THE DYNAMICS OF ACTIVE FILAMENTS

DISSERTATION

zur Erlangung des akademischen Grades

Doctor rerum naturalium

vorgelegt

dem Bereich Mathematik und Naturwissenschaften
der Technischen Universität Dresden

von

Martin Miranda

geboren am 13. April 1993 in Fréjus, Frankreich

Max Planck Institut für Physik komplexer Systeme

Dresden, 2022

Eingereicht am 03.03.2022

Betreuer:
Prof. Dr. Frank Jülicher,
Prof. Dr. Jean-François Joanny.

Gutachter:
Prof. Dr. Frank Jülicher,
Prof. Dr. Jean-François Joanny,
Prof. Dr. Benjamin Friedrich.

ABSTRACT

Biological cilia and flagella are slender organelles which exhibit spontaneous oscillations. These eukaryotic organelles are highly complex structures, comprised of an axoneme—nine pairs of microtubules linked by dynein molecular motors and other structural proteins—enveloped by a membrane. For cilia to generate bending waves, dyneins generate local forces as a function of the ciliary shape, balancing elastic and frictional forces. Is the structural complexity of cilia necessary for this behaviour to arise? Recently, active filament-bundles have been reconstituted. These are minimal synthetic structures, comprised of cytoskeletal filaments and molecular motors, with qualitatively similar behaviour to biological cilia and flagella: spontaneous travelling waves are generated, therefore indicating that spontaneous oscillations are a universal property of slender filament-motor systems. In this dissertation we postulate that biological cilia, and reconstituted active filament bundles, are specific cases of a more general structure: an active filament. The dynamics of active filaments is described by an equation of motion for the filament shape, and a dynamical equation for active moments driving the filament out of equilibrium. The derivation of the equations of motion in the case of planar active filaments is made systematically: the equation of motion for the filament shape is derived using linear irreversible thermodynamics, taking into account external and internal friction forces, while the equation of motion for the active moments follows from the symmetries of filament systems. The resulting dynamical equations can be solved in the time-domain, and are studied analytically and numerically in the limits of dominant external friction, of dominant shear friction, and of dominant curvature friction. We estimate that dominant shear friction is relevant for the study of the dynamics of biological flagella, and reconstituted active filament bundles. In the limit of dominant shear friction, the time-evolution of the filament shape is described by a second order linear differential equation. The theoretical framework is applied to the study of reconstituted actin-bundles. Unlike biological axonemes, actin-bundles are characterised by a heterogeneous number of filaments along its length. Fluorescence imaging of GFP-labelled myosin-V unveils nonlinear myosin-density waves, travelling from the bundle's base to the bundle's apex. The dynamics of myosin-density waves was modelled by taking the bundle heterogeneity into account, with myosin recruitment being a nonlinear function of the local number of filaments and of the curvature. The theoretical framework, derived and applied in this dissertation, describes qualitatively and quantitatively the dynamics of planar active filaments, and can be adapted to study a wide range of different systems. The framework sheds light into the role played by frictional forces in the dynamics of such systems, in particular by suggesting internal friction cannot be neglected when studying active filaments.

ACKNOWLEDGEMENTS

Writing a dissertation is an interesting exercise; as if writing a memoir, one goes back to the past, and see what is there. What is uncovered is, of course, a large amount of work—most of which is of little importance—but also many memories: friendships, conversations, hard times, good times, and an understanding that without the help and support from a large amount of people, this dissertation would have never seen the light of day. I have immense gratitude for all those who made this adventure possible; it is unfortunate that being thorough and exhaustive, when writing acknowledgments, is impossible. I wish therefore, to start by acknowledging the help and contribution of those whose names did not make into these few paragraphs, I am very grateful for the help and support received, and you have my permission to throw rotten tomatoes to me—next time you see me.

I am grateful to my supervisors, Frank Jülicher and Jean-François Joanny, for their understanding and help, and without whom none of this would have happened. They provided me with the opportunity to start and finish this doctorate, in a unique environment, going from Dresden to Paris and back. Their advice is invaluable, and they showed me what true scientific rigour is; how science is performed, not as a matter of theory but as a matter of practice. Frank and Jean-François taught me discipline, preciseness, and how to communicate ideas and concepts effectively. I will always be impressed by how clear cut and incisive the comments of Frank are, and I will always be grateful for Jean-François never-ending joviality. Some of the more intense memories I have from this doctorate are of the three of us in a room, discussing tirelessly, for hours on end. I am not sure I will ever be able to focus for so long ever again.

I cannot be thankful enough towards the non-scientific members of the institute, who are the backbone of PKS. In particular I am grateful to Ulrike Burkert, for being so incredibly competent, and always doing her utmost to keep the division in good order. I am grateful to Anna Burger, who did an incredible job during the year in which she was taking care of us. I would also like to thank the visitor's program, who made my stay so much easier, and the H.R. department, in particular to Elise Voigt who helped me so much when dealing with my many visits to Paris. I would like to thank the IT team, who made sure everything was running smoothly. I would also like to thank the Canteen staff, the cleaning ladies, the reception other staff at the institute, which were all very friendly. I also thank Steffi Gerber, for making the submittal process as easy and swift as was possible.

I am grateful to Pascal Martin, with whom I spend so many hours trying to understand the dynamics of actin-bundles. Without his invaluable presence, these few years would have been very different, and this dissertation would have had a very different focus. His visits to Dresden were always a highlight. I am also grateful to Marie Pochitaloff, who provided the experimental backbone of the thesis.

I would like to thank all of my colleagues at PKS, with whom I had many interesting conversations, as well as many hours drinking coffee and complaining about the weather. The biological-physics division is particularly lively and cheerful, even though scientific life is not always easy, it was made easier with them. In particular, I am grateful to my fellow Ph.D. students. Sara who was my office mate for so long; Giacomo whom I teased so much, and with who I shared my interest in One Piece; Sudarshana for being always cheerful and available for coffee; Fabrizio with his many suits and interesting conversations—who knew, when we met during our master's degree in Paris, that we would end up seeing each other for so many years? Of course I cannot forget the members of the Ph.D. seminar. In no particular order Jonathan, Joanna, Christian, Jonas, Felix, Aida and Omar, who all deserve more than a mere mention. I would also like to thank my other colleagues in the division, again, in no particular order I'm grateful to Stefano, Charlie, Aboutaleb, Joris and others. I wish you all the best of luck in what comes next.

Special thanks to Argo, Lora, Keisuke and Tina who were always there for me, and with whom I developed an enduring friendship. I would like to thank Charlotte and Romaine, for being so supportive and caring.

I am incredibly grateful towards my family, who always supported me. To my father Jaime, and my mother Joélle, who always loved me so much, and did everything they could for my sake; to my brothers and my sister, Mara, Símon and Mathis, always cheering for me; to Katita who was always an example, and to my grandmothers, who love me so unconditionally. Without them, nothing would have been worthwhile. Finally, I cannot express my gratitude to Katarina, whom I had the fortune to meet at the beginning of the pandemic. She has been a constant source of support for these past two years, and a great source of happiness.

CONTENTS

Abstract **i**

Acknowledgements **iii**

1 Introduction **1**
- 1.1 What is an active filament? 1
- 1.2 Theoretical study of cilia and flagella: a short history 5
- 1.3 Outline of the dissertation 7

2 Theory of planar active filaments **9**
- 2.1 Geometry of a filament 9
- 2.2 Symmetry considerations 11
- 2.3 Thermodynamics of a filament 12
- 2.4 Dynamics of an active filament 20

3 Beating of homogeneous active filaments **25**
- 3.1 Linearised dynamical equations 25
- 3.2 Analysis of the filament's beating 27
- 3.3 Limit of dominant external friction 28
- 3.4 Limit of dominant shear friction 35
- 3.5 Limit of dominant curvature friction 55
- 3.6 Relevant regimes for biological flagella 61

4 Study of reconstituted actomyosin bundles **63**
- 4.1 Introduction 63
- 4.2 Active actin filament bundles 63
- 4.3 Theoretical description of actin bundles 71
- 4.4 Discussion 77

5 Summary and Outlook **81**

A Definition of the geometrical shear **85**

B Toy model for the active stress **89**

C Numerical Methods **91**

D Shear control in the limit of dominant shear friction **93**

List of Figures **95**

List of Tables **96**

Bibliography **97**

Versicherung **109**

CHAPTER I

INTRODUCTION

1.1 WHAT IS AN ACTIVE FILAMENT?

The objects of study of this dissertation are active filaments. What is meant, here, by an active filament? Fortunately the term filament is quite simple: a slender mechanical object, where small deformations of the inner structure, with the exception of compression and extension, lead to large global displacements [1, 2]. Activity is defined as the local breaking of detailed balance in the system [3–5]. In particular, an active filament is driven internally, all along the filament, thus excluding otherwise passive filaments which may be driven externally—such as cytoskeletal filaments in motility assays [6, 7], or bacterial flagella driven by basal rotors [8–10].

The most well known, and striking, example of internally driven active filaments, is the one of biological cilia and eukaryotic flagella. The emergent periodic beating, and traveling bending waves, which these organelles display, are one of the mechanisms enabling eukaryotic cell motility—such as in spermatozoa, unicellular and multicellular eukaryotes, e.g. *Paramecia*, *Chlamydomonas*, *Trichoplax adhærens*, among many others, including large organisms such as *Cestum veneris* which grows up to 1.5 m in length [11]. Active filaments, when in large numbers, synchronise and generate fluid flows—as in the trachea and the oviduct, the renal tubules of amphibia, or in the notochordal plate during morphogenesis [12–15].

Recent developments, in the field of biological and soft-matter physics, have seen the emergence of artificial active filament bundles. These bundles, constructed out of biological proteins and molecular motors, exhibit a behaviour qualitatively similar to that of biological axonemes: travelling bending waves and synchronisation between bundles are also observed [16, 17].

Why are these systems, be they biological or artificial, of interest to a physicist? For robust travelling waves, to occur in media characterised by low Reynolds number, where inertial terms vanish, energy has to be constantly consumed, to generate active forces, to balance the dissipative and elastic forces. Furthermore, the active drive has to be itself an oscillating quantity. These oscillations result from a feedback between active force generation and filament shape.

1.1.1 BIOLOGICAL ACTIVE FILAMENTS

Biological active filaments, more commonly known as cilia or eukaryotic flagella, consist of an inner structure called the axoneme, which is enveloped by a membrane. They are highly conserved organelles, meaning that the origin of the structure goes as far back as the last common eukaryotic ancestor [18]. Flagella are quite slender, with a width going from 240 nm to 1 200 nm, and a length typically going from 12 μm to 50 μm, but may be as short as 5 μm and as long as 2 mm in *Ctenophora* [19–21].

The axoneme consists most commonly of 9 microtubule doublets surrounding 2 central microtubules (called an 9+2 structure), however, many other configurations exist; the gametes of *Diplauxis hatti* and *Lecudina tuzetae* possess a motile flagellum with a 3+0 and 6+0 axoneme respectively, motile flagella have also been observed with 9+0, 9+1, 9+2, 9+3 and 9+4 axonemes [19–28], and even with a 9 + 9 + 3 axoneme [29]. In between each microtubule doublet there are two rows of dynein molecular motors, the inner and outer arms. These dynein molecular motors generate force and drive the beating of the flagellum. Axonemes are very complex structures, with more than 650 types of proteins, and many other bio-molecules [30], we will not, however, discuss the details of the axonemal structure

The axoneme is anchored to the cell through the basal body, a structure consisting of nine microtubule triplets. The basal body goes into the cell up to about 400 nm, and dynamically responds to axoneme deformations during the beating cycle of a flagellum [31, 32].

1.1.2 ARTIFICIAL ACTIVE FILAMENT BUNDLES

Biological cilia and flagella are very complex structures, which are the minimal ingredients needed for bending waves to form? An avenue of investigation consists on selectively removing, more or less invasively, structures from an axoneme, and studying the effects of the removal [26, 33]. Another approach, has been to construct active bundles from minimal ingredients, in a laboratory setting, and replacing proteins with analogues with similar function.

The first of these synthetic active filament are microtubule - kinesin bundles, anchored to air bubbles and formed with the help of a depleting agent. These active filament bundles have been shown to beat, synchronise and form metachronal waves. The kinesin molecular motors generate gliding motion between anti-parallel microtubules, and anchor parallel ones. The length of active microtubule bundles goes from 10 μm up to 100 μm and controls the beat frequency [16].

The second example consists of actin filaments, grown on actin nucleation sites, and which are all oriented in a parallel direction. Bundle formation occurs spontaneously, in the presence of a depleting agent, and myosin molecular motors. These bundles are active, exhibit periodic beating, wave propagation and synchronisation [17].

The two previous examples provide strong evidence that beating, and wave propagation, are universal features of active filaments. By replacing all of the ingredients which compose an axoneme, an oscillatory behaviour is still observed, thus showing that self-sustained bending waves, are not restricted to the particular interplay between microtubules, dyneins, nexin and so on.

1.1.3 Biochemistry of an active filament

We will do a very short description of the most important proteins which constitute an active filament. These proteins are of two main types: the elastic fibres which make the backbone of the full filament, and the molecular motors which drive them. They can be either microtubules and their associated molecular motors, dyneins and kinesins, or actin filaments and their associated superfamily of molecular motors, myosins. All known molecular motors are ATPases, and convert chemical energy to mechanical energy through the hydrolysis of ATP [36].

Microtubules are the biggest and stiffest of the cytoskeletal filaments. They are assembled out of tubulin heterodimers in a helical fashion and are therefore polar. The helicity defines a plus and a minus end. Microtubules are highly dynamic, with phases characterised by slow polymerisation or fast depolymerisation, however in an axoneme the length is static [37,38]. A microtubule has a width of around $12\,\mu\mathrm{m}$ [37] and a persistence length ranging from $500\,\mu\mathrm{m}$ to $3000\,\mu\mathrm{m}$ depending on its length [39,40], and a bending stiffness of around $2 \cdot 10^{-22}\,\mathrm{Nm}^2$ [40].

Dyneins belong to a family of closely related molecular motors. They have one to three heads, are processive, and directed towards the minus end of a microtubule, with $10\,\mathrm{nm}$ long steps [41–43]. The other important family of processive molecular motors are kinesins. Unlike dyneins they move towards the plus end of a microtubule, with $8\,\mathrm{nm}$ long steps. There are 14 different known families of kinesins [44,45]

The second family of biofilaments which we are concerned with are actin filaments, constituted of small globular proteins called actin monomers (G-actin), which spontaneously assemble into thin polymers (F-actin) of $7\,\mathrm{nm}$ in diameter. Actin filaments are helical, with a periodicity of around $37\,\mathrm{nm}$, as a corollary F-actin are polar, with a plus and a minus end. The persistence length of an actin filament (F-actin) is around $20\,\mu\mathrm{m}$ and the bending rigidity is around $7 \cdot 10^{-26}\,\mathrm{Nm}^2$ [37,40]. The only superfamily of molecular motors associated with actin are myosins. Of these molecular motors, some are processive, such as myosin-V, while some are not, such as myosin-II [46, 47]. One of the most important, and well-known, functions of myosin-II is that of muscle contraction. The step-size of myosin-V is slightly smaller than $37\,\mathrm{nm}$, the periodicity of F-actin, therefore processive myosins have a helical trajectory around the filament, towards one of the ends [48,49].

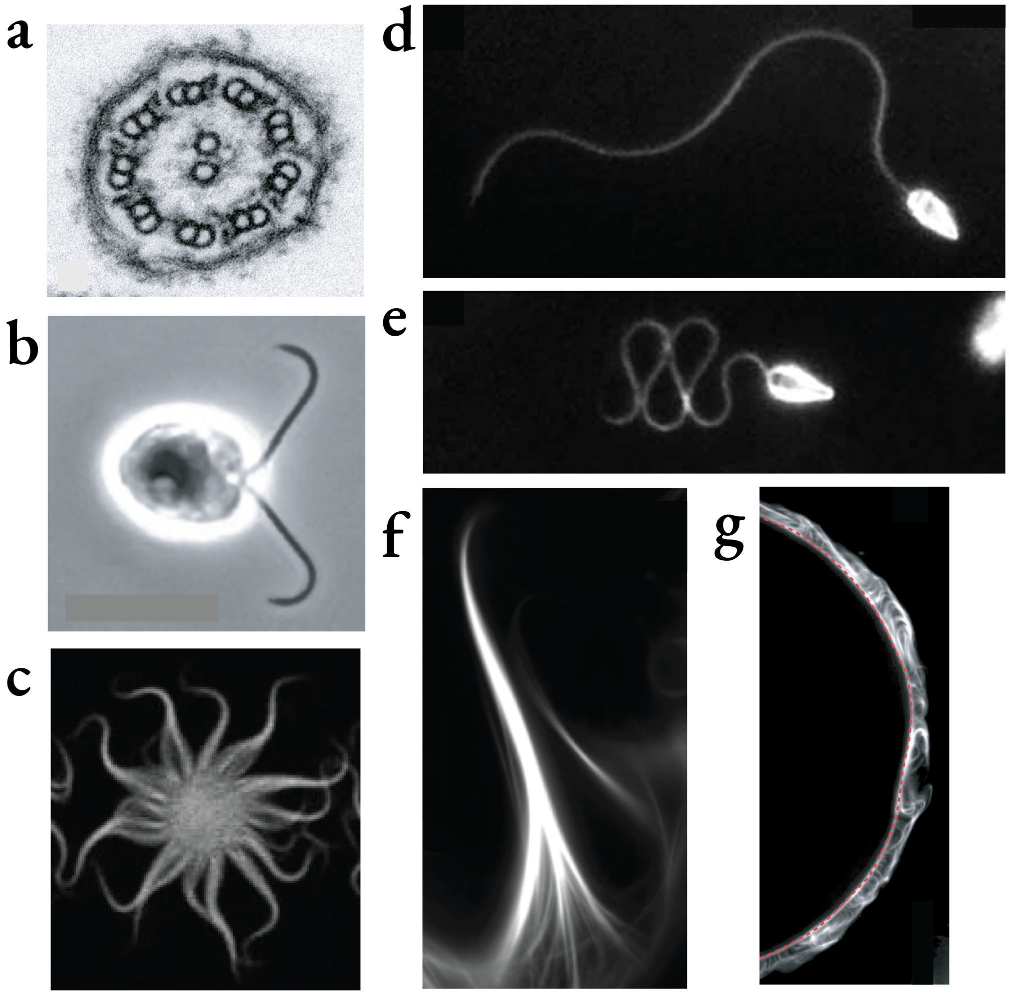

Figure 1.1: Examples of active filaments: (**a**) cross-section of an eukaryotic flagellum, showing the 9+2 axoneme surrounded by a membrane, adapted from [30], (**b**) Chlamydomonas Reinhardtii, adapted from [34], (**c**) reconstituted actomyosin bundles [17], (**d**) sea urchin spermatozoa in artificial sea water, adapted from [35], (**e**) sea urchin spermatozoa in highly viscous artificial sea water ($4\,\mathrm{Pa\,s}$), adapted from [35], (**f**) microtubule bundle and (**g**) air bubble covered by beating microtubule bundles adapted from [16].

1.2 Theoretical study of cilia and flagella: a short history

Active filaments have a long history in biology; they are the oldest known organelles, described in 1675 by Anthony van Leeuwenhoek [50, 51], ten years after cells were first described by Robert Hooke in 1665 [52]. We will however jump over a couple hundred years, reviewing the development of the modern theoretical treatment of the dynamics of biological active filaments.

The physics community was first interested in the question of propulsion: how do cells propel themselves in a very low Reynold's number regime? The displacement of animals of macroscopic size had been treated by James Gray [53–57], however the principles underlying the locomotion of larger scale organisms—based on inertial forces—cannot be extended to the study of the motility of microscopic organisms, where viscous forces are dominant. Sir Geoffrey Taylor, closely followed by Hancock, was the first to mathematically study the propulsion of spermatozoa in the non-inertial regime [58–60]. The propulsion velocity of a micro-organism was then related to the undulations of an infinite sheet, under the assumption of small wave amplitudes. The results of Taylor were extended by Gray and Hancock to larger amplitudes, and finite filament lengths, using the experimental data of sea-urchin spermatozoa [61, 62].

In the previous studies, the dynamics of the flagellum itself were ignored, and the question of how it was able to dynamically change its shape was not posed. In particular, is a flagellum driven at the base, or are there bending moments produced along it? It was Machin who first attempted to answer this question [63], and showed that a basal drive was unable to describe the motion of a flagellum. He instead posited the existence of bending moments f, balanced by elastic and frictional moments. The balance of torques gives rise to the Machin equation:

$$\xi_\perp \partial_t y = -\kappa \partial_s^4 y - \partial_s^2 f, \tag{1.1}$$

where $y(s, t)$ is the transverse deformation of the filament, $\xi_\perp$ is the fluid friction, κ the bending rigidity of the flagellum, and $\{s, t\}$ are the filament arc-length and the time respectively. What is the nature of the active bending moment f? It was naturally assumed by Machin that the flagellum was composed of contractile elements: "A flagellum can be idealized into an elastic filament surrounded by or enclosing a series of bilaterally arranged contractile elements, differential contraction of elements on the two sides producing localized bending moments [63]."

The approach was quickly extended to model the active bending moment f more explicitly, and to take into account possible effect of nonlinearities [64], as well as the structural heterogeneity of a flagellum [65]. It was assumed that f was a function of the curvature's rate of change.

Electron microscopy revolutionised the physical study of the flagellum, as it enabled for the first time to see the inner structure, the axoneme [66–70]. Insights from the axonemal structure lead to the development of the sliding filament model by Brokaw and Satir [71–75]. From then on, the main theoretical question was the nature of the active bending moment f, which was now assumed to generate shear within the active filament. Three main approaches developed (with some overlap) [13,76,77]: (a) treat f as a black box, assuming some relationship between the Fourier transform of f and the Fourier transforms of either the curvature, the shear between microtubule doublets or the normal force [64,71,74,78–82], (b) write f explicitly, either as a time-delayed curvature term, as the output of a phenomenological evolution equation, or as the result of stresses internal to the flagellum [75, 83–89],(c) model the molecular dynamics of the force generating dynein molecular motors [90–93].

Most published work on the dynamics of active filaments made the assumption that fluid friction balances active and elastic forces[1]. There are, however, other frictional forces. In particular, due to microscopic configuration changes, any conformational change of a real material dissipates energy. For a filament, there are four different possible deformations: bend, shear, torsion, and extension or compression [1, 2]. Each such change in conformation, is associated to a different dissipative process, coming from different microscopic dynamics, and may be coupled [94–99]. Furthermore, many passive bio-filaments, such as chromosomes, and even microtubules when shorter than 5 μm, are known to be dominated by internal dissipation [39,100]. The dissipation associated to shear are of particular interest. As an active filament shears, its constituent fibres slide with respect to each other. The intra-filament sliding is then associated with binding-unbinding events of molecular motors attached to a pair of sliding fibres, which dissipates energy [101–105].

In light of the previous paragraph, we can highlight some novel studies of the dynamics of active filaments. Mondal et al. have analysed the beating of reactivated *Chlamydomonas* flagella, and found that fluid viscosity does not contribute to propagating waves. This lead them to develop a theory where the shear and curvature dissipation are dominant [106]. Nandagiri et al. analysed beating patterns of mouse sperm, and considered a Kirchhoff rod model, where no shear is allowed. They found that were the sperm flagellum an unshearable rod, then the dissipative contribution coming from curvature changes would be ten times greater than the hydrodynamic dissipation [107]. Finally, Geyer et al. have analysed the beating of isolated cilia from *Chlamydomonas* in a wide variety of experimental conditions, and found that the limit of small fluid friction provides a good fit [108].

---

[1] Exceptions coming to mind are [75,86,87,92], in which the presence of internal friction was used to find stable numerical solutions

1.3 OUTLINE OF THE DISSERTATION

The aim of the thesis is to understand the dynamic interplay between the active filament's mechanics, and the active moments driving its periodic motion. In chapter 2 we construct general dynamical equations from minimisation and symmetry principles, the derivation enables the systematic treatment of different frictional forces. The general equations are fourth order nonlinear partial differential equations, which take into account geometrical and structural effects. In chapter 3 we study the limit cases of the equations of motion derived in the previous chapter. In particular we investigate the existence of oscillatory instabilities in regimes dominated by external or internal frictions. We estimate that the regime of dominant internal shear friction most closely describes biological cilia and flagella. The theory is then applied to the dynamics of synthetic active actin-filament bundles, in chapter 4. These actin-bundle systems are heterogeneous, and display highly nonlinear effect, such as nonlinear myosin-density waves travelling from the base to the tip of actin-bundles. Finally, chapter 5 gives an overview of the results, as well as discusses open questions which may be addressed by future work.

CHAPTER 2

THEORY OF PLANAR ACTIVE FILAMENTS

The present chapter constructs a phenomenological theory, independent of microscopic details, coupling the active force generation with the dynamics of the filament conformation. This coupling may, in certain conditions, lead to the appearance of oscillatory instabilities, displaying bending wave propagation. The filament conformation is governed by a balance between the dissipative, elastic forces, and active forces.

Phenomenological laws are derived using the formalism of linear irreversible thermodynamics, in order to describe the non-equilibrium mechanics of the filament. On their own, these phenomenological laws are passive and drive the system towards equilibrium. For the system to be active, the formalism is extended to add active forces which do not derive from a variational principle. These terms continuously add energy to the system, and therefore drive the system out of equilibrium.

We consider an incompressible filaments whose movement is restricted to a two dimensional plane. The motivation is out of simplicity, as three dimensional movement is characterised by many geometric nonlinearities [1, 2]. However, the interest is not purely theoretical, as the regime described by planar dynamics does describe a large number of real systems [35, 37, 40, 109]. We also consider the filament to be incompressible

2.1 GEOMETRY OF A FILAMENT

An active filament, of length L, is embedded in a viscous fluid. Its centreline corresponds to a curve γ parametrised by $s \in \{0, L\}$, whose position in space is $\boldsymbol{r}(s,t) = x(s,t)\boldsymbol{u}_x + y(s,t)\boldsymbol{u}_y$, with $\{\boldsymbol{u}_x, \boldsymbol{u}_y\}$ an orthonormal basis spanning the two dimensional Euclidean plane. The filament is of width $w(s)$. At each point along γ we can also define the tangent and normal vectors $\boldsymbol{t}$:

$$\boldsymbol{t}(s,t) = \cos\left(\psi(s,t)\right)\boldsymbol{u}_x + \sin\left(\psi(s,t)\right)\boldsymbol{u}_y, \tag{2.1}$$

$$\boldsymbol{n}(s,t) = -\sin\left(\psi(s,t)\right)\boldsymbol{u}_x + \cos\left(\psi(s,t)\right)\boldsymbol{u}_y, \tag{2.2}$$

where $\psi(s,t)$ is the angle between the tangent vector $\boldsymbol{t}(s,t)$ and $\boldsymbol{u}_x$. The filament must obey the following geometrical constraints:

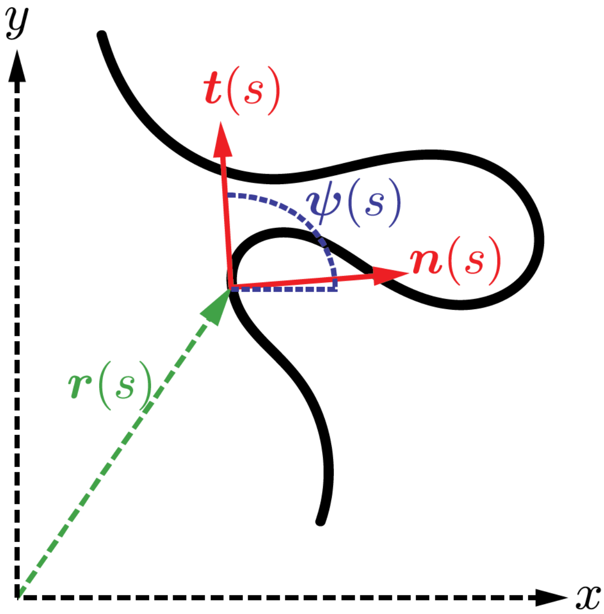

Figure 2.1: Schematic of a planar filament in black, in a two dimensional plane spanned by axes x and y, with the position vector $\boldsymbol{r}$ in green, the tangent $\boldsymbol{t}$ and normal $\boldsymbol{n}$ vectors in red, as well as the tangent angle ψ in blue.

$$\partial_s \boldsymbol{r}(s,t) = \boldsymbol{t}, \tag{2.3}$$

$$\partial_s \psi(s,t) = C(s,t), \tag{2.4}$$

where C is the centreline curvature. If the filament is incompressible, a bend must be related to a shear $a\Delta + \mathscr{O}(a^2)$, where a is the distance from the centreline. We call Δ the geometrical shear, which is defined as:

$$\Delta(s,t) = \Delta_0(t) + \int_0^s \mathrm{d}s' C(s',t), \tag{2.5}$$

Where Δ_0 is the basal shear. See Appendix A for more details on he derivation of the shear. From equations (2.4,2.5) we observe that the arc-length derivatives of the angle ψ and the shear Δ are equal:

$$\partial_s \psi = \partial_s \Delta. \tag{2.6}$$

Symmetries of the system	
Time translation	$t \to t + t_0$
Spatial translational invariance	$\boldsymbol{r} \to \boldsymbol{r} + \boldsymbol{r}_0$
Rotational invariance	$\psi \to \psi + \psi_0$
Mirror symmetry	$\{C, \psi, \Delta\} \to \{-C, -\psi, -\Delta\}$
Broken symmetries	
Time reversal	$t \nrightarrow -t$
Polarity	$s \nrightarrow -s$

Table 2.a: List of the respected and broken symmetries of planar filaments considered in this dissertation

It may seem redundant to define Δ in addition to ψ, as they differ only by a function of time $\Delta(s,t) = \psi(s,t) + \Delta(0,t) - \psi(0,t)$. However, the shear is rotationally invariant, while the tangent angle is not. Furthermore, we shall see in subsequent sections, that in the case of a simple fluid, the tangent angle's rate of change does not dissipate energy [99].

2.2 SYMMETRY CONSIDERATIONS

All physical systems are constrained, and characterised, by their symmetries; the dynamical equations and state variables of a given system must obey the symmetries of the studied system. As a corollary, a physical system with a broken symmetry may display many novel phenomena, which are forbidden in a system where the symmetry is not broken. A characteristic symmetry of an equilibrium system is the time-reversal symmetry: the arrow of time is undefined and a movie played forwards is undistinguishable from the same movie played backwards [110, 111]. While time-reversal symmetry is not sufficient for a system to be in equilibrium, it's breaking is a sufficient condition for a system to be out-of-equilibrium. We study systems in which the time-reversal symmetry is broken, as it is the case for most biological systems.

In the following few paragraphs, as summarised in Table 2.a, we list the symmetries relevant to the class of systems under consideration. Notable symmetries are the time translation invariance, the spatial translation invariance, and the rotational invariance—these imply conservation of energy, conservation of linear momentum, and conservation of angular momentum, respectively.

We assume that mirror symmetry holds—that is, changing the sign of the curvature, the tangent angle, and the shear, does not change the dynamics of the system. It is important to note here that in most real systems, whose internal components are chiral, this assumption is not correct. The effects of chirality are not treated in this dissertation, as this requires a more general three dimensional treatment, we can however note that many biological flagella display helical oscillations, and that even for those exhibiting planar beating, it is planar only in the time-scale of a few periods, and can be regulated by viscosity [35]. However, the artificial active filaments seen in [16] might not be a priori chiral because the authors do not control the alignment of the microtubules.

All known active filaments are polar: going from the basal end to the distal end of the filament, or vice-versa, is important to the overall dynamics. The breaking of that symmetry is fundamental for the existence of bending waves directed in a preferential direction, which enables the motility of flagellates.

Depending on the particular subclass of systems, we may decide to uphold more symmetries, such as centreline translation invariance $s \to s+s_0$, in which case explicit functions of the centreline arc-length—such as position dependent width—would not be allowed. We note that conjugate forces to the system fluxes must display the same symmetries as these fluxes [112], with the exception of time-reversal symmetry, in which case the sign of a time-reversal transformations depends on whether a flux is reactive of dissipative.

2.3 THERMODYNAMICS OF A FILAMENT

In this section we derive the phenomenological equations describing the dynamics of a filament. We first write a free energy from the symmetry considerations, and compute its variation variation, taking into account mechanical and geometrical constraints. The variation enables us to write the entropy production of a passive filament. Linear irreversible thermodynamics lead to relaxation dynamics, which are be generalised by adding active forces. The active forces do not derive from free energetic considerations.

The phenomenological equations describe a large number of dynamical regimes, including previous models of flagellar beat [78–82], as well as in new regimes, in particular regimes where internal dissipation cannot be neglected.

2.3.1 BALANCE LAWS

The thermodynamics of a filament is described by potentials such as the energy $\mathscr{U}$, the entropy $\mathscr{S}$, the free energy $\mathscr{F}$ and so forth. These potentials are integral quantities defined over the filament length:

$$\mathscr{U} = \int_0^L \mathrm{d}s' u(s',t), \qquad \mathscr{S} = \int_0^L \mathrm{d}s' \sigma(s',t), \qquad \mathscr{F} = \int_0^L \mathrm{d}s' f(s',t), \tag{2.7}$$

where u is the energy density of the filament, σ the entropy density, and f the free energy density. The variation of these quantities follows the global conservation laws:

$$\partial_t \mathscr{U} = -J_{\mathscr{U}}, \tag{2.8}$$
$$\partial_t \mathscr{S} = \Theta - J_{\mathscr{S}}, \tag{2.9}$$
$$\partial_t \mathscr{F} = \Theta_{\mathscr{F}} - J_{\mathscr{F}}, \tag{2.10}$$

where $J_{\mathscr{U}}$, $J_{\mathscr{S}}$ and $J_{\mathscr{F}}$ are the total energy, entropy and free energy fluxes, respectively, Θ and $\Theta_{\mathscr{F}}$ are the entropy and free energy production, respectively. These conservation laws in their local form are:

$$\partial_t u + \partial_s j_u = 0, \tag{2.11}$$
$$\partial_t \sigma + \partial_s j_\sigma = \theta, \tag{2.12}$$
$$\partial_t f + \partial_s j_f = \theta_f, \tag{2.13}$$

where j_u, j_σ and j_f are the local energy, entropy and free energy flux, respectively; θ and θ_f are the entropy and free energy production density, respectively. In a small line element, the equilibrium relation $f = u - T\sigma$ is valid. We assume that the system is isothermal, therefore in contact with a heat bath, then we have [113]:

$$j_f = j_u - T j_\sigma, \tag{2.14}$$
$$\theta_f = -T\theta. \tag{2.15}$$

2.3.2 THE FREE ENERGY FUNCTIONAL

We write the free energy functional for a filament. The free energy takes into account the configuration of the filament at any given time. The most general form of the free energy, up to quadratic order, without spatial derivatives and which obeys the symmetries stated in the previous section is [114–118]:

$$\mathscr{F}[C,\Delta] = \int_0^L \mathrm{d}s' \left(\frac{\kappa_C}{2} C^2 + \frac{\kappa_\Delta}{2} \Delta^2 + \frac{\kappa_{C,\Delta}}{2} C\Delta \right), \tag{2.16}$$

Dimensions of the parameters	
Bending elasticity	$[\kappa_C] = \frac{ML^3}{T^2}$
Shear elasticity	$[\kappa_\Delta] = \frac{ML}{T^2}$
Active moment relaxation rate	$[k_\mathrm{d}] = \frac{1}{T}$
Activation constant	$[k_\mathrm{a}] = \frac{ML^2}{LT^2}$
Dimensions of the friction coefficients	
Curvature friction coefficient	$[\xi_C] = \frac{ML^3}{T}$
Shear friction coefficient	$[\xi_\Delta] = \frac{ML}{T}$
Angular friction coefficient	$[\xi_\psi] = \frac{ML}{T}$
Normal friction coefficient	$[\xi_\perp] = \frac{M}{LT}$
Dimensions of the Lagrange multipliers	
Angular moment	$[M_\psi] = \frac{ML^2}{T^2}$
Shear moment	$[M_\Delta] = \frac{ML^2}{T^2}$
Force	$[\boldsymbol{F_r}] = \frac{ML}{T^2}$

Table 2.b: Physical quantities and their dimensions, where T is the dimension of time, M is the dimension of mass and L is the dimension of length

where κ_C and κ_Δ denote the bending and shear rigidity, respectively. The parameter $\kappa_{C,\Delta}$ describes an elastic coupling between curvature and shear. All of the parameters are in principle, functions of the centreline arc-length s. Terms which are explicitly functions of $\boldsymbol{r}$ and ψ are not allowed due to translational and rotational invariance. The addition of gravitational effects, magnetic fields, or any other form of potential would break translational symmetry and thus allow for the presence of further terms depending on the position or the orientation. We ignore such effects in the present dissertation.

External forces and torques can act on the filament at its boundaries, and can be described by the following work function:

$$
\begin{aligned}
W = &+\frac{k_\psi}{2}\left(\psi(0,t)-\psi_0\right)^2 - T_0^\psi \psi(0,t) - T_L^\psi \psi(L,t) \\
&+\frac{k_\Delta}{2}\left(\Delta(0,t)-\Delta_0\right)^2 - T_0^\Delta \Delta(0,t) - T_L^\Delta \Delta(L,t) \\
&-\boldsymbol{F}_0^{\mathrm{ext}} \cdot \boldsymbol{r}(0,t) - \boldsymbol{F}_L^{\mathrm{ext}} \cdot \boldsymbol{r}(L,t).
\end{aligned}
\tag{2.17}
$$

The time derivative of W is the work done by external forces and torques. Adding

W to $\mathscr{F}$ we obtain the potential $\mathscr{G}$:

$$\mathscr{G} = \mathscr{F} + W. \tag{2.18}$$

When taking the variation of this sum, the boundary contributions due to the free energy flux and the work function balance each other, and only the bulk contribution remains, which is equal to the free energy production. If the system is isothermal, because of (2.15), the free energy production is proportional to the entropy production.

2.3.3 ENTROPY PRODUCTION OF A FILAMENT NEAR EQUILIBRIUM

We derive in this section the entropy production for a filament. The rate of change of the potential $\mathscr{G}$ can be written, using the definition (2.18) and equations (2.13,2.15), as:

$$\frac{\mathrm{d}\mathscr{G}}{\mathrm{d}t} = -T\Theta - J_{\mathscr{F}} + \frac{\mathrm{d}W}{\mathrm{d}t}. \tag{2.19}$$

The variables C, Δ and $\boldsymbol{r}$ are not independent, but must satisfy the geometrical constraints outlined in section 2.1. In order to do compute the rate of change we therefore introduce the Lagrange functional:

$$\mathscr{C} = \int_0^L \mathrm{d}s' \left(M_\psi \left(\partial_s \psi - C \right) + M_\Delta \left(\partial_s \Delta - C \right) + \boldsymbol{F_r} \cdot \left(\partial_s \boldsymbol{r} - \boldsymbol{t} \right) \right), \tag{2.20}$$

where M_ψ, M_Δ and $\boldsymbol{F_r}$ are Lagrange multipliers with the dimensions of two moments and a force, respectively. When taking the variation of the potential $\mathscr{G}$, the constraint functional $\mathscr{C}$ cannot be neglected, because its variation can be finite. Therefore equation (2.19) becomes:

$$\frac{\mathrm{d}}{\mathrm{d}t}(\mathscr{G} + \mathscr{C}) = -T\Theta - J_{\mathscr{F}} + \frac{\mathrm{d}W}{\mathrm{d}t}, \tag{2.21}$$

where Θ and $J_{\mathscr{F}}$ are the entropy and free energy flux defined in equations (2.9, 2.10). The integration by parts of the functional $\mathscr{C}$ yields a bulk term and a boundary. The boundary term is identified to the free energy flux such that:

$$-J_{\mathscr{F}} = \int_0^L \mathrm{d}s' \partial_s \left(M_\psi \partial_t \psi + M_\Delta \partial_t \Delta + \boldsymbol{F_r} \cdot \partial_t \boldsymbol{r} \right). \tag{2.22}$$

Variables	Fluxes	Conjugate thermodynamic forces	Dimensions
Curvature C	$\partial_t C$	$-\frac{\delta \mathscr{G}}{\delta C} = -\kappa_C C - \kappa_{C,\Delta}\Delta + M_\psi + M_\Delta$	$[C] = \frac{1}{L}$
Shear Δ	$\partial_t \Delta$	$-\frac{\delta \mathscr{G}}{\delta \Delta} = -\kappa_\Delta \Delta - \kappa_{C,\Delta} C + \partial_s M_\Delta$	$[\Delta] = 1$
Tangent angle ψ	$\partial_t \psi$	$-\frac{\delta \mathscr{G}}{\delta \psi} = \partial_s M_\psi + \boldsymbol{F_r} \cdot \boldsymbol{n}$	$[\psi] = 1$
Position $\boldsymbol{r}$	$\partial_t \boldsymbol{r}$	$-\frac{\delta \mathscr{G}}{\delta \boldsymbol{r}} = \partial_s \boldsymbol{F_r}$	$[\boldsymbol{r}] = L$

Table 2.c: Conjugated thermodynamic fluxes and forces

Because the free energy flux and the work function rate of change are boundary contributions, their sum vanishes:

$$-J_{\mathscr{F}} + \frac{\mathrm{d}W}{\mathrm{d}t} = 0. \tag{2.23}$$

We can finally write the entropy production as:

$$-T\Theta = \int_0^L \mathrm{d}s' \left(\frac{\delta \mathscr{G}}{\delta C} \partial_t C + \frac{\delta \mathscr{G}}{\delta \Delta} \partial_t \Delta + \frac{\delta \mathscr{G}}{\delta \psi} \partial_t \psi + \frac{\delta \mathscr{G}}{\delta \boldsymbol{r}} \cdot \partial_t \boldsymbol{r} \right), \tag{2.24}$$

where the functional derivatives take into account the geometrical constraints given by the functional $\mathscr{C}$. The explicit form of these functional derivatives is written in Table 2.c

2.3.4 Linear irreversible thermodynamics

The entropy production of a system near equilibrium is a bilinear quadratic form, consisting of the sum of the products of thermodynamic fluxes and their conjugates thermodynamic fluxes, which we write in a concise form as:

$$T\Theta = -\int_0^L \mathrm{d}s' \partial_t \boldsymbol{\eta} \cdot \frac{\delta \mathscr{G}}{\delta \boldsymbol{\eta}}, \tag{2.25}$$

where $\boldsymbol{\eta} = (C, \Delta, \psi, x, y)^T$. The formalism of linear irreversible thermodynamics—developed by Onsager, Casimir, Machlup and others in the first half of the twentieth century [94–98]—assumes a linear relationship between the forces and the fluxes such that:

$$\Xi \partial_t \boldsymbol{\eta} = -\frac{\delta \mathscr{G}}{\delta \boldsymbol{\eta}}, \tag{2.26}$$

where Ξ is the friction tensor, whose elements are $\xi_{\eta,\eta'}$. Using this linear relation to substitute the thermodynamic forces in equation (2.25), we find:

$$T\Theta = \int_0^L \mathrm{d}s' \partial_t \boldsymbol{\eta} \cdot \Xi \partial_t \boldsymbol{\eta}. \tag{2.27}$$

Because the entropy production is always positive, the tensor Ξ must be semi-definite positive. Therefore its determinant is such that:

$$\det \Xi = 0. \tag{2.28}$$

This is ensured if the following condition between the diagonal and off-diagonal elements is respected [94, 119, 120]:

$$\xi_{\eta,\eta'}^2 \leq \xi_{\eta,\eta} \xi_{\eta'\eta'}. \tag{2.29}$$

To ensure microscopic time-reversibility, the off-diagonal elements of the tensor Ξ follow Onsager's reciprocal relations [94–98], such that:

$$\xi_{\eta,\eta'} = \xi_{\eta',\eta}. \tag{2.30}$$

In the case of systems with inertia, or which break microscopic time-reversibility, such as in the presence of magnetic fields, the above relations are replaced by the Onsager-Casimir reciprocal relations [96–98].

2.3.5 EQUATIONS WITH ACTIVE FORCES

The equations of linear irreversible thermodynamics defined by (2.26), describe a system with relaxational dynamics, with an initial transient followed by an equilibrium steady state. In order to drive the system continuously out of equilibrium, energy has to be injected into the system in the form of active forces and torques. In order to do this, we write modified phenomenological equations:

$$\Xi \partial_t \boldsymbol{\eta} = -\frac{\delta \mathscr{G}}{\delta \boldsymbol{\eta}} - \boldsymbol{f}^{\text{act.}}, \tag{2.31}$$

where $\boldsymbol{f}^{\text{act.}}$ is a vector of active moments and forces. The above equation extends the Onsager theory of near-equilibrium thermodynamics to active systems not described by a free energy principle. A system described by a free energy principle is such that the evolution equation for a field ϕ has the form $\partial_t \phi = -\delta \mathscr{F} / \delta \phi$. Here the active force vector does not derive from a free energy therefore $\partial_t \phi = f(\phi)$ where $f \neq \delta \mathscr{F} / \delta \phi$ [121]. In principle the active force vector may have active contributions specific to each variable, however, for the sake of simplicity we suppose that it only has one single contribution, the active moment conjugate to shear, so that:

$$\boldsymbol{f}^{\text{act.}} = \begin{pmatrix} 0 \\ m_{\text{a}} \\ 0 \\ 0 \\ 0 \end{pmatrix} . \tag{2.32}$$

The dynamics of the active moment density m_{a} is discussed in section 2.4.3.

Dissipation is either internal or external. Internal dissipative forces are related to changes in the internal configuration of the filament, either by changing the curvature or by shearing of the filament. External dissipative forces are related to the displacement of the filament in the fluid medium. We assume that no cross-coupling exists between internal and external sources of dissipation. The Onsager matrix therefore takes the following form:

$$\Xi = \begin{pmatrix} \xi_C & \xi_{C,\Delta} & \xi_{C,\psi} & 0 & 0 \\ \xi_{C,\Delta} & \xi_\Delta & \xi_{\Delta,\psi} & 0 & 0 \\ \xi_{C,\psi} & \xi_{\Delta,\psi} & \xi_\psi & \xi_{\psi,x} & \xi_{\psi,y} \\ 0 & 0 & \xi_{\psi,x} & \xi_{x,x} & \xi_{x,y} \\ 0 & 0 & \xi_{\psi,y} & \xi_{x,y} & \xi_{y,y} \end{pmatrix} . \tag{2.33}$$

The top left sub-matrix describes internal friction, while the bottom right sub-matrix describes external friction. The friction coefficients associated to the tangent angle's rate of change ξ_ψ could be either external or internal. External rotational friction could be due to the active filament being embedded in a chiral fluid [99]. Internal rotational friction cannot be ruled out to exist, but its mechanism is unknown. We will assume the active filament to be immersed in a simple fluid, therefore external rotational viscosity vanishes, we will also assume internal rotational friction to be negligible, therefore $\xi_\psi = 0$. Because of relation (2.29), the off-diagonal coefficients also vanish, therefore $\xi_{\psi,x} = \xi_{\psi,y} = 0$ and $\xi_{C,\psi} = \xi_{\Delta,\psi} = 0$.

The external friction sub-matrix is can be further sub-divided, with the bottom right 2x2 viscous friction tensor $\Xi_{\boldsymbol{r}}$, describing the friction due to translation, such that $\Xi_{\boldsymbol{r}} \boldsymbol{t} = \xi_{\parallel} \boldsymbol{t}$ and $\Xi_{\boldsymbol{r}} \boldsymbol{n} = \xi_{\perp} \boldsymbol{n}$, and can therefore be written as:

$$\Xi_{\boldsymbol{r}} = \begin{pmatrix} \xi_{x,x} & \xi_{x,y} \\ \xi_{x,y} & \xi_{y,y} \end{pmatrix} = \begin{pmatrix} \xi_{\|} \cos^2 \psi + \xi_{\perp} \sin^2 \psi & \left(\xi_{\|} - \xi_{\perp}\right) \sin \psi \cos \psi \\ \left(\xi_{\|} - \xi_{\perp}\right) \sin \psi \cos \psi & \xi_{\|} \sin^2 \psi + \xi_{\perp} \cos^2 \psi \end{pmatrix}, \tag{2.34}$$

where the tangential and normal friction coefficients $\xi_{\|}$ and $\xi_{\perp}$ are functions of the fluid viscosity ξ_{f}, the length of the filament L and its width $w(s)$. Slender-body theory gives the following expressions for these coefficients [122–125]:

$$\xi_{\|} = \frac{4\pi\xi_{\mathrm{f}}}{\ln\left(2\frac{L}{w(s)}\right) + \frac{1}{2}}, \tag{2.35}$$

$$\xi_{\perp} = \frac{2\pi\xi_{\mathrm{f}}}{\ln\left(2\frac{L}{w(s)}\right) - \frac{1}{2}}. \tag{2.36}$$

We can now write the phenomenological equations explicitly, we then have two equations for the internal degrees of freedom:

$$\xi_C \partial_t C + \xi_{C,\Delta} \partial_t \Delta = -\kappa_C C - \kappa_{C,\Delta} \Delta + M_{\psi} + M_{\Delta}, \tag{2.37}$$

$$\xi_{\Delta} \partial_t \Delta + \xi_{C,\Delta} \partial_t C = -\kappa_{\Delta} \Delta - \kappa_{C,\Delta} C + \partial_s M_{\Delta} - m_{\mathrm{a}}, \tag{2.38}$$

and one vectorial equation for the translational degrees of freedom:

$$\Xi_{\boldsymbol{r}} \partial_t \boldsymbol{r} = \partial_s \boldsymbol{F}_{\boldsymbol{r}}. \tag{2.39}$$

As a consequence of the absence of rotational friction, we have the following relation between the Lagrange multipliers $\boldsymbol{F}_{\boldsymbol{r}} \cdot \boldsymbol{n}$ and M_{ψ}:

$$\partial_s M_{\psi} = -\boldsymbol{F}_{\boldsymbol{r}} \cdot \boldsymbol{n}. \tag{2.40}$$

2.3.6 Force and torque balance at the boundaries

The boundary terms coming from the free energy variation must balance the external forces applied on the filament. Therefore equation (2.23) must hold. In which case, for arbitrary rates of change of the variables at the boundaries, the following equations follow at the basal boundary:

$$0 = -T_0^{\Delta} + k_0^{\Delta} \left(\Delta(0,t) - \Delta_0\right) - M_{\Delta}(0,t), \tag{2.41}$$

$$0 = -T_0^{\psi} + k_0^{\psi} \left(\psi(0,t) - \psi_0\right) - M_{\psi}(0,t), \tag{2.42}$$

$$0 = -\boldsymbol{F}_0^{\mathrm{ext}} - \boldsymbol{F}_{\boldsymbol{r}}(0,t), \tag{2.43}$$

while for the distal boundary we have:

$$0 = -T_L^{\Delta} + k_L^{\Delta}\left(\Delta(L,t) - \Delta_L\right) + M_{\Delta}(L,t), \tag{2.44}$$
$$0 = -T_L^{\psi} + k_L^{\psi}\left(\psi(L,t) - \psi_L\right) + M_{\psi}(L,t), \tag{2.45}$$
$$0 = -\boldsymbol{F}_L^{\text{ext}} + \boldsymbol{F}_{\boldsymbol{r}}(L,t). \tag{2.46}$$

2.4 DYNAMICS OF AN ACTIVE FILAMENT

2.4.1 EQUATIONS OF MOTION

As said previously, the variables C, Δ, ψ and $\boldsymbol{r}$ are not independent, but are related to each other through geometrical constraints. We now reduce the number of dynamical equations to a single equation of motion for the filament's shape. Replacing the curvature C by the derivative of the shear, and rearranging equations (2.37,2.38), we get two expressions for the Lagrange multipliers M_{ψ} and M_{Δ}:

$$\partial_s M_{\Delta} = \xi_{\Delta}\partial_t\Delta + \xi_{C,\Delta}\partial_t\partial_s\Delta + \kappa_{\Delta}\Delta + \kappa_{C,\Delta}\partial_s\Delta + m_{\text{a}}, \tag{2.47}$$
$$M_{\psi} + M_{\Delta} = \xi_C\partial_t\partial_s\Delta + \xi_{C,\Delta}\partial_t\Delta + \kappa_C\partial_s\Delta + \kappa_{C,\Delta}\Delta. \tag{2.48}$$

We introduce the line tension $F_{\|}$, and the normal force $F_{\perp}$, defined as the tangential and normal components of $\boldsymbol{F}_{\boldsymbol{r}}$:

$$F_{\|} = \boldsymbol{F}_{\boldsymbol{r}} \cdot \boldsymbol{t}, \tag{2.49}$$
$$F_{\perp} = \boldsymbol{F}_{\boldsymbol{r}} \cdot \boldsymbol{n}. \tag{2.50}$$

Using relation (2.40) and equations (2.47,2.48) yields an expression for the normal force:

$$\begin{aligned} F_{\perp} = (\xi_{\Delta} - (\partial_s\xi_{C,\Delta}))\partial_t\Delta + (\kappa_{\Delta} - (\partial_s\kappa_{C,\Delta}))\Delta + m_{\text{a}} \\ - \partial_s\left(\xi_C\partial_t\partial_s\Delta + \kappa_C\partial_s\Delta\right). \end{aligned} \tag{2.51}$$

When internal friction forces exist, the normal force is a differential operator acting on the shear, such that $F_{\perp} = \mathrm{F}_{\perp}(\partial_t, \partial_s)\Delta$. Taking the time derivative of the incompressibility constraint $\partial_s\boldsymbol{r} = \boldsymbol{t}$ we find the following equations:

$$\boldsymbol{t} \cdot \partial_s\partial_t\boldsymbol{r} = 0, \tag{2.52}$$
$$\boldsymbol{n} \cdot \partial_s\partial_t\boldsymbol{r} = \partial_t\psi. \tag{2.53}$$

Equation (2.52) is equivalent to $\partial_t \boldsymbol{t}^2 = 0$, and encodes the local force balance on the filament. Using Equation (2.39) we find the following partial differential equation:

$$\begin{aligned}\partial_s\left(\xi_\parallel^{-1}\partial_s F_\parallel\right) - \xi_\perp^{-1}\left(\partial_s\psi\right)^2 F_\parallel \\ = F_\perp \partial_s(\xi_\parallel^{-1}\partial_s\psi) + \left(\xi_\parallel^{-1} + \xi_\perp^{-1}\right)\left(\partial_s\psi\right)\partial_s F_\perp .\end{aligned} \tag{2.54}$$

Equation (2.53) yields another partial differential:

$$\begin{aligned}\partial_t\psi - \partial_s\left(\xi_\perp^{-1}\partial_s F_\perp\right) - \xi_\parallel^{-1}\left(\partial_s\psi\right)^2 F_\perp \\ = F_\parallel \partial_s(\xi_\perp^{-1}\partial_s\psi) + \left(\xi_\perp^{-1} + \xi_\parallel^{-1}\right)\left(\partial_s\psi\right)\partial_s F_\parallel .\end{aligned} \tag{2.55}$$

Equations (2.51,2.54), in conjunction with with boundary conditions (2.41–2.46), are partial differential equations coupling the line tension profile $F_\parallel$ to the time–evolutions of Δ and ψ.

2.4.2 FORCE AND MOMENT BALANCES

The global force balance is given by integrating equation (2.39) over the filament length, using boundary conditions (2.43, 2.46):

$$\int_0^L \mathrm{d}s' \Xi_{\boldsymbol{r}} \partial_t \boldsymbol{r} = \boldsymbol{F}_L^{\text{ext}} + \boldsymbol{F}_0^{\text{ext}} . \tag{2.56}$$

The global torque balance is given by integrating equations (2.40,2.39) over the entire filament:

$$\begin{aligned}T_0^\psi + T_L^\psi - k_0^\psi\left(\psi(0) - \psi_0\right) - k_L^\psi\left(\psi(L) - \psi_L\right) \\ = \int_0^L \mathrm{d}s' \boldsymbol{n}(s') \cdot \left(\boldsymbol{F}_L^{\text{ext}} - \int_0^{s'} \mathrm{d}s'' \Xi_{\boldsymbol{r}} \partial_t \boldsymbol{r}\right) .\end{aligned} \tag{2.57}$$

2.4.3 THE ACTIVE MOMENT

The last ingredient in need to be specified are the active forces. As remarked in the introduction, there are many different approaches. A particularly fruitful approach is to assume a specific form for the active forces in Fourier space [78–82]. Another approach, is to write an explicit time-evolution equation, using symmetry considerations. In 1894, Pierre Curie stated in his seminal paper *Sur la symétrie dans les phénomènes physiques* [112]:

> Lorsque certaines causes produisent certains effets, les éléments de symétrie des causes doivent se retrouver clans les effets produits.
>
> Lorsque certains effets révèlent une certaine dissymètrie, cette dissymétrie doit se retrouver dans les causes qui lui ont donné naissance

Which we translate as:

> When certain causes produce certain effects, the elements of symmetry of the causes must be found in the produced effects.
>
> When certain effects show some asymmetry, this asymmetry must be found in the causes which gave it birth.

In particular, the forces acting on the system variables must obey the same symmetries as these variables. Furthermore, the force cannot obey these symmetries if its evolution equation breaks them; however, if the evolution equation of the active forces obeys the symmetries, the active forces themselves also obeys them.

We construct the dynamical equation for the moment density field m_a which appears in equation 2.32 from the symmetry principles outlined above by Pierre Curie. The active moment density field m_a obeys the same symmetries as its rate of change $\partial_t m_\mathrm{a}$, with the exception of time reversal symmetry, and its conjugate variable, the shear Δ. The symmetries are given in Table 2.a. Because of rotational invariance, and mirror symmetry, only odd powers of the shear, the curvature, and their derivatives, are allowed to play a role in the time evolution of m_a. The tangent and normal vectors could also appear in scalar products, however we do not consider such terms. In this way, infinitely many terms may be added. However, it is important to keep in mind, that we do not know the precise mechanisms behind the behaviour of the active moment. Therefore, while the addition of more terms might generate more realistic beating patterns, they might not increase our understanding of the phenomena we aim to study. Up to linear order, we only add terms which are necessary and sufficient for the existence of an oscillatory instability. For example, the rate of change of the active moment must have term taking into account the effect of the filament configuration, and a relaxation term, if the former is proportional to the shear, then an oscillatory instability does not always exist (see Appendix D.)

Taking into account the previous considerations, the linear equation of motion for the active moment density field m_a is:

$$\partial_t m_\mathrm{a} = k_\mathrm{a} \partial_s \Delta - k_\mathrm{d} m_\mathrm{a}. \tag{2.58}$$

The above equation describes an active moment which senses the filament configuration through a curvature control mechanism; moments are generated in regions of high curvature with a phase difference due to a time-lag. The phase difference then drives the filament in areas of lower curvature, thus generating propagating bending-waves. Equations (2.54, 2.55, 2.58) and the boundary conditions (2.41 – 2.46) fully specify the nonlinear dynamics of an active filament.

CHAPTER 3

BEATING OF HOMOGENEOUS ACTIVE FILAMENTS

3.1 LINEARISED DYNAMICAL EQUATIONS

The general theory, presented in the previous chapter, describes the nonlinear dynamics of an arbitrary, heterogeneous filament. In order to study the oscillatory instability thresholds which such systems might display, it is more convenient to use linearised equations of motion, because near a bifurcation the nonlinear terms are small. For the sake of simplicity, in this section, the framework is applied to the linear dynamics homogeneous filaments, subject to neither external forces nor torques, with a basal shear elasticity.

A homogeneous filament is characterised by an additional symmetry: the translation along the centreline arc-length leaves the dynamical equations, as well as the parameters of the system, unchanged. Therefore the rigidities, the internal dissipations, as well as the width of the filament, are all constant. Because the fluid friction depends locally on the filament width, it is also constant. It is important to note that homogeneity does not imply isotropy: the filament remains polar.

The linearised local force balance, in a homogeneous filament, follows the equation $\partial_s^2 F_\parallel = 0$. Because there are no external forces acting at either end of the filament, the tension vanishes along the entire filament:

$$F_\parallel = 0. \tag{3.1}$$

The local moment balance can also easily be obtained from equation 2.55, and takes the form of an advection equation:

$$\xi_\perp \partial_t \psi = -\partial_s j, \tag{3.2}$$

where $j = -\partial_s F_\perp$ is the angular momentum density current. While the above form of the equation is concise, it is more interesting to write it explicitly, by using equation (2.51), which leads to a fourth order, parabolic, partial differential equation:

$$\xi_\perp \partial_t \psi - \xi_\Delta \partial_s^2 \partial_t \psi + \xi_C \partial_s^4 \partial_t \psi = \kappa_\Delta \partial_s^2 \psi - \kappa_C \partial_s^4 \psi + \partial_s^2 m_\mathrm{a}. \tag{3.3}$$

The dynamical equation governing the evolution of the active moments remains, to linear order, unchanged:

$$\partial_t m_{\mathrm{a}} = k_{\mathrm{a}} \partial_s \Delta - k_{\mathrm{d}} m_{\mathrm{a}}. \tag{3.4}$$

The above equations require four boundary condition. In the case of the homogeneous filament, the absence of external forces at the boundaries yields two boundary conditions:

$$\xi_\Delta \partial_t \Delta(0,t) + \kappa_\Delta \Delta(0,t) + m_{\mathrm{a}}(0,t) = \partial_s(\xi_C \partial_t \partial_s \psi(0,t) + \kappa_C \partial_s \psi(0,t), \tag{3.5}$$

$$\xi_\Delta \partial_t \Delta(L,t) + \kappa_\Delta \Delta(L,t) + m_{\mathrm{a}}(L,t) = \partial_s(\xi_C \partial_t \partial_s \psi(L,t) + \kappa_C \partial_s \psi(L,t); \tag{3.6}$$

the absence of torques at the boundaries results in the following two boundary conditions:

$$\xi_C \partial_t \partial_s \psi(0,t) + \xi_{C,\Delta} \partial_t \Delta(0,t) + \kappa_C \partial_s \psi(0,t) + \kappa_{C,\Delta} \Delta(0,t) = k_\Delta \Delta(0,t) \tag{3.7}$$

$$\xi_C \partial_t \partial_s \psi(L,t) + \xi_{C,\Delta} \partial_t \Delta(L,t) + \kappa_C \partial_s \psi(L,t) + \kappa_{C,\Delta} \Delta(L,t) = 0. \tag{3.8}$$

The momentum balance (3.3) displays different dynamical regimes, defined by the relative magnitudes of the frictional coefficients, with the wavelengths of the oscillations. This can be readily seen with the spatial Fourier transformation of the left-hand side of the momentum balance equation, which takes the form:

$$\xi_\perp \left(1 + \frac{\xi_\Delta}{\xi_\perp} q^2 \left(1 + \frac{\xi_C}{\xi_\Delta} q^2\right)\right) \partial_t \tilde{\psi} = -\bar{q}^2 \left(\kappa_\Delta \tilde{\psi} - \kappa_C \bar{q}^2 \tilde{\psi} + \tilde{m}_{\mathrm{a}}\right). \tag{3.9}$$

The ratios $\sqrt{\xi_\Delta/\xi_\perp}$ and $\sqrt{\xi_C/\xi_\Delta}$ define length-scales characterising the dynamics of the active filament. Travelling waves on the filament are dominated by different friction mechanisms depending on their wavenumbers, which define the length $\ell = 1/q$. Indeed, for a given value of the ratio $\xi_\Delta/\xi_\perp$, the effect of external friction is large if the length ℓ is large enough so that $\xi_\Delta/\xi_\perp < \ell^2$. The effect of internal friction becomes larger for smaller values of ℓ, when $\xi_\Delta/\xi_\perp > \ell^2$ holds. Likewise, the dominant internal friction is fixed by whether ξ_C/ξ_Δ is larger or smaller than ℓ. If $\xi_C/\xi_\Delta < \ell^2$ then shear friction is dominant.

We study three limiting cases: the case of dominant external friction, where the ratio $\xi_\Delta/\xi_\perp \ll \ell^2$; the case of dominant shear friction, where $\xi_\Delta/\xi_\perp \gg \ell^2$ and $\xi_C/\xi_\Delta \ll \ell^2$; the case of dominant curvature friction, where $q^2\xi_\Delta/\xi_\perp \gg 1$ and $\xi_C/\xi_\Delta \gg \ell^2$. These limiting cases are considerably simpler than the mixed friction regimes, because the boundary conditions in the dominant external and shear friction cases are not dynamic, but static. The dominant curvature friction case retains a

Dimensionless time	$\bar{t} = k_{\mathrm{d}} t$
Dimensionless arc-length	$\bar{s} = \dfrac{s}{\mu_\perp}$
Dimensionless shear rigidity	$\bar{\kappa}_\perp = \dfrac{\kappa_\Delta}{\kappa_C} \mu_\perp^2$
Control parameter	$\bar{\Omega}_\perp = \dfrac{k_{\mathrm{a}}}{k_{\mathrm{d}}} \dfrac{\mu_\perp}{\kappa_C}$
Dimensionless active moment	$\bar{m}_\perp = \dfrac{k_{\mathrm{d}}}{k_{\mathrm{a}} \mu_\perp} m_{\mathrm{a}}$
Dimensionless filament length	$\bar{L}_\perp = \frac{L}{\mu_\perp}$
Dimensionless basal shear rigidity	$\bar{k}_\perp = \frac{k_\Delta \mu_\perp}{\kappa_C}$

Table 3.a: Dimensionless parameters in the limit of dominant external friction

dynamic boundary condition. The linear stability of each case are analysed, and numerical solutions are shown if applicable. Before proceeding, we further simplify the system by neglecting the cross-couplings $\xi_{C,\Delta}$ and $\kappa_{C,\Delta}$, which until now only appear in the boundary conditions.

It is important to note that in the case of high internal friction, the equations of motion are linear, not due to a small amplitude expansion, but because of the fact that the nonlinearities are geometrical, and describe the shape-dependent movement of the filament embedded in a plane. Therefore, when external friction is neglected, these affects are also neglected.

3.2 Analysis of the filament's beating

Before analysing specific limiting cases of equation (3.3), we define some important tools, used later for the analysis of the properties filament's dynamics. The period of the filament beating is obtained by a Fourier transform of the beating signal at the middle of the filament, the maximum intensity gives the first mode frequency $f = \tilde{\omega}/2\pi$, and the period is $T = 1/f$. Because in this chapter we remain very close to the instability threshold, the waves are dominated by their first mode. Taking the Fourier transform of the tangent angle one obtains:

$$\tilde{\psi}(s,\tilde{\omega}) = \int_{t_0}^{t_0+T} \mathrm{d}t'\psi(s,t')\mathrm{e}^{-\mathrm{i}\tilde{\omega}t'}, \tag{3.10}$$

where the transform $\tilde{\psi}(s,\tilde{\omega})$ is a complex number, and has the form $\tilde{\psi}(s,\tilde{\omega}) = |\tilde{\psi}|\exp(-\mathrm{i}\phi(s,\tilde{\omega}))$, and where t_0 is large enough so that the oscillations are in the limit-cycle. The phase is obtained by taking the natural logarithm:

$$\phi(s,\tilde{\omega}) = \mathrm{i}\ln\left(\frac{\tilde{\psi}(s,\tilde{\omega})}{|\tilde{\psi}|}\right). \tag{3.11}$$

We relate the local wave vector to the phase as:

$$\tilde{q}(s,\tilde{\omega}) = -\partial_s\phi(s,\tilde{\omega}). \tag{3.12}$$

Finally, from the phase we can define the phase velocity as:

$$v(s,\tilde{\omega}) = \frac{\tilde{\omega}}{\tilde{q}(s,\tilde{\omega})}. \tag{3.13}$$

During the analysis of the numerical solutions of the equations of motion in different limits, we plot the real and complex part of the transform with respect to s at the measured frequency, the phase as well as the phase speed. In the following sections the analysis is done in dimensionless units, because ϕ is dimensionless by construction, the above definitions apply with no modification.

3.3 LIMIT OF DOMINANT EXTERNAL FRICTION

The limit of dominant external friction has been extensively studied, and, as seen in the introduction, has been the case most often considered historically, as well as the first one to be studied theoretically, by K.E. Machin in 1958. Our approach differs from most others by an explicit modelling of the active moments m_a, it is however not unique, Hines and Blum in 1978 studied similar dynamics [86]. The equations of motion can be written in an dimensionless form, using $1/k_\mathrm{d}$ as our unit time and $\mu_\perp = (\kappa_C/(\xi_\perp k_\mathrm{d}))^{1/4}$ as our unit length, as:

$$\partial_{\bar{t}}\psi = -\partial_{\bar{s}}^4\psi + \bar{\kappa}_\perp\partial_{\bar{s}}^2\psi + \bar{\Omega}_\perp\partial_{\bar{s}}^2\bar{m}_\perp, \tag{3.14}$$

$$\partial_{\bar{t}}\bar{m}_\perp = \partial_{\bar{s}}\psi - \bar{m}_\perp, \tag{3.15}$$

where $\bar{t}$ and $\bar{s}$ are the dimensionless time and arc-length, while $\bar{\kappa}_\perp = \mu_\perp^2 \kappa_\Delta/\kappa_C$ is a parameter whose magnitude encodes the strength of the shear rigidity, $\bar{\Omega}_\perp = k_\text{a}\mu_\perp/(k_\text{d}\kappa_C)$ is a control parameter, and $\bar{m}_\perp = k_\text{d} m_\text{a}/(k_\text{a}\mu_\perp)$ is the dimensionless active moment. Their expressions as function of the dimensional parameters can be seen in Table 3.a. The boundary conditions are:

$$\bar{\kappa}_\perp \Delta(0,\bar{t}\,) + \bar{\Omega}_\perp \bar{m}_\perp(0,\bar{t}\,) = \partial_{\bar{s}}^2 \psi(0,\bar{t}\,), \tag{3.16}$$

$$\bar{\kappa}_\perp \Delta(\bar{L}_\perp,\bar{t}\,) + \bar{\Omega}_\perp \bar{m}_\perp(\bar{L}_\perp,\bar{t}\,) = \partial_{\bar{s}}^2 \psi(\bar{L}_\perp,\bar{t}\,), \tag{3.17}$$

$$\partial_s \bar{\psi}(0,\bar{t}\,) = \bar{k}_\perp \Delta(0,\bar{t}\,), \tag{3.18}$$

$$\partial_s \bar{\psi}(\bar{L}_\perp,\bar{t}\,) = 0. \tag{3.19}$$

3.3.1 STABILITY ANALYSIS

We look for an oscillatory instability in the limit of dominant external friction. In order to do so we solve the eigenvalue problem associated with the equations of motion (3.14, 3.15), using the ansatz $\psi = \tilde{\psi}\exp(-\bar{q}\bar{s}+\bar{\omega}\bar{t}\,)$ and $m_\text{a} = \tilde{m}\exp(-\bar{q}\bar{s}+\bar{\omega}\bar{t}\,)$, where $\bar{q}$ is the complex wave-vector, and $\bar{\omega}$ is the complex angular frequency, respectively. The choice of q and ω as the ansatz, instead of the more common choice of $\mathrm{i}\bar{q}$ and $\mathrm{i}\bar{\omega}$, is perhaps an odd one. The reason for that choice is the following: finite linear systems can have diverging modes for both the wave-vector and the angular frequency, it is slightly more straightforwards in these cases to have the positive real part correspond to diverting modes, rather than the negative imaginary part, and likewise for the negative real part corresponds to relaxing modes instead of the positive imaginary part. Inserting the ansatz in the equations of motion, we find the complex dispersion relation:

$$\bar{q}^4 + \frac{\bar{\Omega}_\perp}{1+\bar{\omega}}\bar{q}^3 - \bar{\kappa}_\perp\bar{q}^2 + \bar{\omega} = 0. \tag{3.20}$$

The complex dispersion relation has the symmetry $\{\bar{q},\bar{\Omega}_\perp\} \to \{-\bar{q},-\bar{\Omega}_\perp\}$. Because under such a transformation the angular frequency remains unchanged, a change in the sign of the control parameters changes the direction of wave propagation. This is in contrast with previous theories of flagellar beat, where the direction of the wave propagation is controlled by the boundary conditions [81, 82]. Furthermore the dispersion relation admits the trivial solution $\{\bar{q}=0,\bar{\omega}=0\}$, corresponding to a uniform static angle profile.

We first study the stability of an infinitely long filament, in which case there are no boundary conditions. For a finite value of $\bar{q}$, two non-trivial solution for the angular frequency exist and are:

$$\bar{\omega}_{\pm} = \frac{1}{2}\left(-1 + \bar{\kappa}_{\perp}\bar{q}^2 - \bar{q}^4 \pm \sqrt{(1 + \bar{\kappa}_{\perp}\bar{q}^2 - \bar{q}^4)^2 - 4\bar{\Omega}_{\perp}\bar{q}^3}\right). \tag{3.21}$$

An infinitely long filament is unstable if, for a range wavenumbers and control parameters, there exists a range of angular frequencies with a positive real component. This can be easily seen by plotting the real part of $\bar{\omega}_+$ as a function of $\bar{q}$. Indeed, as seen in figure 3.1 for $\bar{\kappa}_{\perp} = 0$, above a critical value of $\bar{\Omega}_{\perp} \simeq 1.755$ there exists a region in which $\bar{\omega}_+$ has a positive real part. As $\bar{\kappa}_{\perp}$ increases, the critical value of $\bar{\Omega}_{\perp}$ also increases, and for $\bar{\kappa}_{\perp} = 1$ the critical value of the control parameter increases to $\bar{\Omega}_{\perp} \simeq 4.077$ thus demonstrating that shear rigidity inhibits beating. We can therefore conclude that an oscillatory instability does exist for an infinitely long filament. In the corresponding limit-cycle, the dominant mode corresponds to the most unstable wavevector q_*, with its associated angular frequency $\bar{\omega}_+(q_*)$ having a maximal real positive part. As shown in figure 3.1, the most unstable wavevector as a function of $\bar{\Omega}_{\perp}$ and $\bar{\kappa}_{\perp}$ remains of order one. As seen in figure 3.2, the transition is first order, and the angular frequency associated with the most unstable mode has a finite value at the onset of the instability.

The stability analysis of a filament of finite length is more complicated, and therefore done numerically. The equations of motion (3.14, 3.15) can be written as finite difference equations, whose eigenvalues correspond to the complex angular frequencies of the system. A finite filament displays an oscillatory instability if, by varying continuously the control parameter, we can go from a state in which no angular frequencies have positive real components, to a state in which a single pair of complex conjugate angular frequencies have a vanishing real component with a finite imaginary component. For a finite filament, boundary conditions play a key role, as the finite difference matrices must be modified accordingly. In the present case, we solve for the limit in which $\bar{k} \to \infty$, and $\bar{\kappa}_{\perp} \to 0$.

3.3.2 NUMERICAL SOLUTIONS

Numerical solutions of the equations of motion, near the onset of the instability, were obtained through an implicit-explicit finite-difference scheme. However, some precautions must be taken: because the dynamical equations are linear, they are unstable. In a real system, there exist physical mechanisms which stabilise the system, therefore preventing its divergence. Near the onset of the instability, for a low-amplitude description, this mechanism manifests itself as a relatively low order polynomial correction to the equations of motion. Without any knowledge of the microscopic details of a particular system, it is difficult to determine the precise form of the nonlinearity, as there is an infinite number of choices. The only constraints are that they must obey the symmetries of the system.

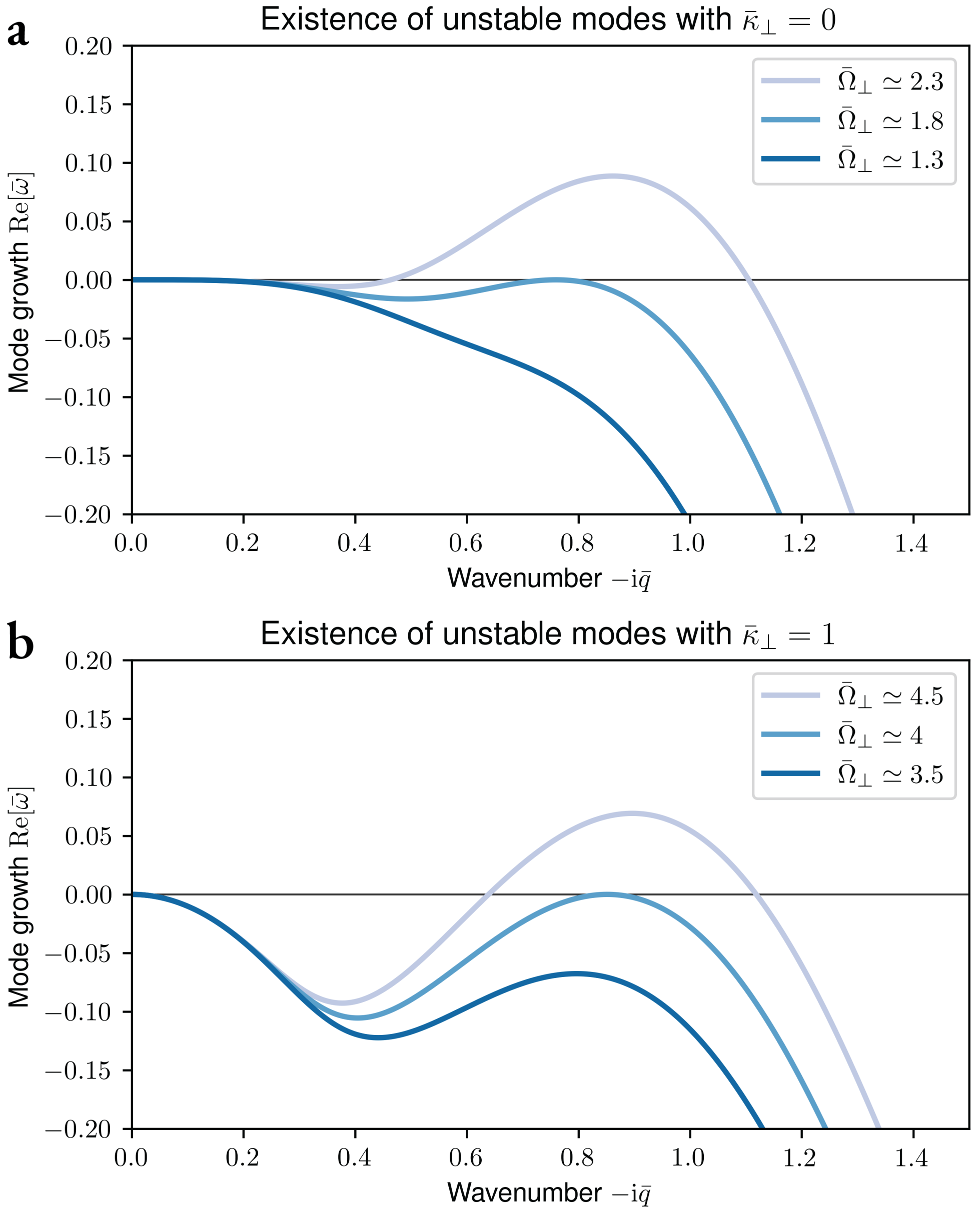

Figure 3.1: Stability of an infinite filament: (**a**) Mode growth as a function of the wavenumber for different values of the control parameter and at $\bar{\kappa}_\perp = 0$ (**b**) Mode growth as a function of the wavenumber for different values of the control parameter and at $\bar{\kappa}_\perp = 1$. The wavenumber corresponding to the maxima of $\mathrm{Re}[\bar{\omega}]$ is $\bar{q}_*$

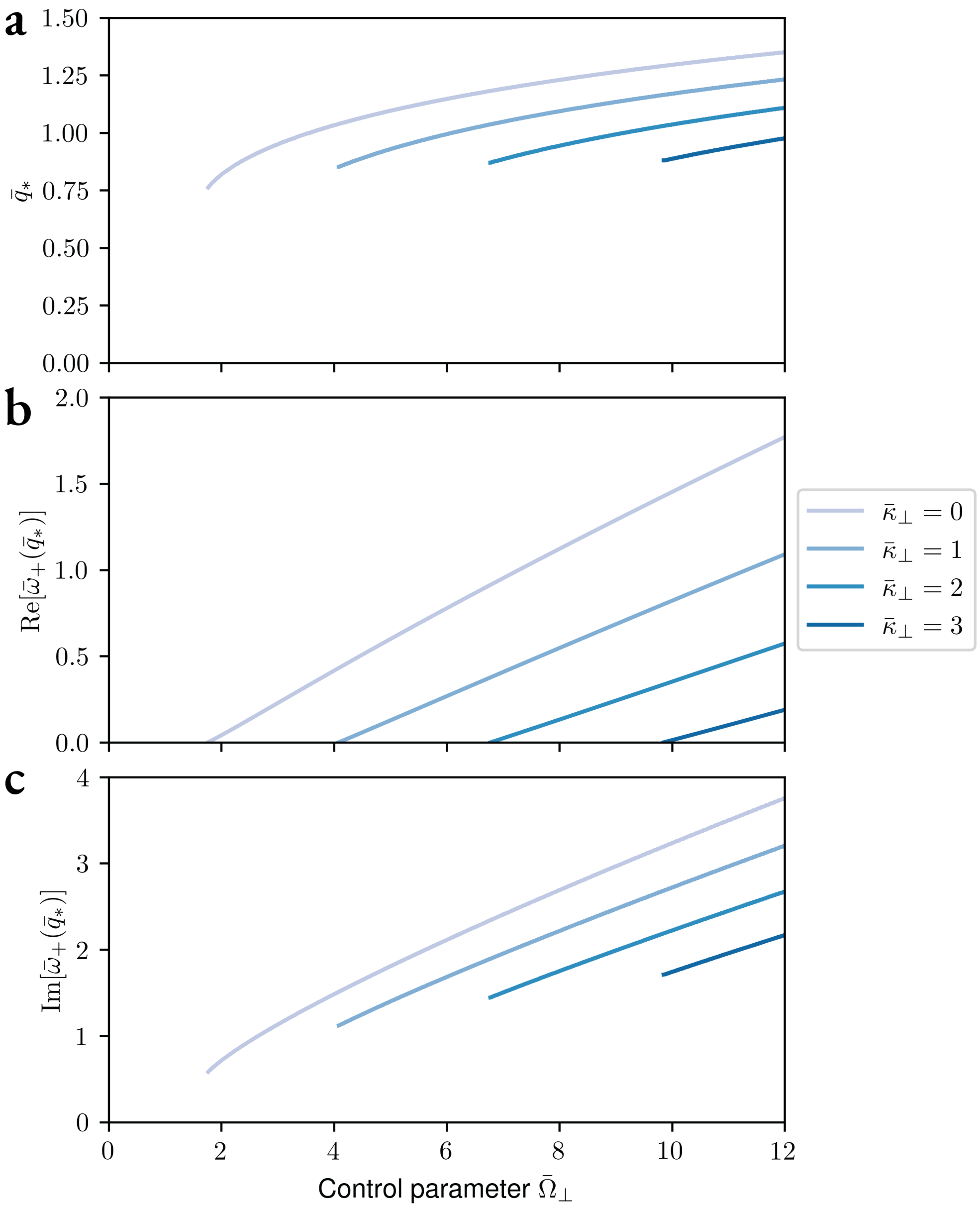

Figure 3.2: Properties of the most unstable mode as a function of $\bar{\Omega}_\perp$ (**a**) wave vector $\bar{q}_*$ (**b**) real part of the angular frequency (**c**) imaginary part of the angular frequency

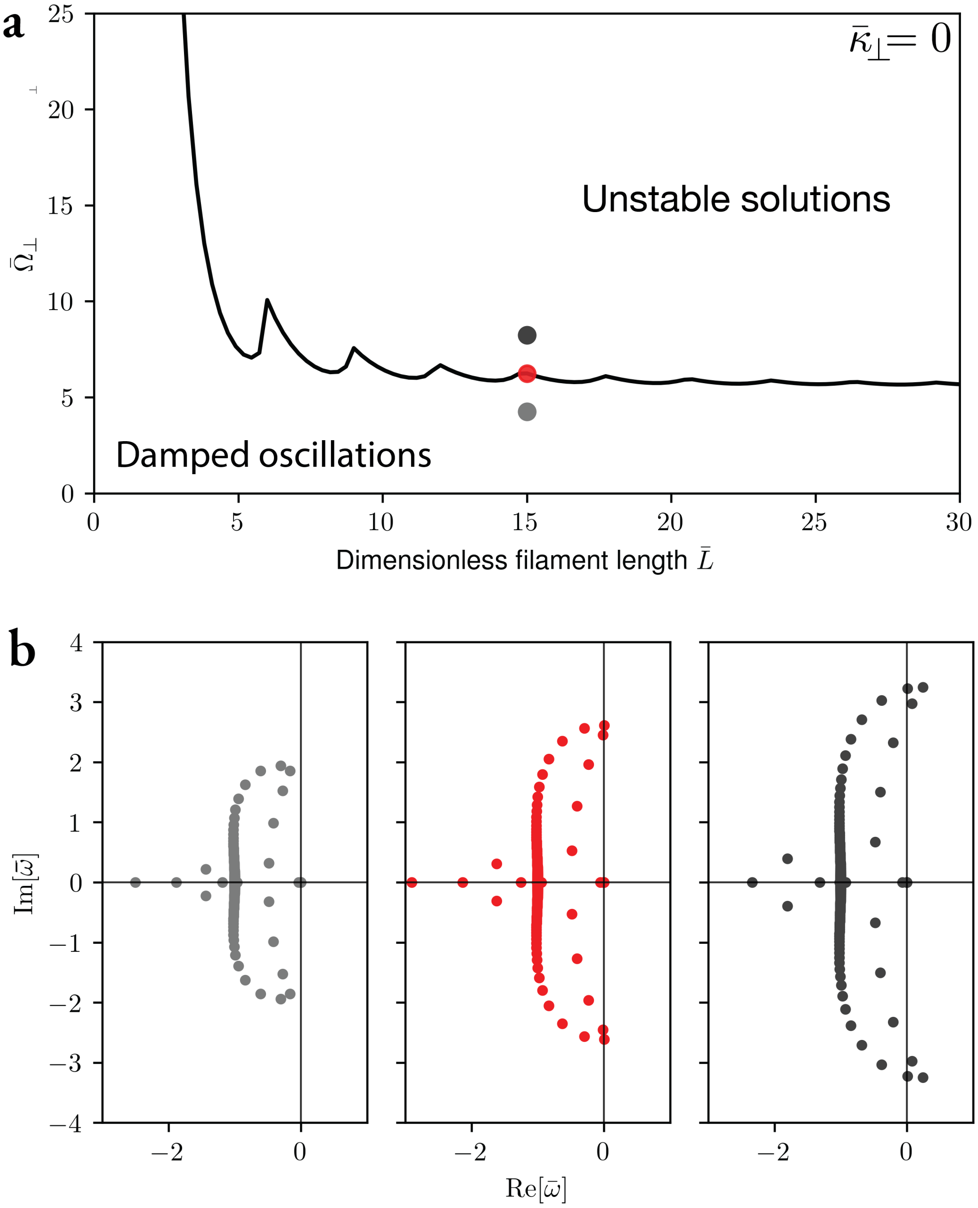

Figure 3.3: Stability of a finite length filament: (**a**) onset of the instability as a function of the length $\bar{L}_\perp$, above the black line the region is unstable, below the oscillations are damped (**b**) angular frequency distribution in the complex plane for a filament of length $\bar{L}_\perp = 15$, light grey case $\bar{\Omega}_\perp \simeq 4.2$ has only stable modes, its position in the phase space is also marked by a light grey dot in figure (a), red case $\bar{\Omega}_\perp \simeq 6.2$ has one pair of unstable modes, its position in the phase space is marked by a red dot in figure(a), dark grey case $\bar{\Omega}_\perp \simeq 8.2$, has unstable modes, its position in the phase space is marked by a dark grey dot in figure (a).

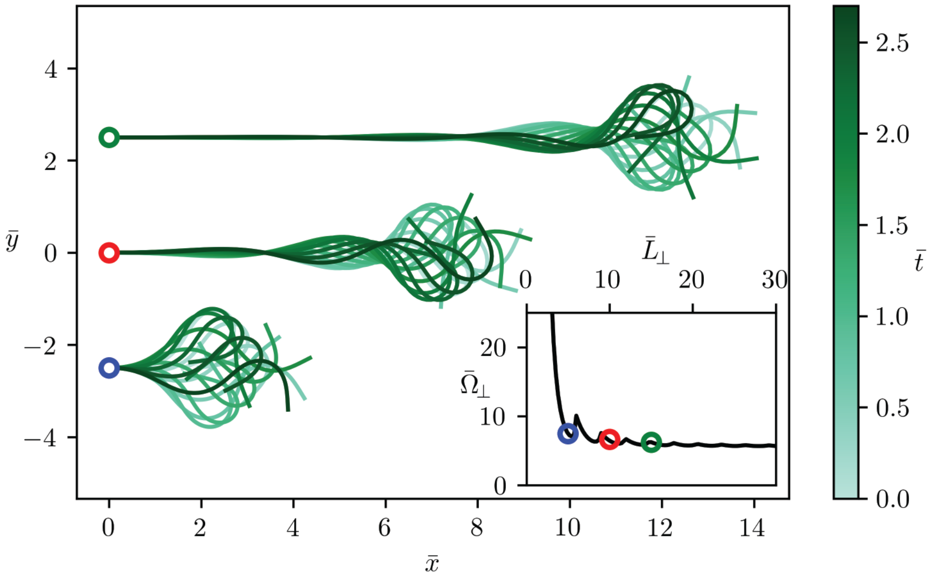

Figure 3.4: Beating patterns of a filament of different lengths, with no shear rigidity $\bar{\kappa}_\perp = 0$. The upper, longer filament, marked with a green dot ○, is of length $\bar{L}_\perp = 15$, $\bar{\Omega}_\perp \simeq 6.2$ and $\epsilon = 0.08$. The middle filament, marked with a red dot ○, is of length $\bar{L}_\perp = 10$, $\bar{\Omega}_\perp \simeq 6.6$ and $\epsilon = 0.1$. The lowermost filament, marked with a blue dot ○, is of length $\bar{L}_\perp = 5$, $\bar{\Omega}_\perp \simeq 7.5$ and $\epsilon = 0.15$. Their positions in the phase space are marked with their respective coloured dots in the lower right quadrant. For more details on the phase space see figure 3.3. Here $\bar{x} = x/\mu_\perp$ and $\bar{y} = y/\mu_\perp$, are the dimensionless units of the euclidean plane.

For the purpose of finding numerical solutions, this nonlinearity is of fundamental importance, as otherwise there is no limit cycle. Keeping this in mind, we choose a simple nonlinear cubic term to stabilise the equations of motion, which we add to the active moment equation:

$$\partial_{\bar{t}}\bar{m}_\perp = \partial_{\bar{s}}\psi - \bar{m}_\perp - \epsilon\bar{m}_\perp^3. \tag{3.22}$$

Near the threshold of the instability, the nonlinearity sets the amplitude of the waves. We choose to simulate filaments with vanishing basal shear elasticity ($\bar{k}_\perp = 0$) and no internal shear rigidity ($\bar{\kappa}_\perp = 0$). Because there are no external torques at either side of the filament, the basal tangent-angle is 0 $\psi(0) = 0$. We remain close to the threshold, therefore all effects are linear. Filaments of three different lengths were chosen, with $\bar{L}_\perp = 5, 10, 15$. We first show the shape of the oscillations, which can be seen in figure 3.4. For longer filaments, the amplitudes of the oscillations are small

Dimensionless time	$\bar{t} = k_\mathrm{d} t$
Dimensionless arc-length	$\bar{s} = \dfrac{s}{\mu_\Delta}$
Dimensionless shear rigidity	$\bar{\kappa}_\Delta = \dfrac{\kappa_\Delta}{\kappa_C} \mu_\Delta^2$
Control parameter	$\bar{\Omega}_\Delta = \dfrac{k_\mathrm{a}}{k_\mathrm{d}} \dfrac{\mu_\Delta}{\kappa_C}$
Dimensionless active moment	$\bar{m}_\Delta = \dfrac{k_\mathrm{d}}{k_\mathrm{a} \mu_\Delta} m_\mathrm{a}$
Dimensionless filament length	$\bar{L}_\Delta = \frac{L}{\mu_\Delta}$
Dimensionless basal shear rigidity	$\bar{k}_\Delta = \frac{k_\Delta \mu_\Delta}{\kappa_C}$

Table 3.b: Dimensionless parameters in the dominant shear friction case

at the beginning of the filament, before giving rise to higher amplitude oscillations. As shown in figure 3.5, the amplitudes are dominated by the first mode, with waves traveling from the base to the apex. Although the filament dynamics are described by linear equations, and dominated by the first Fourier mode, the phase velocity of the filament tangent-angle waves are nonlinear.

The infinitely long filament displays an instability at $\bar{\Omega}_\perp \sim 1.6$, yet the onset of the instability for a filament of finite length seems to reach a plateau of $\bar{\Omega}_\perp > 5$ as the length increases. How these two scenarios can be reconciled remains an open question.

3.4 LIMIT OF DOMINANT SHEAR FRICTION

We now consider the case of dominant shear friction. This is the limit when $q^2\xi_\Delta/\xi_\perp \gg 1$ and $q^2\xi_C/\xi_\Delta \ll 1$. We obtain a second order differential equation of motion, thus much simpler than the limit of dominant external friction. Because the external friction is neglected, only internal degrees of freedom remain, and all geometrical nonlinearities, describing external degrees of freedom, vanish. Therefore the equations of motion are linear, not because of a linearisation in the context of a small amplitudes development, but because of the properties of the system.

The equations of motion may also be written in a dimensionless form, using $1/k_\mathrm{d}$ as a unit time, and $\mu_\Delta = \sqrt{\kappa_C/(\xi_\Delta k_\mathrm{d})}$ as a unit length:

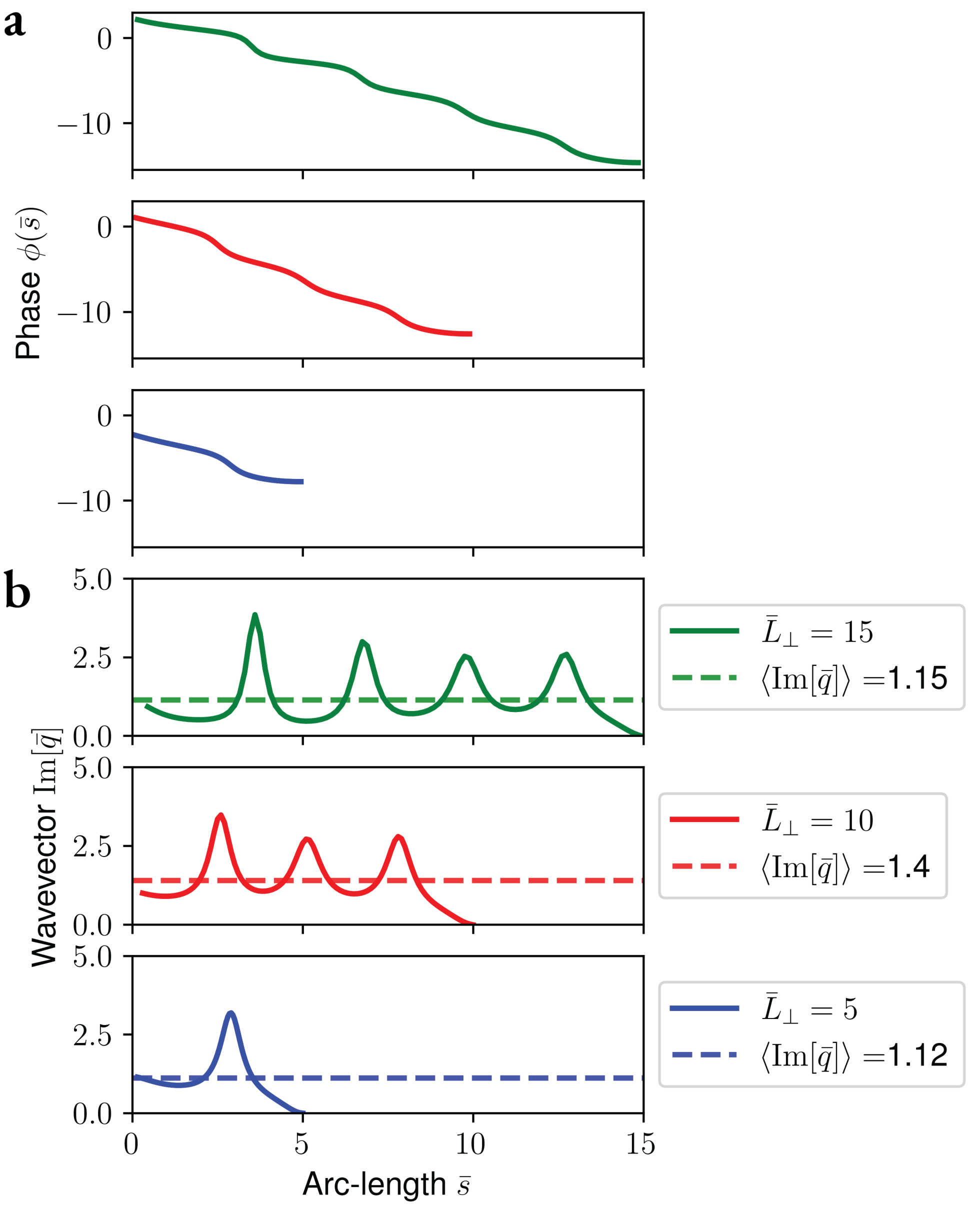

Figure 3.5: Properties of tangent angle waves $\psi(\bar{s}, \bar{t})$ in the limit of dominant external friction on filaments of length $\bar{L}_\perp \in \{5, 10, 15\}$, shown in green, red and blue, respectively: (**a**) phase, (**b**) wave vector, as defined in section 3.2 The brackets $\langle\cdot\rangle$ are averages over the filament length.

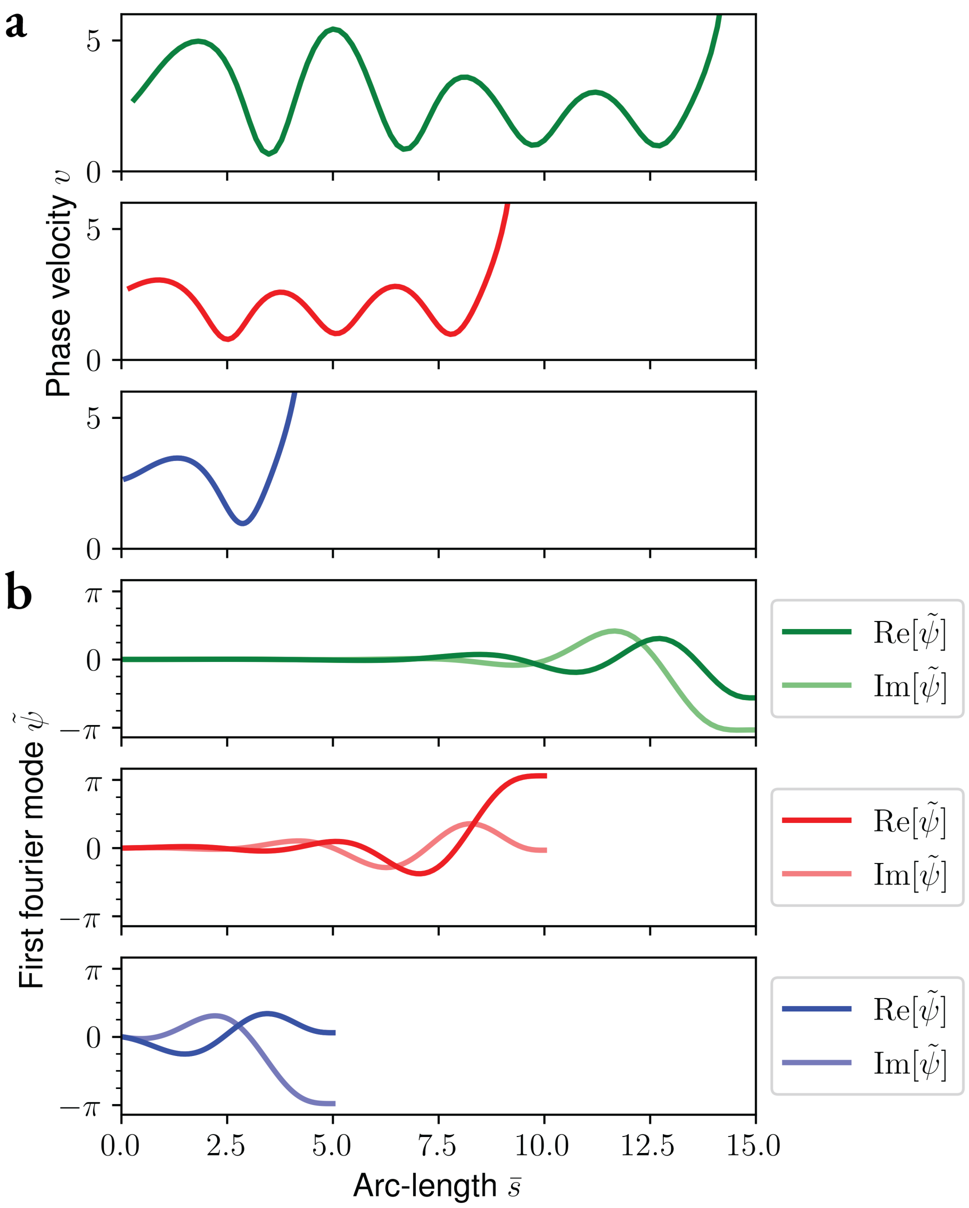

Figure 3.6: Properties of tangent angle waves $\psi(\bar{s},\bar{t})$ in the limit of dominant external friction on filaments of length $\bar{L}_{\perp} \in \{5, 10, 15\}$, shown in green, red and blue, respectively: (**a**) phase velocity, (**b**) first Fourier mode representation, as defined in section3.2.

$$\partial_{\bar{t}}\Delta = -\bar{\kappa}_{\Delta}\Delta + \partial_{\bar{s}}^{2}\Delta - \bar{\Omega}_{\Delta}\bar{m}_{\Delta}, \tag{3.23}$$

$$\partial_{\bar{t}}\bar{m}_{\Delta} = \partial_{\bar{s}}\Delta - \bar{m}_{\Delta}, \tag{3.24}$$

where $\bar{\kappa}_{\Delta} = \mu_{\Delta}^{2}\kappa_{\Delta}/\kappa_{C}$ is the dimensionless shear elasticity, $\bar{\Omega}_{\Delta} = k_{\mathrm{a}}\mu_{\Delta}k_{\mathrm{d}}^{-1}\kappa_{C}^{-1}$ the control parameter, and $\bar{m}_{\Delta} = k_{\mathrm{d}}m_{\mathrm{a}}/(k_{\mathrm{a}}\mu_{\Delta})$ the dimensionless active moment. The expressions of the dimensionless parameters are given as a function of their dimensional counterparts in Table 3.b. Because the equations of motion are second order, only two boundary conditions are needed:

$$\partial_{\bar{s}}\Delta(0,t) = \bar{k}_{\Delta}\Delta(0,t), \tag{3.25}$$

$$\partial_{\bar{s}}\Delta(\bar{L}_{\Delta},t) = 0. \tag{3.26}$$

These boundary conditions can be derived from the more general equations (3.5–3.8), the first two equations become, in the limit of dominant internal shear friction, identical to the equations of motion, while the second two equations result in the boundary condition written above. The parameter $\bar{k}_{\Delta}$ describes the basal shear rigidity of the filament. Because no external torque is present, $\psi(0) = 0$. For $\bar{k}_{\Delta} = 0$, the onset of the instability has an analytical closed form, as well as analytical solutions for the dynamics at the instability in the time-domain.

3.4.1 LINEAR STABILITY ANALYSIS

In order to extract the complex dispersion relation governing the propagation of waves in the active filament, we use the Laplace ansatz: $\Delta = \tilde{\Delta}\exp(-\bar{q}\bar{s} + \bar{\omega}\bar{t})$, and $\bar{m}_{\Delta} = \tilde{m}\exp(-\bar{q}\bar{s} + \bar{\omega}\bar{t})$. With $\bar{q}$ the *complex* wavenumber, $\bar{\omega}$ the complex angular frequency, $\tilde{\Delta}$ and $\tilde{m}$ the amplitudes. Substituting the ansatz into equations of motion (3.23–3.24), we find:

$$\bar{q}^{2} + \frac{\bar{\Omega}_{\Delta}}{1+\bar{\omega}}\bar{q} - \bar{\kappa}_{\Delta} - \bar{\omega} = 0. \tag{3.27}$$

As in the previous section, the complex dispersion relation is invariant upon the change of signs of the wave vector and the control parameter $\{\bar{q}, \bar{\Omega}_{\Delta}\} \rightarrow \{-\bar{q}, -\bar{\Omega}_{\Delta}\}$. Therefore the direction of wave propagation is given by the sign of $\bar{\Omega}_{\Delta}$.

LINEAR STABILITY OF AN INFINITELY LONG FILAMENT

Following the same procedure as in the previous section, we analyse the stability of travelling waves in an infinitely ling filament, in the limit of dominant shear friction. The complex angular frequencies as a function of the complex wavevectors are:

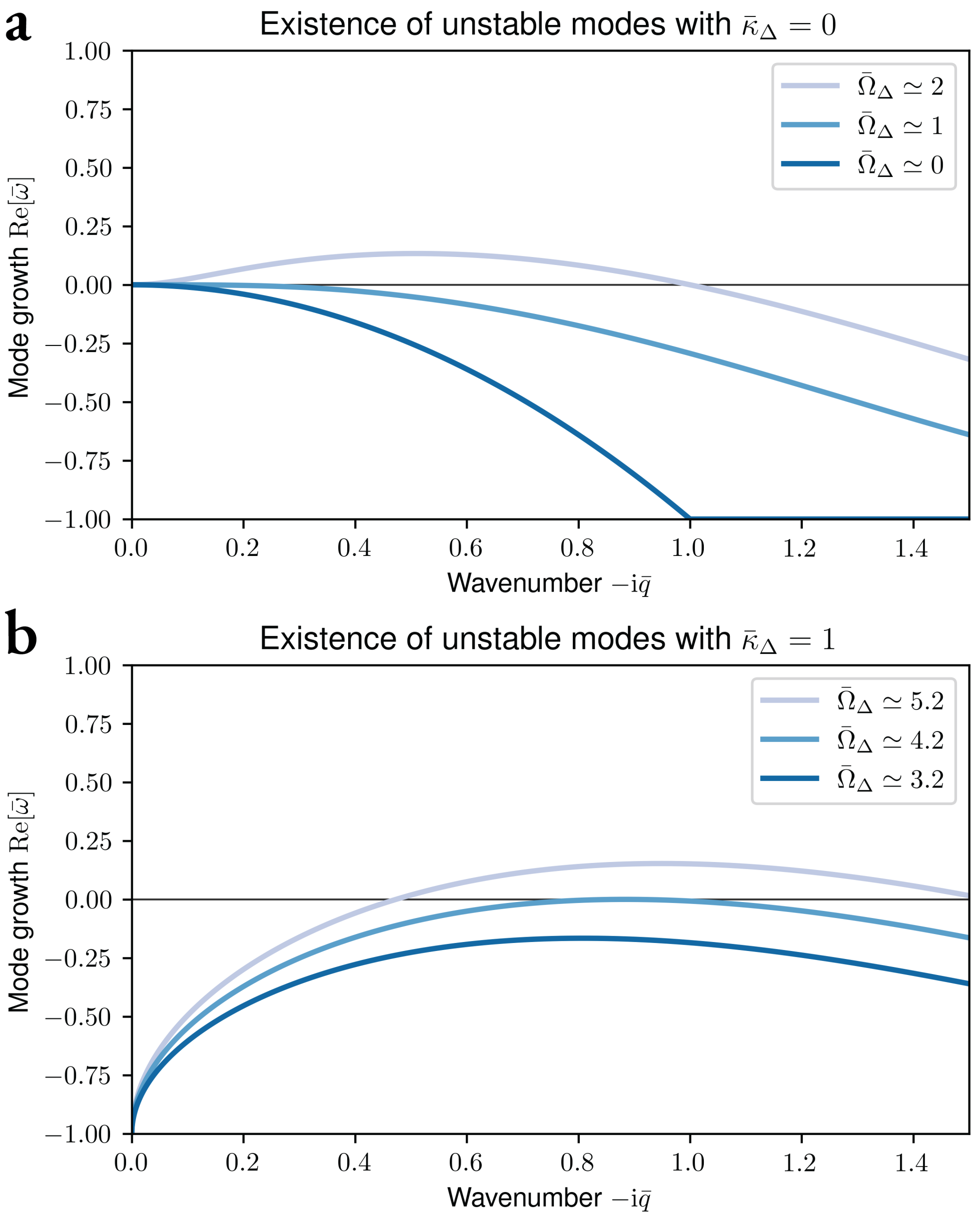

Figure 3.7: Stability of an infinite filament: (**a**) Mode growth as a function of the wavenumber for different values of the control parameter and at $\bar{\kappa}_\Delta = 0$ (**b**) Mode growth as a function of the wavenumber for different values of the control parameter and at $\bar{\kappa}_\Delta = 1$. The wavenumber corresponding to the maxima of $\mathrm{Re}[\bar{\omega}]$ is $\bar{q}_*$

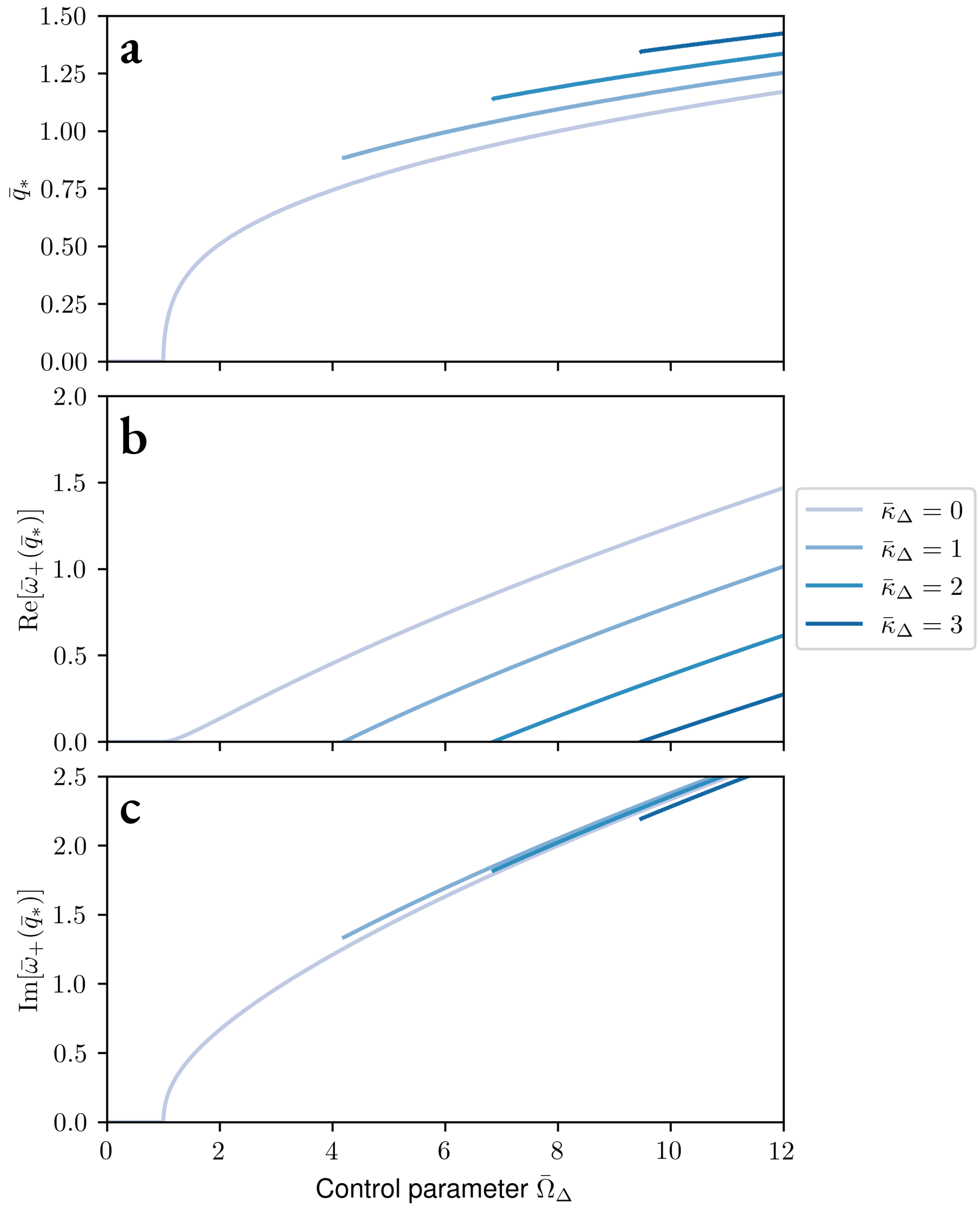

Figure 3.8: Properties of most unstable mode as a function of $\bar{\Omega}_\Delta$ (**a**) wave vector $\bar{q}_*$ (**b**) real part of the angular frequency (**c**) imaginary part of the angular frequency

$$\bar{\omega}_{\pm} = \frac{1}{2}\left(-1 - \bar{\kappa}_{\Delta} + \bar{q}^2 \pm \sqrt{\left(1 + \bar{\kappa}_{\Delta} - \bar{q}^2\right)^2 - 4\left(\bar{\kappa}_{\Delta} - \bar{q}^2 - \bar{\Omega}_{\Delta}\bar{q}\right)}\right). \quad (3.28)$$

Because the filament is infinitely long, the wavenumbers must be purely imaginary, that is $\mathrm{i}\bar{q} \in \mathbb{R}$. The filament presents an oscillatory instability, if, for some range of $-\mathrm{i}\bar{q}$ and $\bar{\Omega}_{\Delta}$, the real part of either $\bar{\omega}_{+}$ or $\bar{\omega}_{-}$ become positive. In this case, as seen in figure 3.7, for $\bar{\kappa}_{\Delta} = 0$, the real part of $\bar{\omega}_{+}$ becomes positive for any $\bar{\Omega}_{\Delta} > 1$. We call the most unstable mode the pair $\{\bar{q}_{*}, \bar{\omega}(\bar{q}_{*})\}$, such that $\mathrm{Re}[\bar{\omega}]$ is maximal. The system exhibits, for $\bar{\kappa}_{\Delta} = 0$, a second order transition, with the angular frequency $\mathrm{Im}[\bar{\omega}]$ associated to the most unstable wavenumber approaching 0 as $\bar{\Omega}_{\Delta}$ approaches its critical value of 1 as seen in figure 3.8.

Finite values of the shear elasticity inhibit beating, by increasing the critical value of $\bar{\Omega}_{\Delta}$ needed for the instability to occur. The transition becomes first order, as the most unstable wavenumber approaches a finite value as $\bar{\Omega}_{\Delta}$ approaches the onset of the instability.

Linear stability of a finite filament

In the case of a filament of finite length, the stability analysis is remarkably simple, and a number of quantities can be derived in an analytical form. Because the filament is of finite size, we solve the above dispersion relation for the complex wavenumber $\bar{q}$:

$$\bar{q}_{1,2}(\bar{\Omega}_{\Delta}, \bar{\kappa}_{\Delta}, \bar{\omega}) = -\frac{1}{2}\frac{\bar{\Omega}_{\Delta}}{1+\bar{\omega}} \pm \frac{1}{2}\sqrt{\left(\frac{\bar{\Omega}_{\Delta}}{1+\bar{\omega}}\right)^2 + 4\left(\bar{\omega} + \bar{\kappa}_{\Delta}\right)}. \quad (3.29)$$

Because there are two wavenumbers for each angular frequency, the shear and the active moment can be written as:

$$\Delta(\bar{s}, \bar{t}) = \sum_{\bar{\omega}\in S}\sum_{i\in\{1,2\}} \tilde{\Delta}_i \mathrm{e}^{-\bar{q}_i\bar{s}+\bar{\omega}\bar{t}} + \text{c.c.}, \quad (3.30)$$

$$\bar{m}_{\Delta}(\bar{s}, \bar{t}) = \sum_{\bar{\omega}\in S}\sum_{i\in\{1,2\}} \tilde{m}_i \mathrm{e}^{-\bar{q}_i\bar{s}+\bar{\omega}\bar{t}} + \text{c.c.}, \quad (3.31)$$

where S is the set of angular frequencies, such that Δ and $\bar{m}_{\Delta}$ satisfy the boundary conditions. The set S can be determined by substituting the above equations into the aforementioned boundary conditions. This procedure yields two equations determining the amplitudes for the shear:

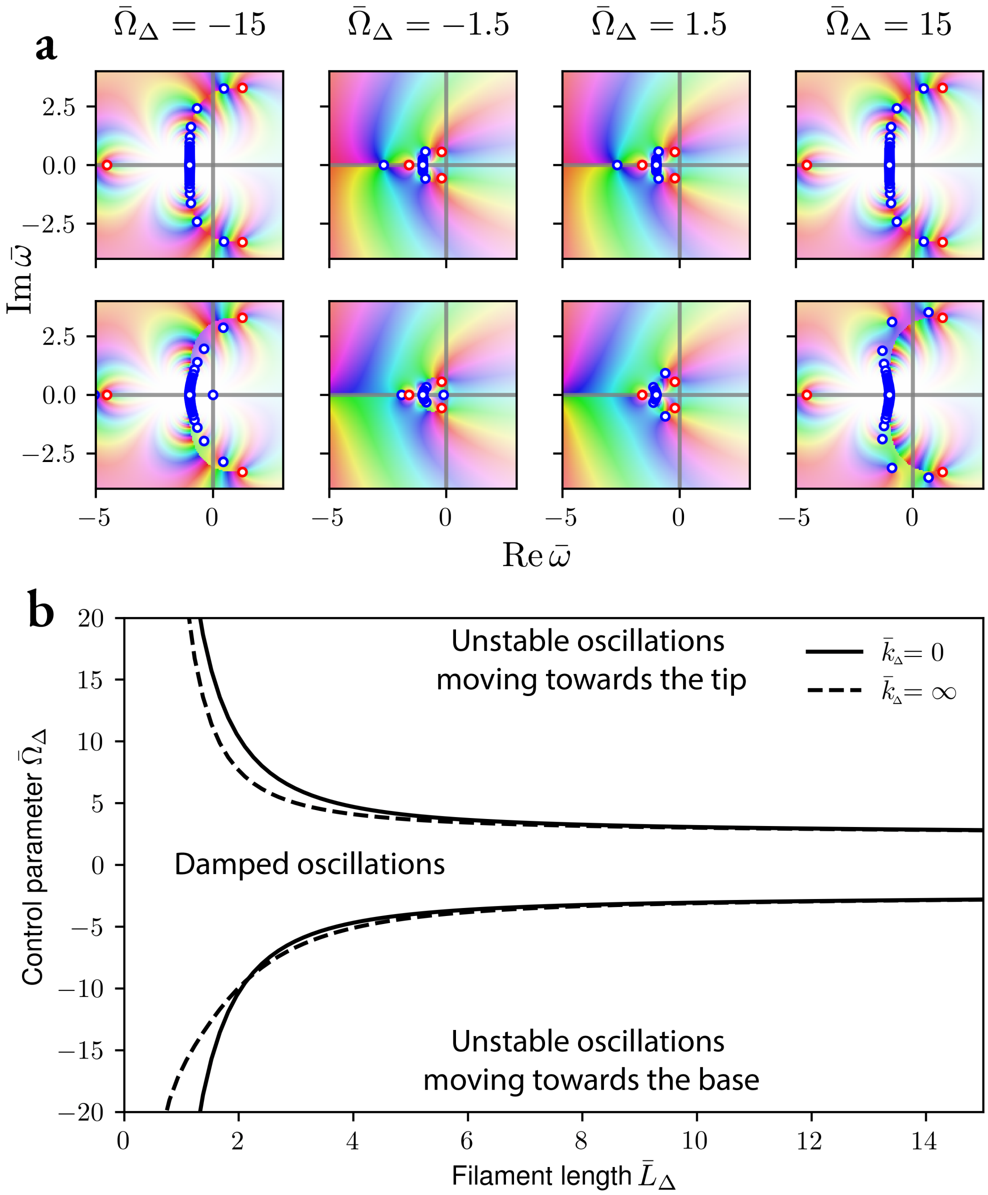

Figure 3.9: Stability of a finite length filament: (**a**) Plot of the $f(\bar{\omega}) = (\bar{q}_1/\bar{q}_2)(\bar{k}_\Delta + \bar{q}_2)/(\bar{k}_\Delta + \bar{q}_1) - \exp((\bar{q}_1 - \bar{q}_2)\,\bar{L}_\Delta)$ for $\bar{L}_\Delta = 2$, roots marked with blue bordered dots ○ are the allowed modes, roots marked with red bordered dots ○ are the (vanishing) trivial solution $q_1 = q_2$, the color hue and the brightness represents the phase and the amplitude of f and are for illustration purposes. First row corresponds to $\bar{k}_\Delta = 0$ and is symmetric for negative and positive values of Ω. Second row corresponds to $\bar{k}_\Delta \to \infty$. For $\left|\bar{\Omega}_\Delta\right| = 15$ two roots are unstable, for $\left|\bar{\Omega}_\Delta\right| = 1.5$ all roots are stable. (**b**) Critical value of the control parameter as a function of the length

$$\frac{\tilde{\Delta}_1}{\tilde{\Delta}_2} = -\frac{\bar{k}_\Delta + \bar{q}_2}{\bar{k}_\Delta + \bar{q}_1}, \tag{3.32}$$

$$\frac{\tilde{\Delta}_1}{\tilde{\Delta}_2} = -\frac{\bar{q}_2}{\bar{q}_1} \mathrm{e}^{(\bar{q}_1 - \bar{q}_2)\bar{L}_\Delta}. \tag{3.33}$$

Substituting the ratios of the amplitudes yields an equation whose solutions define the set S:

$$\frac{\bar{q}_1}{\bar{q}_2} \frac{\bar{k}_\Delta + \bar{q}_2}{\bar{k}_\Delta + \bar{q}_1} - \mathrm{e}^{(\bar{q}_1 - \bar{q}_2)\bar{L}_\Delta} = 0. \tag{3.34}$$

The equation has the trivial solution $\bar{q}_1 = \bar{q}_2 = \bar{q}$, however these modes vanish identically. This can be easily checked by substituting $\Delta(\bar{s}, \bar{t}) = (\tilde{\Delta}_1 + \tilde{\Delta}_2) \exp(-\bar{q}\bar{s} + \bar{\omega}\bar{t})$ in one of the boundary conditions. For an arbitrary $\bar{k}_\Delta$, the relation 3.34 does not admit closed form non-trivial solutions, and must instead be solved numerically. The system admits an oscillatory instability, if one can go through a situation in which all angular frequencies allowed by the boundary conditions have a negative real part, to one in which at least one pair of angular frequencies have a vanishing real part, by varying the control parameter $\bar{\Omega}_\Delta$. The distribution of angular frequencies in the complex plane can be visualised in figure 3.9, were we can see that there indeed exists an oscillatory instability.

The amplitudes for the active moment can be derived by substituting equations (3.30,3.31) in the active moment equation (3.24) at the boundaries, thus yielding:

$$\frac{\tilde{m}_1}{\tilde{m}_2} = -\mathrm{e}^{(\bar{q}_1 - \bar{q}_2)\bar{L}_\Delta} \tag{3.35}$$

$$\frac{\tilde{m}_1}{\tilde{\Delta}_1} = \frac{\bar{k}_\Delta \bar{\Omega}_\Delta}{1 + \bar{\omega}} \frac{1 - \frac{\bar{q}_1}{\bar{q}_2} \mathrm{e}^{-(\bar{q}_1 - \bar{q}_2)\bar{L}_\Delta}}{1 - \mathrm{e}^{-(\bar{q}_1 - \bar{q}_2)\bar{L}_\Delta}}. \tag{3.36}$$

The above is enough to fully characterise the dynamics of the shear, and the active moment, at the onset of the instability.

Existence of a slow mode

Figure 3.9 shows that, in some cases, there is a mode near the origin of the complex plane. This mode is called a slow mode, and describes slow relaxation dynamics. Subtracting the equations of motion (3.23,3.24), for $\bar{\kappa}_\Delta = 0$ we obtain the following conservation equation:

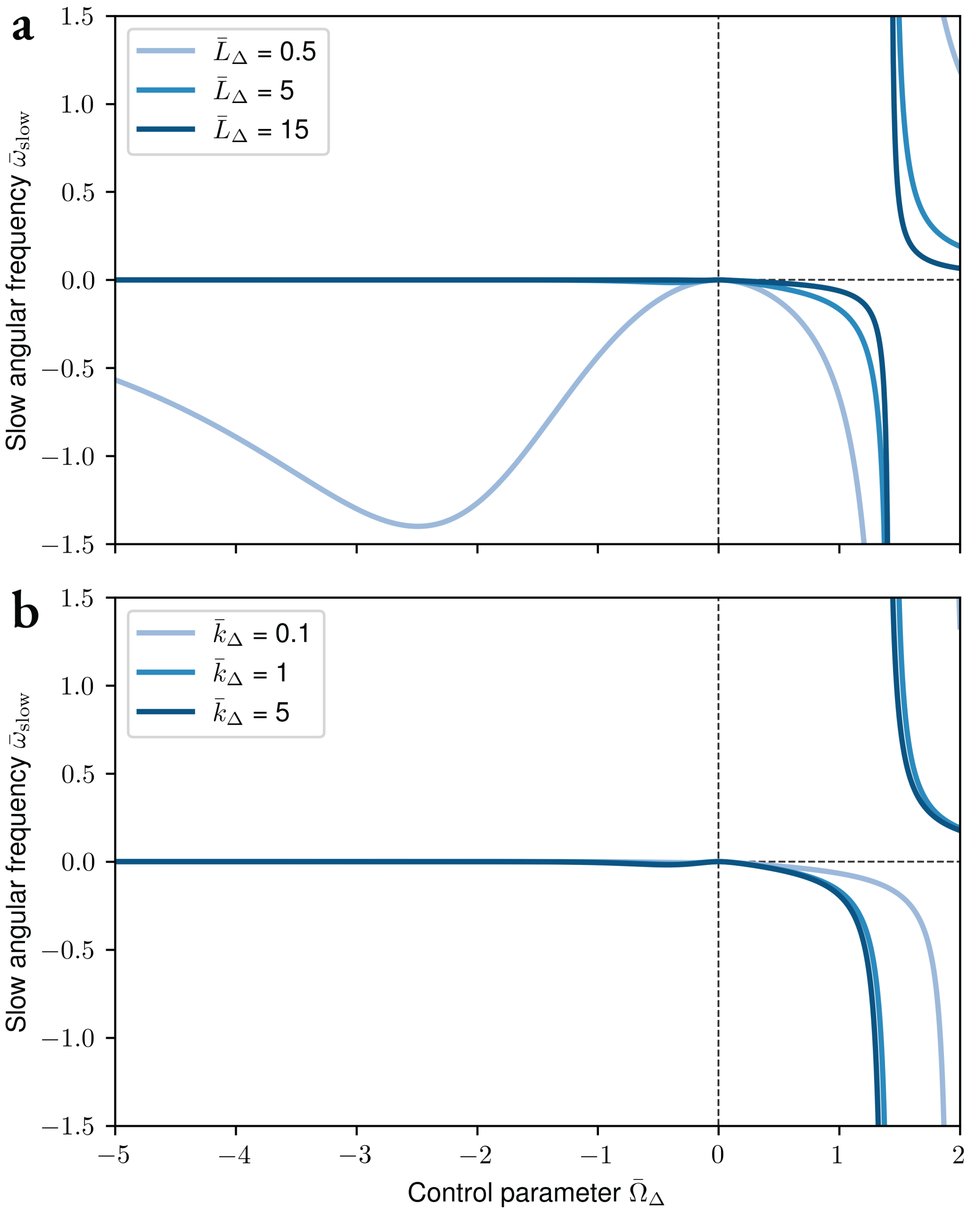

Figure 3.10: Slow mode expansion $\bar{\omega}_{\mathrm{slow}}$, as a function of the control parameter $\bar{\Omega}_\Delta$: (**a**) varying the length of the filament, (**b**) varying the basal shear rigidity of the filament.

$$\partial_t\left(\Delta - \bar{\Omega}_\Delta \bar{m}_\Delta\right) = -\partial_s(\bar{\Omega}_\Delta \Delta - \partial_s \Delta), \tag{3.37}$$

where $\Delta - \bar{\Omega}_\Delta \bar{m}_\Delta$ is the slow mode. If the left-hand side vanishes, then the general solution of the equation is:

$$\Delta(\bar{s}, \bar{t}) = \Delta_1(\bar{t}) \frac{\mathrm{e}^{\bar{\Omega}_\Delta \bar{s}}}{\bar{\Omega}_\Delta} + \Delta_2(\bar{t}) \tag{3.38}$$

$$\bar{m}_\Delta(\bar{s}, \bar{t}) = \frac{\Delta(\bar{s}, \bar{t})}{\bar{\Omega}_\Delta}. \tag{3.39}$$

It is easy to check that with the boundary conditions, the solutions of these equations vanish identically. However, such equations often display long transients, characterised by a dispersion relation such that the angular frequency is proportional to the wavenumber $\bar{\omega} \sim \bar{q}$ as $\bar{\omega}$ becomes small. Expanding $\bar{\omega}_\pm$ in (3.28) for small values of $\bar{q}$, the angular frequency reads:

$$\bar{\omega}_\pm = \frac{1}{2}\left(-\bar{\kappa}_\Delta - 1 + |\bar{\kappa}_\Delta - 1|\right) \pm \frac{\mathrm{i}\bar{\Omega}_\Delta \bar{q}}{|\bar{\kappa}_\Delta - 1|} + \mathcal{O}(\bar{q}^2). \tag{3.40}$$

The angular frequency $\bar{\omega}_\pm$ is proportional to $\bar{q}$ only if the shear rigidity vanishes. Let $\bar{\omega}_{\text{slow}}$ be the slow mode, describing a long transient in the dynamics of the active filament. In the case $\bar{\kappa}_\Delta = 0$, by expanding equation (3.34) multiplied by $\bar{q}_2 \bar{k}_\Delta + \bar{q}_1 \bar{q}_2$, we find an expression for the slow mode:

$$\bar{\omega}_{\text{slow}} = \begin{cases} \dfrac{\bar{k}_\Delta \bar{\Omega}_\Delta^2 \mathrm{e}^{\bar{\Omega}_\Delta \bar{L}_\Delta}}{\bar{\Omega}_\Delta - \bar{k}_\Delta + \mathrm{e}^{\bar{\Omega}_\Delta \bar{L}_\Delta}\left(\left(\bar{k}_\Delta\left(\bar{\Omega}_\Delta^2 - 1\right) - \bar{\Omega}_\Delta\right) + \delta\right)} & \bar{\Omega}_\Delta > 0, \\ 0 & \bar{\Omega}_\Delta = 0, \\ \dfrac{\bar{k}_\Delta \bar{\Omega}_\Delta^2 \mathrm{e}^{\bar{\Omega}_\Delta \bar{L}_\Delta}}{\bar{\Omega}_\Delta - \bar{k}_\Delta + \mathrm{e}^{\bar{\Omega}_\Delta \bar{L}_\Delta}\left(\bar{k}_\Delta\left(\bar{\Omega}_\Delta^2 - 1\right) - \bar{\Omega}_\Delta\right)} & \bar{\Omega}_\Delta < 0, \end{cases} \tag{3.41}$$

where $\delta = \bar{L}_\Delta \bar{\Omega}_\Delta \bar{k}_\Delta (\bar{\Omega}_\Delta^2 - 2)$. The expansion is valid as long as $\bar{\omega}_{\text{slow}}$ is small. For $\bar{\Omega}_\Delta > 0$, this is only the case when $\bar{\Omega}_\Delta \ll 1$ therefore in this case a slow mode is never concurrent with stable oscillations. For $\bar{\Omega}_\Delta < 0$, this is the case if the denominator is not small, and always valid if $\left|\bar{\Omega}_\Delta\right| \gg \bar{L}_\Delta$, therefore in this case, a slow mode can be concurrent with stable oscillations, and we may observe oscillations biased to one side over the other. The dependence of $\bar{\omega}_{\text{slow}}$ as a function of the parameters can be seen in figure 3.10

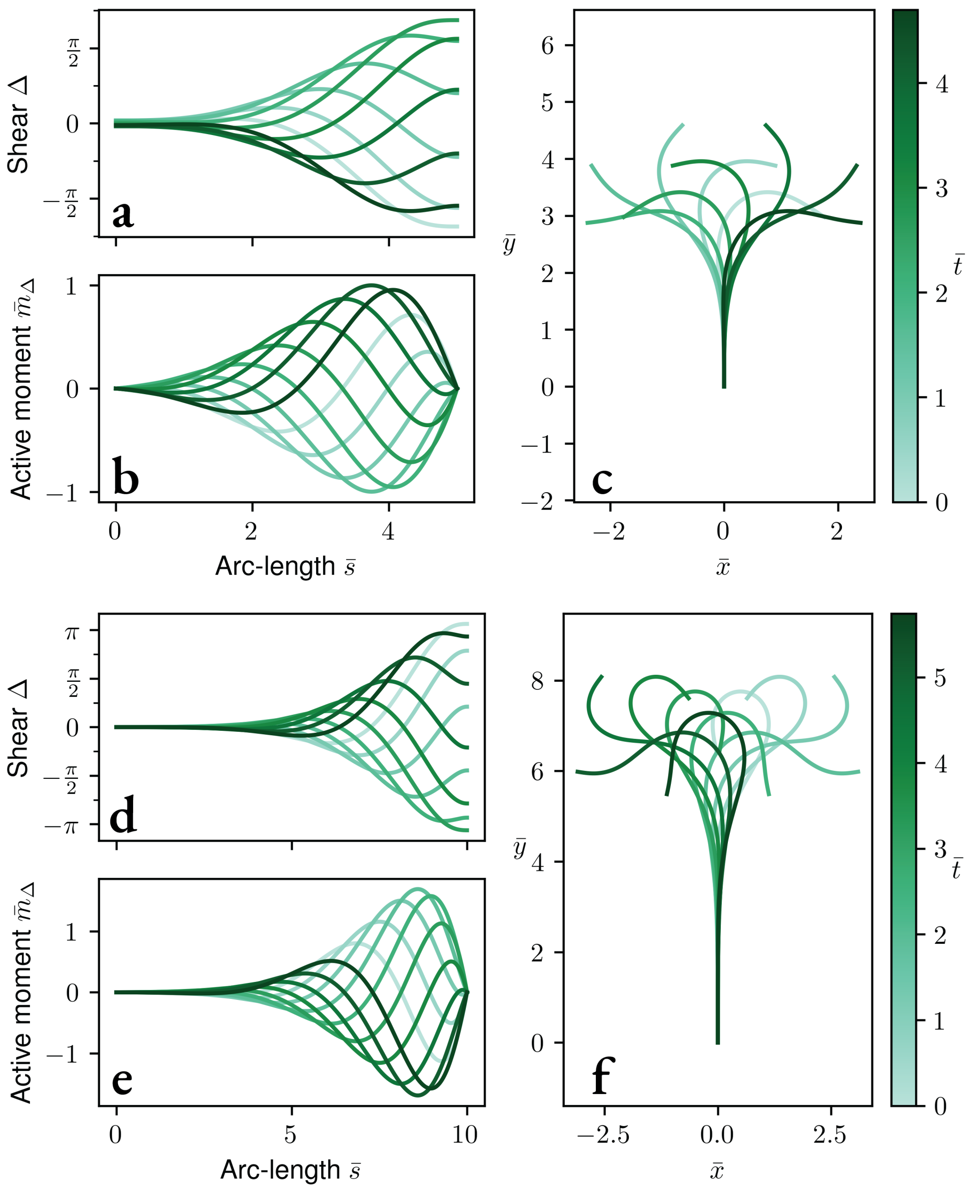

Figure 3.11: Analytical solutions of the waveforms and filament conformation, for $\bar{\kappa}_\Delta = 0$ at the instability: First for a filament of length $\bar{L}_\Delta = 5$ and $\bar{\Omega}_\Delta \simeq 3.9$ (**a**) shear, (**b**) active moment, (**c**) filament shape. Second for a filament of length $\bar{L}_\Delta = 10$ and $\bar{\Omega}_\Delta \simeq 3.1$ (**d**) shear, (**e**) active moment, (**f**) filament shape

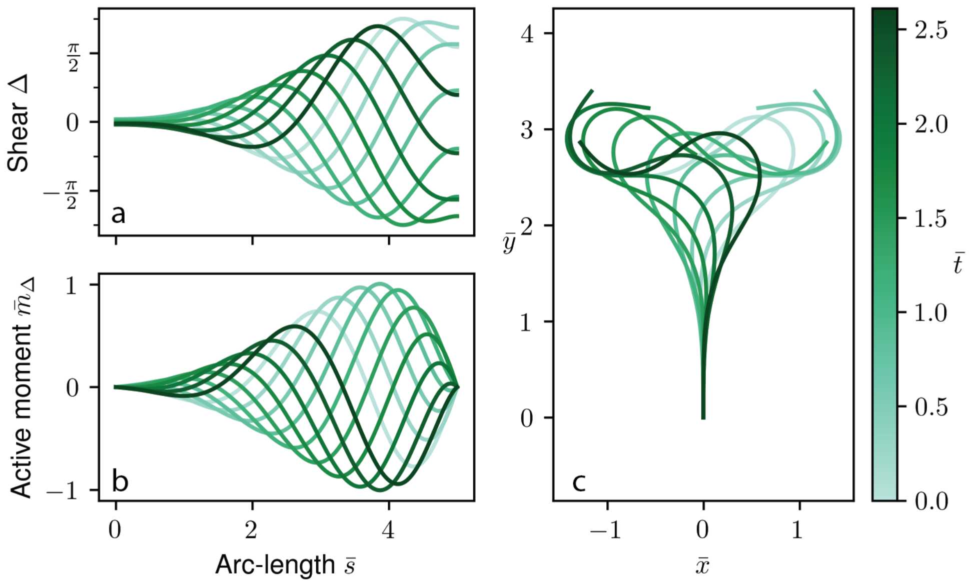

Figure 3.12: Analytical solutions of the waveforms and filament conformation of a filament of length $\bar{L}_\Delta = 5$ and $\bar{\kappa}_\Delta = 2$ at the instability $\bar{\Omega}_\Delta \simeq 9.6$ with (**a**) shear, (**b**) active moment, (**c**) filament shape

3.4.2 FILAMENT WITHOUT BASAL SHEAR RIGIDITY: ANALYTICAL RESULTS

In the limit of a filament with no basal shear rigidity, $\bar{k}_\Delta = 0$, Equation (3.34), which selects the modes, is a simple algebraic equation, in which the wavenumbers $\bar{q}_1$ and $\bar{q}_2$ are related to each-other by the phase difference:

$$\bar{q}_1 - \bar{q}_2 = \frac{2i\pi n}{\bar{L}_\Delta}, \tag{3.42}$$

with the integer n numbering triplets of modes. The case $n = 0$ corresponds to the trivial, vanishing, solution. Substituting the wavenumbers $\bar{q}_{1,2}$ by their expression given in equation (3.29), we find the following family of third degree polynomials, whose solutions are the allowed angular frequencies:

$$\left(\frac{\pi^2 n^2}{\bar{L}_\Delta^2} + \bar{\kappa}_\Delta + \bar{\omega}\right)(1+\bar{\omega})^2 + \frac{\bar{\Omega}_\Delta^2}{4} = 0. \tag{3.43}$$

The solutions of the above polynomials are plotted in figure 3.9. Because the coefficients of the polynomial are real, if one solution is complex, then another one is its complex conjugate, and the third one is a real number. Therefore, the onset of the instability can be found by looking for pairs of solutions $\{\bar{\Omega}_\Delta = \bar{\Omega}_n, \bar{\omega} = \pm \mathrm{i}\bar{\omega}_n\}$. These solutions are:

$$\bar{\Omega}_n = \pm 2\sqrt{2}\left(\frac{\pi^2 n^2}{\bar{L}_\Delta^2} + \bar{\kappa}_\Delta + 1\right), \tag{3.44}$$

$$\bar{\omega}_n = \pm\sqrt{2\frac{\pi^2 n^2}{\bar{L}_\Delta^2} + 2\bar{\kappa}_\Delta + 1}. \tag{3.45}$$

As the integer increases, $\left|\bar{\Omega}_n\right|$ also increases, therefore the system becomes unstable when $\left|\bar{\Omega}_\Delta\right| \geq |\bar{\omega}_1|$. For $\bar{\Omega}_\Delta = \bar{\Omega}_1$, the complex wavenumbers can then be written in the following form:

$$q_{1,2}(\bar{\omega}_1) = -\mathrm{sgn}\left(\bar{\Omega}_1\right)\frac{\sqrt{2}}{2}(1 - \mathrm{i}\bar{\omega}_1) \pm \mathrm{i}\frac{\pi}{\bar{L}_\Delta}, \tag{3.46}$$

where $\mathrm{sgn}\left(\bar{\Omega}_1\right) = \bar{\Omega}_1 / \left|\bar{\Omega}_1\right| \in \{-1, +1\}$ is the sign of the variable $\bar{\Omega}_1$. With the above wavevectors and angular frequencies, and using equations (3.32,3.33,3.35,3.36), the exact dynamics of Δ and $\bar{m}_\Delta$ at the instability are determined:

$$\begin{aligned}\Delta(\bar{s},\bar{t}) = A\mathrm{e}^{\mathrm{sgn}\left(\bar{\Omega}_1\right)\frac{\sqrt{2}}{2}\bar{s}}\Bigg[a(\bar{s})\sin\left(\bar{\omega}_1\left(\bar{t} - \mathrm{sgn}\left(\bar{\Omega}_\Delta\right)\frac{\sqrt{2}}{2}\bar{s}\right) + \theta\right)\\ +b(\bar{s})\cos\left(\bar{\omega}_1\left(\bar{t} - \mathrm{sgn}\left(\bar{\Omega}_\Delta\right)\frac{\sqrt{2}}{2}\bar{s}\right) + \theta\right)\Bigg].\end{aligned} \tag{3.47}$$

The variable amplitudes $a(\bar{s})$ and $b(\bar{s})$ read:

$$a(\bar{s}) = -\mathrm{sgn}\left(\bar{\Omega}_1\right)\frac{\sqrt{2}}{2}\sin\left(\frac{\pi\bar{s}}{\bar{L}_\Delta}\right) + \frac{\pi}{\bar{L}_\Delta}\cos\left(\frac{\pi\bar{s}}{\bar{L}_\Delta}\right),$$

$$b(\bar{s}) = +\mathrm{sgn}\left(\bar{\Omega}_1\right)\frac{\sqrt{2}}{2}\bar{\omega}_1\sin\left(\frac{\pi\bar{s}}{\bar{L}_\Delta}\right).$$

The active moments have the form:

$$\bar{m}_\Delta(\bar{s},\bar{t}) = B\mathrm{e}^{\mathrm{sgn}\left(\bar{\Omega}_1\right)\frac{\sqrt{2}}{2}\bar{s}}\sin\left(\frac{\pi\bar{s}}{\bar{L}_\Delta}\right)\sin\left(\bar{\omega}_1\left(\bar{t} - \mathrm{sgn}\left(\bar{\Omega}_1\right)\frac{\sqrt{2}}{2}\bar{s}\right) + \varphi\right). \tag{3.48}$$

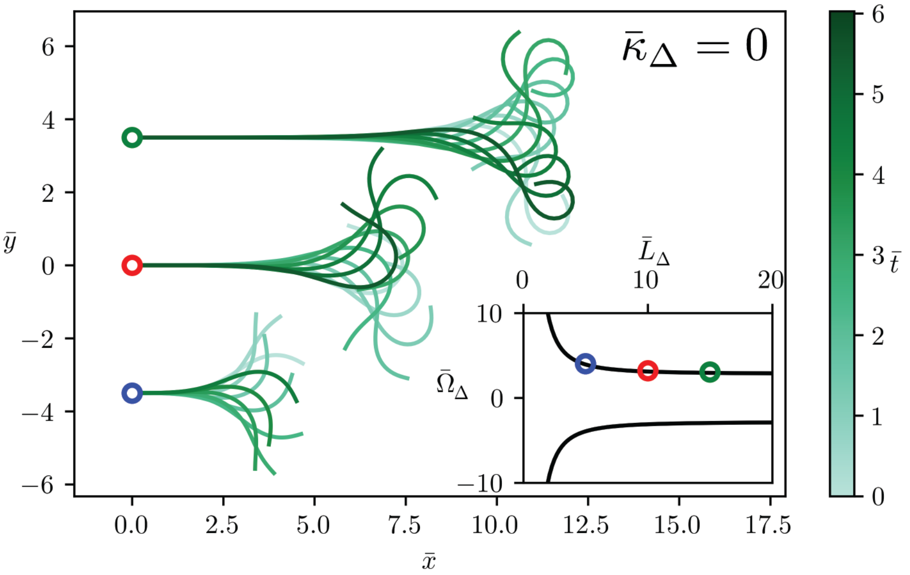

Figure 3.13: Beating patterns of a filament of different lengths. The upper, longer filament, marked with a green dot ○, is of length $\bar{L}_\Delta = 15$, $\bar{\Omega}_\Delta \simeq 3$ and $\epsilon = 0.08$. The middle filament, marked with a red dot ○, is of length $\bar{L}_\Delta = 10$, $\bar{\Omega}_\Delta \simeq 3.1$ and $\epsilon = 0.1$. The lowermost filament, marked with a blue dot ○, is of length $\bar{L}_\Delta = 5$, $\bar{\Omega}_\Delta \simeq 3.9$ and $\epsilon = 0.15$. Their positions in the phase space are marked with their respective coloured dots in the lower right quadrant. Here $\bar{x} = x/\mu_\Delta$ and $\bar{y} = y/\mu_\Delta$, are the dimensionless units of the euclidean plane.

The amplitudes $A = |\tilde{\Delta}_1/q_2|/4$ and $B = 4\,|\tilde{m}_1|$ are determined by the nonlinearities, and the phases θ and ϕ are determined by the initial conditions. The phase velocity of a travelling wave is given by $v = \lambda/T$, where $\lambda = \operatorname{sgn}\left(\bar{\Omega}_1\right) 2\pi\sqrt{2}/\bar{\omega}_1$ is the wavelength, and $T = 2\pi/\bar{\omega}_1$ is the period. Therefore the wave velocity of the shear and the active moment is:

$$v = \operatorname{sgn}\left(\bar{\Omega}_1\right)\sqrt{2}. \tag{3.49}$$

The phase velocity is constant and independent from all other parameters, such as the length of the filament, the shear rigidity, and its sign is determined by the sign of the control parameter.

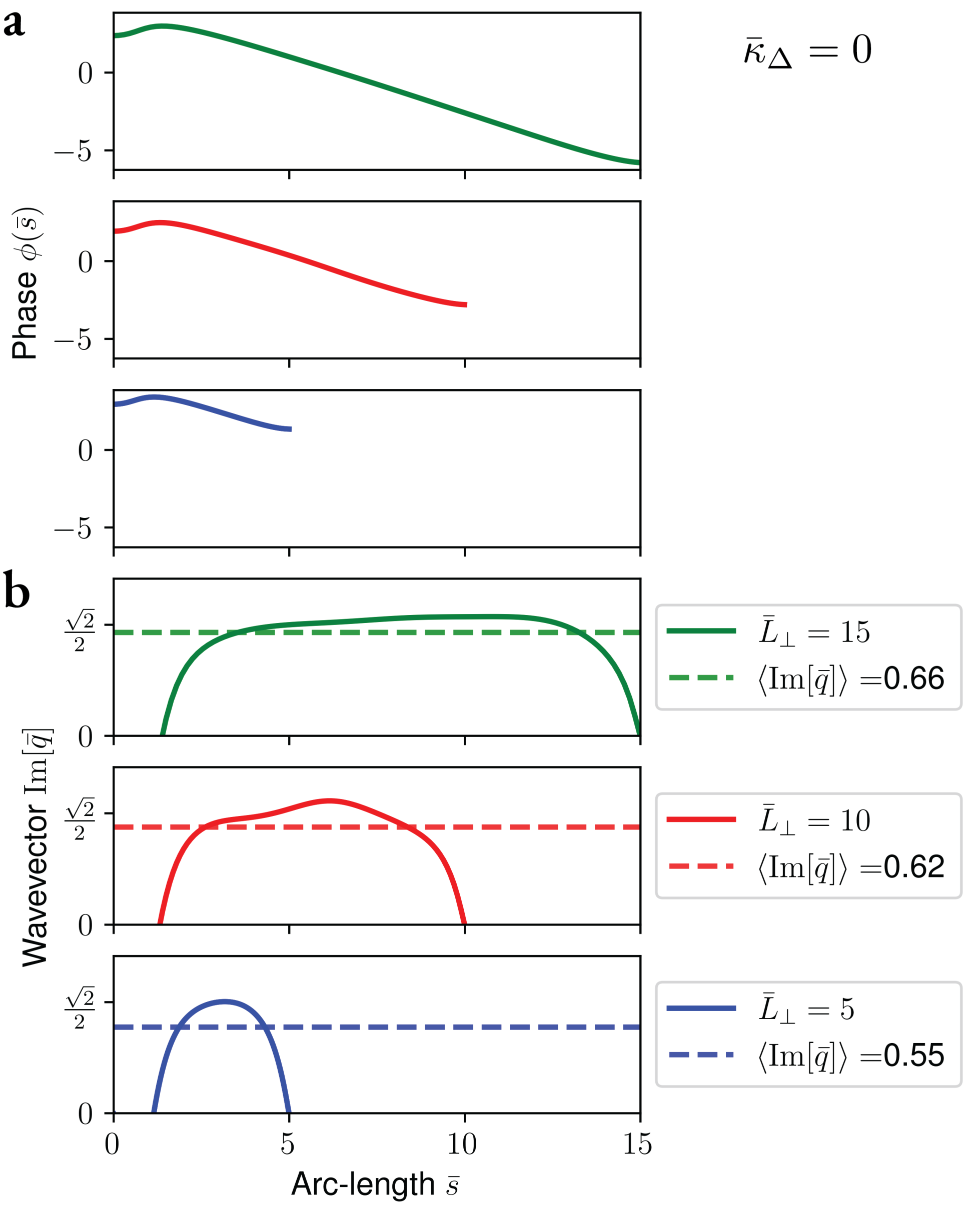

Figure 3.14: Properties of tangent angle waves $\psi(\bar{s}, \bar{t}\,)$ in the limit of dominant shear friction on filaments of length $\bar{L}_\perp \in \{5, 10, 15\}$, for $\bar{\kappa}_\Delta = 0$, shown in green, red and blue, respectively: (**a**) phase, (**b**) wave vector, as defined in section 3.2. The brackets $\langle \cdot \rangle$ are averages over the filament length.

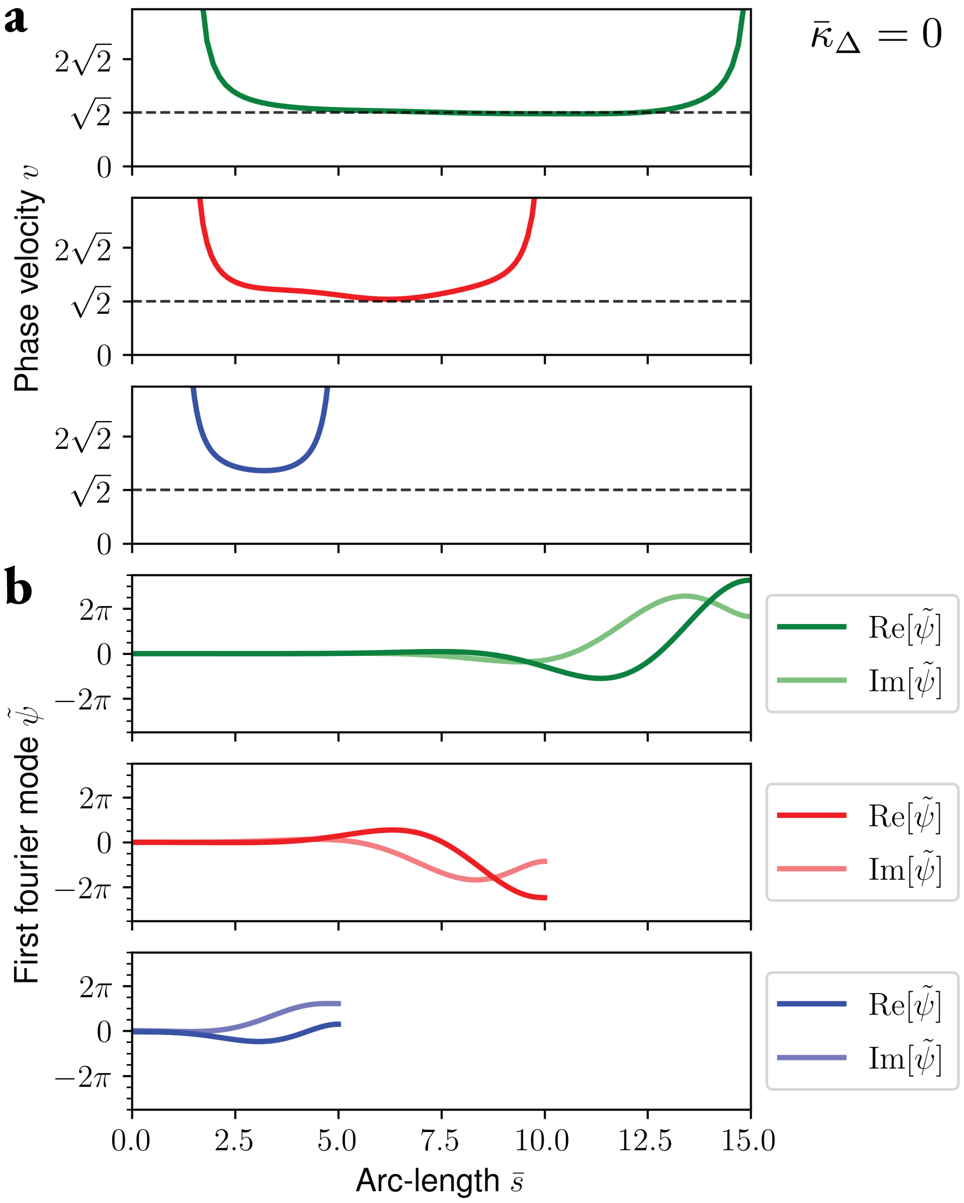

Figure 3.15: Properties of tangent angle waves $\psi(\bar{s}, \bar{t})$ in the limit of dominant external friction on filaments of length $\bar{L}_\perp \in \{5, 10, 15\}$, for $\bar{\kappa}_\Delta = 0$, shown in green, red and blue, respectively: (**a**) phase velocity, (**b**) first Fourier mode representation, as defined in section3.2.

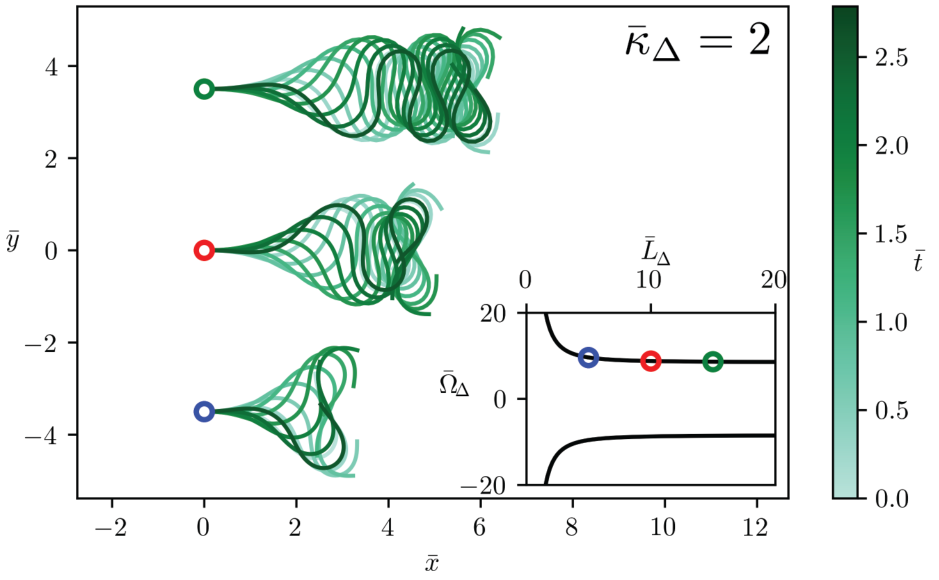

Figure 3.16: Beating patterns of a filament of different lengths and internal shear rigidity $\bar{\kappa}_\Delta = 2$. The upper, longer filament, marked with a green dot ○, is of length $\bar{L}_\Delta = 15$, $\bar{\Omega}_\Delta \simeq 8.6$ and $\epsilon = 2$. The middle filament, marked with a red dot ○, is of length $\bar{L}_\Delta = 10$, $\bar{\Omega}_\Delta \simeq 8.7$ and $\epsilon = 2$. The lowermost filament, marked with a blue dot ○, is of length $\bar{L}_\Delta = 5$, $\bar{\Omega}_\Delta \simeq 9.6$ and $\epsilon = 2$.

3.4.3 NUMERICAL SOLUTIONS

We show numerical solutions for the equations of motion, computed using a modified Crank-Nicolson finite difference scheme [126], with a time step of $\delta\bar{t} = 0.06$ and a spatial step-size of $\delta\bar{s} = \bar{L}_\Delta/101$. As in section 3.3.2, a cubic nonlinearity is added to the dynamical equation of the active moment, in order to stabilise the numerical solutions, so that we have:

$$\partial_{\bar{t}}\bar{m}_\Delta = \partial_{\bar{s}}\psi - \bar{m}_\Delta - \epsilon\bar{m}_\Delta^3. \tag{3.50}$$

We do not present a systematic review of the configuration space, but only showcase some particular examples at the onset of the instability. We do not explore the nonlinear regime in this section. For an active filament at the onset of the instability, the basal shear rigidity has very little effect on the dynamics, therefore, for the sake of simplicity, we only show active filaments such that $\bar{k}_\Delta = 0$.

The beating patterns made by filaments with no internal shear rigidity, $\bar{\kappa}_\Delta = 0$, are shown in figure 3.13 for filaments of length $\bar{L}_\Delta \in \{5, 10, 15\}$. We observe that

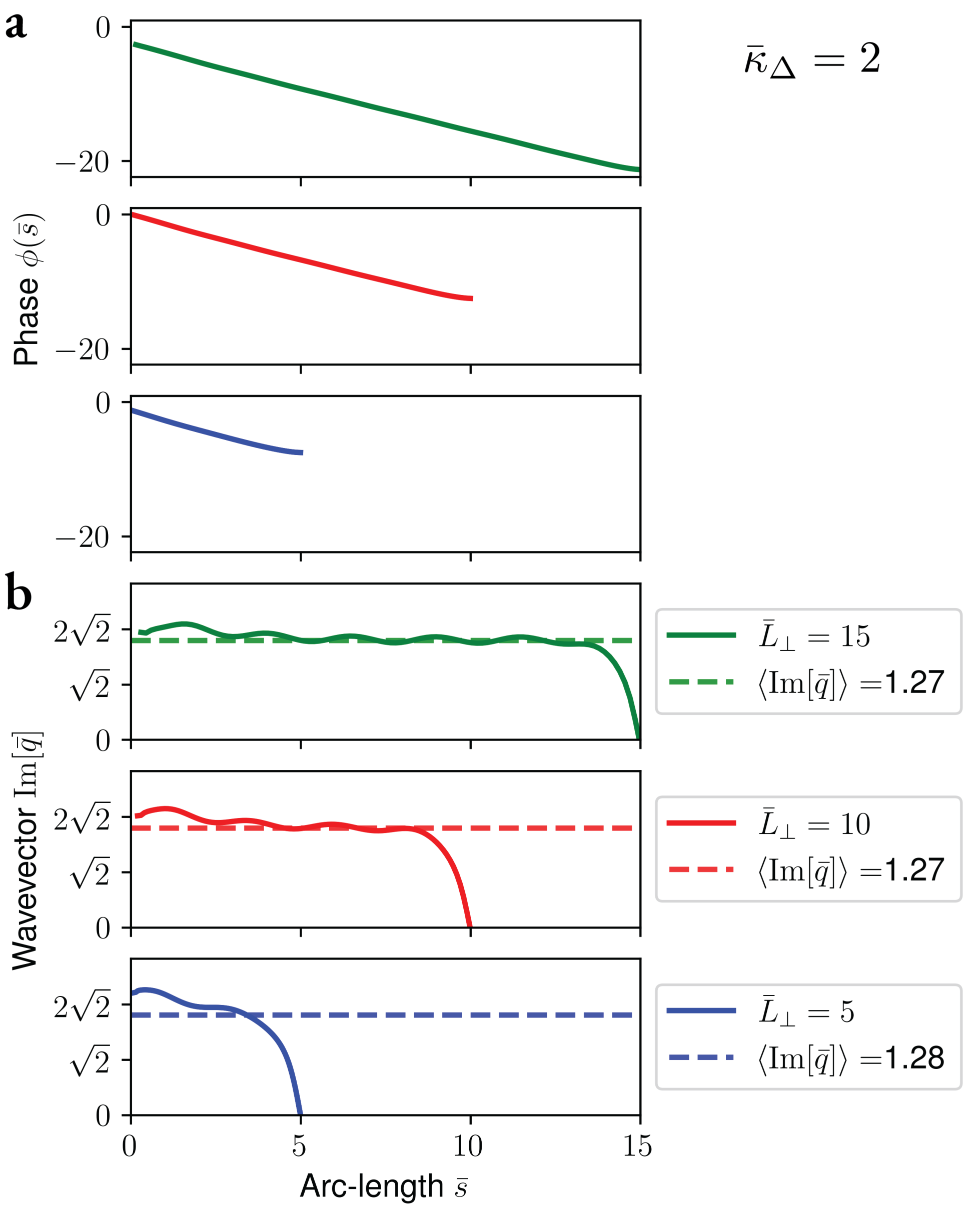

Figure 3.17: Properties of tangent angle waves $\psi(\bar{s}, \bar{t}\,)$ in the limit of dominant shear friction on filaments of length $\bar{L}_\perp \in \{5, 10, 15\}$, for $\bar{\kappa}_\Delta = 2$, shown in green, red and blue, respectively: (**a**) phase, (**b**) wave vector, as defined in section 3.2. The brackets $\langle \cdot \rangle$ are averages over the filament length.

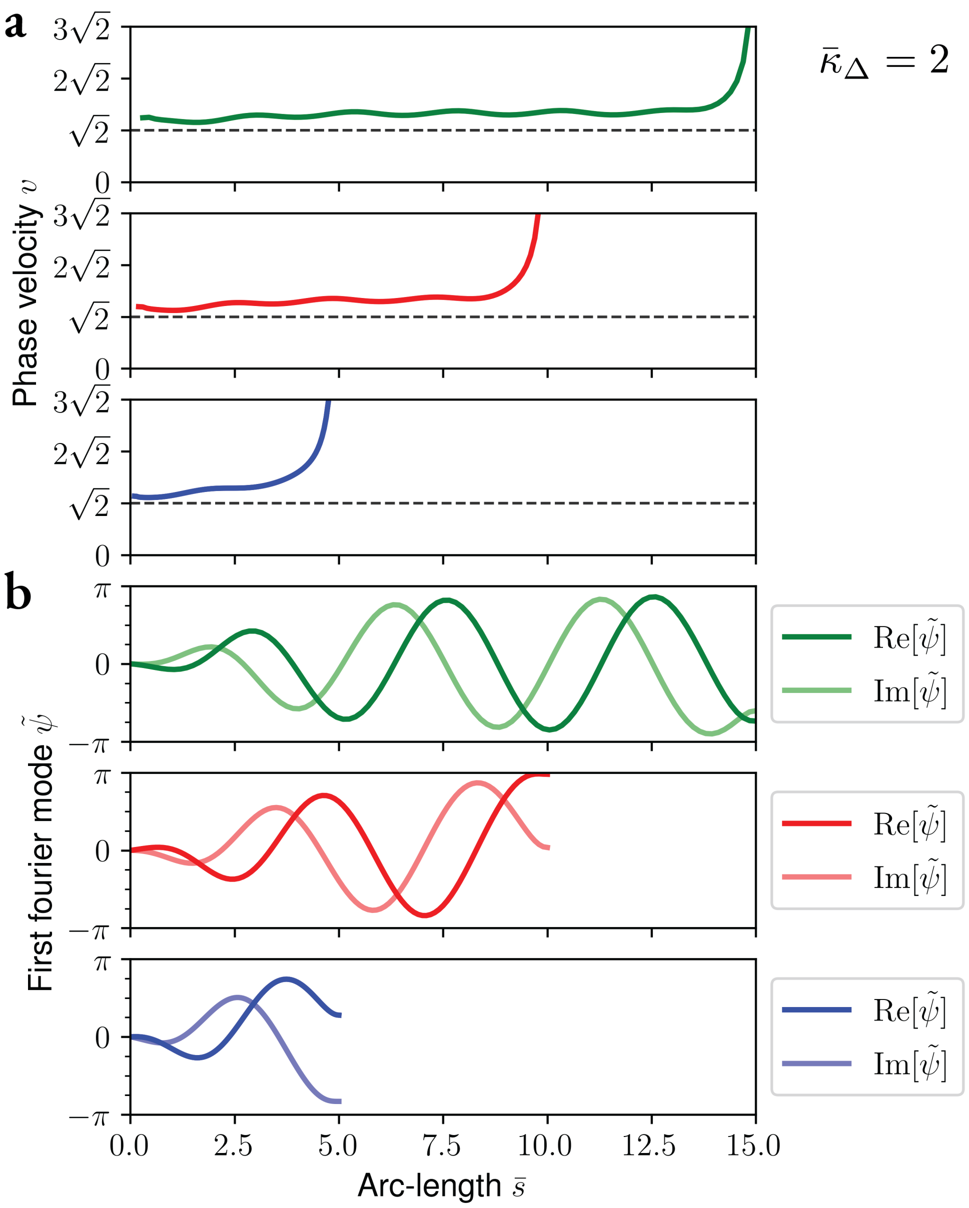

Figure 3.18: Properties of tangent angle waves $\psi(\bar{s}, \bar{t})$ in the limit of dominant external friction on filaments of length $\bar{L}_\perp \in \{5, 10, 15\}$, for $\bar{\kappa}_\Delta = 2$, shown in green, red and blue, respectively: (**a**) phase velocity, (**b**) first Fourier mode representation, as defined in section3.2.

the superposition of their conformations in time forms trumpet-like shapes. Figure 3.16 shows some of the properties of their beating. Because $\bar{k}_\Delta = 0$, we know that the phase velocity of travelling shear waves along the filament is $v = \sqrt{2}$. The numerical solutions are in agreement, with nearly constant phase velocity in the centre of the filament, and deviations at the boundaries. As the analytical solution predicts, the beating has only a single Fourier mode.

Increasing the internal shear rigidity to $\bar{\kappa}_\Delta = 2$, we see in figure 3.16 that the shape of the filament changes, and becomes more tubular. The analytical calculation predicts that the phase velocity does no change from the previous case. This is indeed the case, with a constant phase velocity $v \simeq \sqrt{2}$ at the centre, with a deviation at the boundary.

3.5 LIMIT OF DOMINANT CURVATURE FRICTION

The final limit we consider in this chapter is the case of dominant curvature friction. This limit is reached when $q^2\xi_\Delta/\xi_\perp \gg 1$ and $q^2\xi_C/\xi_\Delta \gg 1$, or more concisely, when $q^4\xi_C/\xi_\perp \gg 1$. The equations of motion are, in dimensionless form:

$$\partial_{\bar{t}}\partial_{\bar{s}}^2\Delta = \Delta - \bar{\kappa}_C\partial_{\bar{s}}^2\Delta + \bar{\Omega}_C\bar{m}_C \tag{3.51}$$

$$\partial_{\bar{t}}\bar{m}_C = \partial_{\bar{s}}\Delta - \bar{m}_C. \tag{3.52}$$

With the dynamic boundary conditions:

$$\partial_{\bar{s}}\partial_{\bar{t}}\Delta(0,\bar{t}) + \bar{\kappa}_C\partial_{\bar{s}}\Delta(0,\bar{t}) = \bar{k}_C\Delta(0,\bar{t}), \tag{3.53}$$

$$\partial_{\bar{s}}\partial_{\bar{t}}\Delta(\bar{L}_C,\bar{t}) + \bar{\kappa}_C\partial_{\bar{s}}\Delta(\bar{L}_C,\bar{t}) = 0. \tag{3.54}$$

The arc-length is here rescaled by $\mu_C = \sqrt{\xi_C k_\mathrm{d}/\kappa_\Delta}$ and the time is rescaled by $1/k_\mathrm{d}$. The dimensionless parameters are given as functions of the dimensional parameters in table 3.c.

Using the same Laplace ansatz as in the previous section, with $\Delta = \tilde{\Delta}\exp(-\bar{q}\bar{s}+\bar{\omega}\bar{t})$ and $\bar{m}_C = \tilde{m}_C\exp(-\bar{q}\bar{s}+\bar{\omega}\bar{t})$, we find the dispersion relation for the case of dominant curvature friction:

$$\left(\bar{\kappa}_C + \bar{\omega}\right)\bar{q}^2 + \frac{\bar{\Omega}_C}{1+\bar{\omega}}\bar{q} - 1 = 0. \tag{3.55}$$

The complex angular frequencies $\bar{\omega}_\pm$ solution fo the dispersion relation are:

Dimensionless time	$\bar{t} = k_{\mathrm{d}} t$
Dimensionless arc-length	$\bar{s} = \dfrac{s}{\mu_C}$
Dimensionless shear rigidity	$\bar{\kappa}_C = \dfrac{\kappa_C}{\kappa_\Delta} \mu_C^2$
Control parameter	$\bar{\Omega}_C = \dfrac{k_{\mathrm{a}}}{k_{\mathrm{d}}} \dfrac{\mu_C}{\kappa_\Delta}$
Dimensionless active moment	$\bar{m}_C = \dfrac{k_{\mathrm{d}}}{k_{\mathrm{a}} \mu_C} m_{\mathrm{a}}$
Dimensionless filament length	$\bar{L}_C = \frac{L}{\mu_C}$
Dimensionless basal shear rigidity	$\bar{k}_C = \frac{k_\Delta \mu_C}{\xi_C k_{\mathrm{d}}}$

Table 3.c: Dimensionless parameters in the limit of dominant external friction

$$\bar{\omega}_\pm = \frac{1 - \bar{q}^2 \left(1 + \bar{\kappa}_C\right)}{2\bar{q}^2} \pm \frac{1}{2\bar{q}^2} \sqrt{\left(1 + \bar{q}^2 \left(1 - \bar{\kappa}_C\right)\right)^2 - 4\bar{q}^3 \bar{\Omega}_C}. \tag{3.56}$$

An infinite filament is unstable if there exists a real part of the complex angular frequency as a function of purely imaginary $\bar{q} \in \mathrm{i}\mathbb{R}$. For $\bar{\kappa}_C = 0$, the onset of the instability occurs for $\bar{\Omega}_C = 1$, in which the most unstable mode is for $\bar{q} \to \infty$, as can be seen in figure 3.20. Finite values of the rigidity $\bar{\kappa}_C$ suppress this ultraviolet divergence.

Unlike the previous cases, a filament of finite length in the case of dominant curvature friction has dynamic boundary conditions, which depend on the time derivatives of the curvature. This makes the numerical solutions more complex, and are beyond the scope of the dissertation. However some analytical calculations can be obtained. The complex wavenumbers $\bar{q}$, solutions of the dispersion relation, are:

$$\bar{q}_{1,2} = -\frac{1}{2} \frac{\bar{\Omega}_C}{(1 + \bar{\omega})(\bar{\kappa}_C + \bar{\omega})} \pm \frac{1}{2} \sqrt{\frac{\bar{\Omega}_C^2}{(1 + \bar{\omega})^2 (\bar{\kappa}_C + \bar{\omega})^2} + \frac{4}{\bar{\kappa}_C + \bar{\omega}}}. \tag{3.57}$$

The complex angular frequencies $\bar{\omega}$ aresolutions of the following transcendental equation:

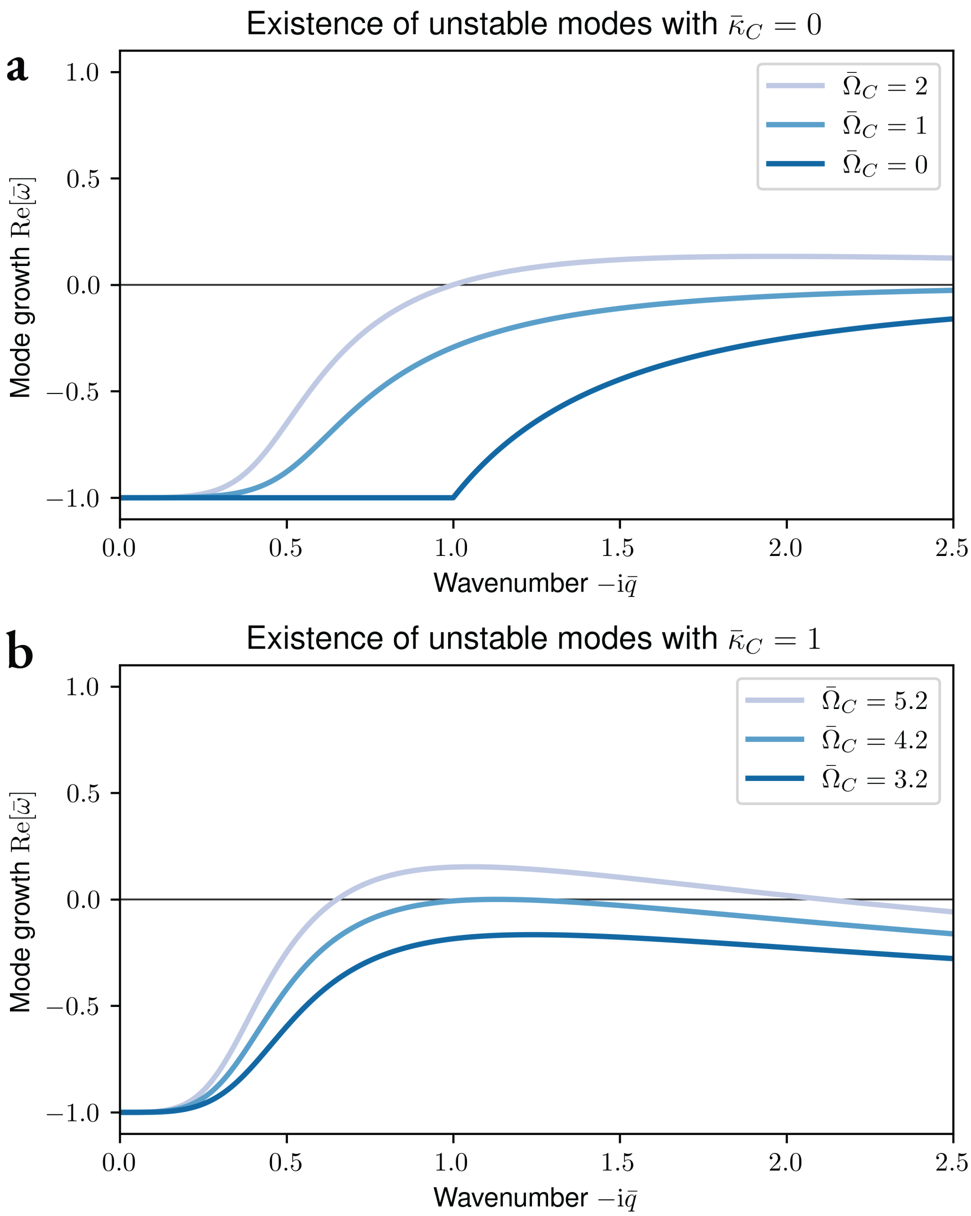

Figure 3.19: Stability of an infinitely long filament: (**a**) Mode growth as a function of the wavenumber for different values of the control parameter and at $\bar{\kappa}_C = 0$ (**b**) Mode growth as a function of the wavenumber for different values of the control parameter and at $\bar{\kappa}_C = 1$. Wavevector corresponding to the maximum of $\mathrm{Re}[\bar{\omega}]$ is $\bar{q}_*$

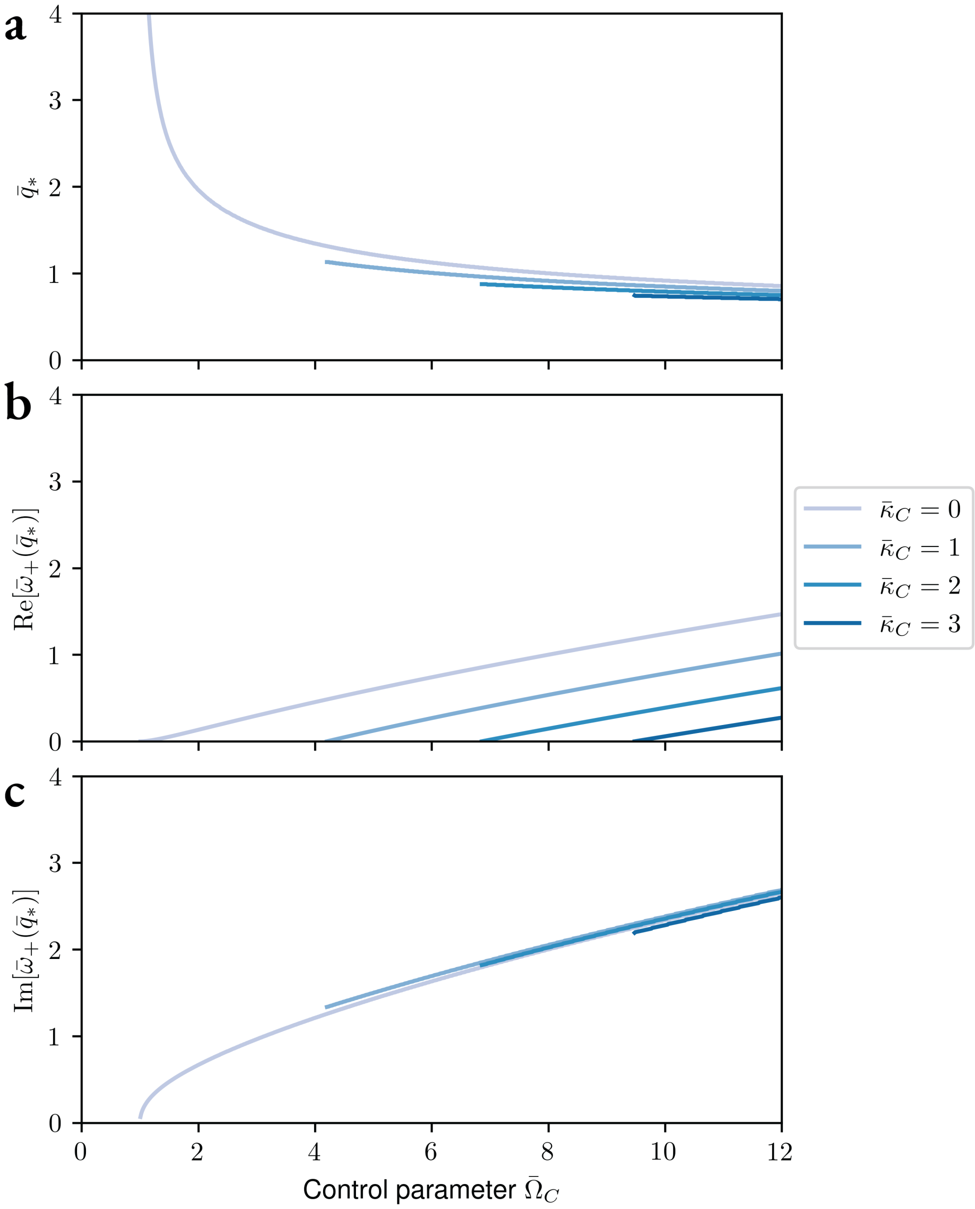

Figure 3.20: Properties of the most unstable mode as a function of $\bar{\Omega}_C$ (**a**) wave vector $\bar{q}_*$ (**b**) real part of the angular frequency (**c**) imaginary part of the angular frequency

$$\frac{\bar{q}_1}{\bar{q}_2}\frac{\bar{q}_2+\frac{\bar{k}_C}{1+\bar{\omega}}}{\bar{q}_1+\frac{\bar{k}_C}{1+\bar{\omega}}}-\mathrm{e}^{(\bar{q}_1-\bar{q}_2)\bar{L}_C}. \tag{3.58}$$

Remarkably, as in the case of limit of shear friction, the case of no basal shear rigidity $\bar{k}_C = 0$, corresponds to the case $\bar{q}_1 = \bar{q}_2 + 2\mathrm{i}\pi n/\bar{L}_C$. Therefore, the complex angular frequencies can be written as the solutions of the following family of polynomials:

$$\frac{\bar{\Omega}_C^2}{4}+(\bar{\kappa}_C+\bar{\omega})(1+\bar{\omega})^2\left(1+\frac{\pi^2 n^2}{\bar{L}_C^2}(\bar{\kappa}_C+\bar{\omega})\right)=0. \tag{3.59}$$

Looking for pair of solutions $\{\bar{\Omega}_C = \bar{\Omega}_{C,n}, \bar{\omega} = \pm\mathrm{i}\bar{\omega}_n\}$, we find that the filament becomes unstable, with the following values of the complex angular frequency and the control parameter at the onset of the instability:

$$\bar{\omega}_n = \sqrt{\frac{2\bar{\kappa}_C\left(\frac{\pi^2 n^2}{\bar{L}_C^2}(1+\bar{\kappa}_C)+1\right)+1}{2\frac{\pi^2 n^2}{\bar{L}_C^2}(1+\bar{\kappa}_C)+1}}, \tag{3.60}$$

$$\bar{\Omega}_{C,n} = \pm 2\sqrt{2}(1+\bar{\kappa}_C)\frac{1+\frac{\pi^2 n^2}{\bar{L}_C^2}(1+\bar{\kappa}_C)}{1+\frac{2\pi^2 n^2}{\bar{L}_C^2}(1+\bar{\kappa}_C)}\sqrt{1+\frac{2\pi^2 n^2}{\bar{L}_C^2}\bar{\kappa}_C}. \tag{3.61}$$

The limit of no bending rigidity yields:

$$\lim_{\bar{\kappa}_C\to 0}\bar{\omega}_n = \sqrt{\frac{1}{1+2\frac{\pi^2 n^2}{\bar{L}_C^2}}}, \tag{3.62}$$

$$\lim_{\bar{\kappa}_C\to 0}\bar{\Omega}_{C,n} = \pm 2\sqrt{2}\frac{1+\frac{\pi^2 n^2}{\bar{L}_C^2}}{1+2\frac{\pi^2 n^2}{\bar{L}_C^2}}, \tag{3.63}$$

in this case, the first unstable mode corresponds to the limit $n \to \infty$, where $\bar{\Omega}_{C,\infty} = \pm\sqrt{2}$ is the onset of the instability, which $\bar{\omega}_\infty = 0$. This is in agreement with the analysis of the infinite filament. Therefore the case $\bar{\kappa}_C \to 0$ leads to an ultraviolet divergence, where the first unstable modes correspond to infinitely small wavelengths. Finite values of the shear regularise the transition, such that the first unstable mode is finite. See figure A.1 for the distribution of the complex angular frequencies on the complex plane.

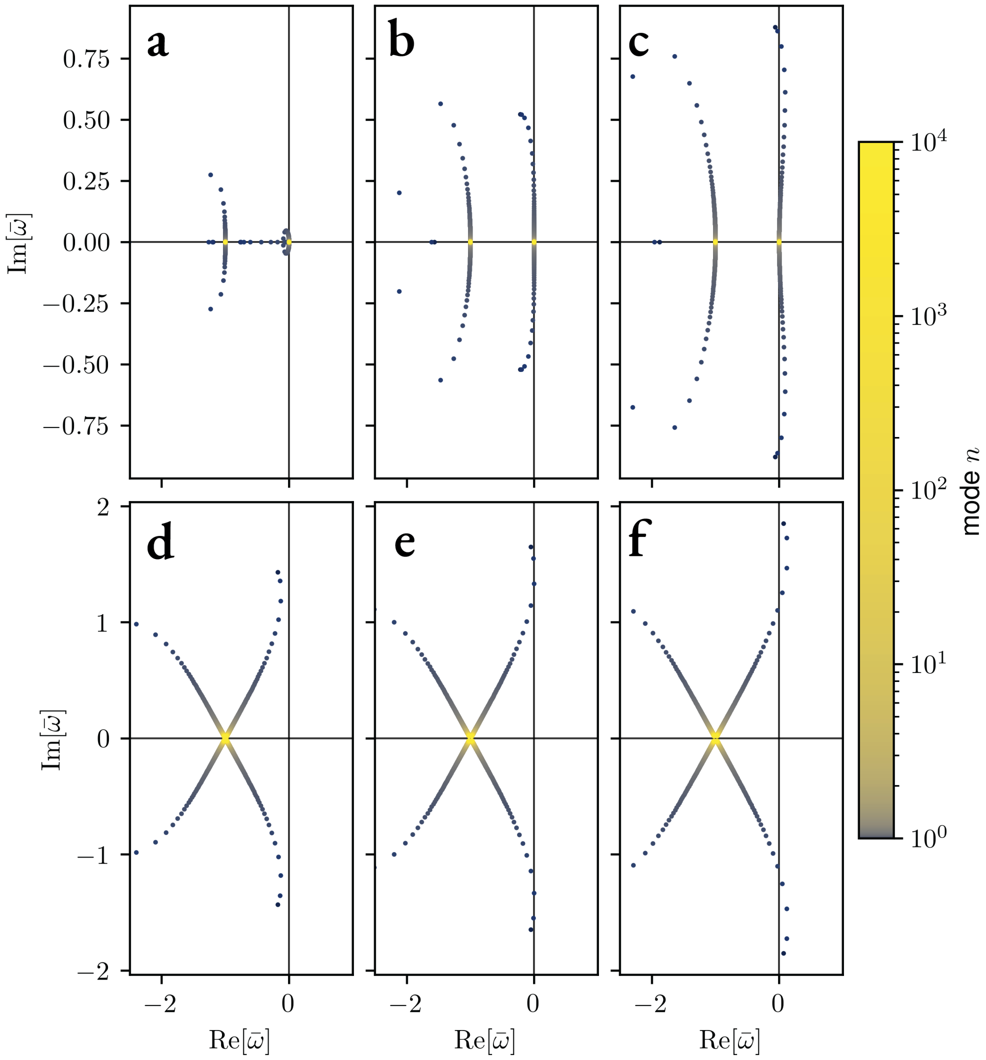

Figure 3.21: Distribution of the angular frequencies in the complex plane. Each mode, indexed by $n \in \{0, \cdots 10^4\}$ corresponds to two pairs of angular frequencies. For $\bar{\kappa}_C = 0$ the plots correspond to (**a**) Angular frequencies for $\bar{\Omega}_C = \sqrt{2} - 1$, (**b**) for $\bar{\Omega}_C = \sqrt{2}$, where the system is at the instability threshold, (**c**) for $\bar{\Omega}_C = \sqrt{2} + 1$ infinitely many modes are unstable. For $\bar{\kappa}_C = 0$ we have (**d**) Angular frequencies for $\bar{\Omega}_C \simeq 4.25$, (**e**) for $\bar{\Omega}_C \simeq 5.2$, where the instability occurs for $n = 2$ (**f**) for $\bar{\Omega}_C \simeq 6.25$ finitely many modes are unstable.

3.6 Relevant regimes for biological flagella

We discuss in this section the values of the parameters and friction coefficients relevant for biological cilia and flagella. Is there a dominant friction, or are cilia and flagella better described by an intermediate regime, in which than one kind of friction is relevant? Cilia and flagella are constituted of an axoneme—comprising a constant number of microtubules and a constant density of dynein along its length—and a membrane which varies in diameter, with a thicker base and a thinner tip. We assume that the contributions of the membrane to the shear and bending rigidities and to the shear and curvature frictions are small in comparison with the axonemal contribution. Because the external friction has a logarithmic dependence on the diameter, it is also nearly constant along the filament. Therefore we assume that a homogeneous filament is a good approximation of biological cilia and flagella.

As seen before, the dominant regime governing the dynamics of the filament is found by computing the ratio between the friction coefficients, multiplied the square of the wavevector. The dimensionless wavenumber $\bar{q}$, in units adapted to each symptomatic regime, is of order one. Therefore the dimensional wavevetor is always inversely proportional to the characteristic unit length for either the dominant external friction limit $\mu_\perp = (\kappa_C/(\xi_\perp k_\mathrm{d}))^{1/4}$, the dominant shear friction limit $\mu_\Delta = \sqrt{\kappa_C/(\xi_\Delta k_\mathrm{d})}$, and dominant curvature friction limit $\mu_C = \sqrt{\xi_C k_\mathrm{d}/\kappa_\Delta}$. The conditions for external friction to dominate is: $\xi_\Delta/\xi_\perp \ll \mu_\perp^2$, while the condition for internal shear friction to dominate is $\xi_\Delta/\xi_\perp \gg \mu_\Delta^2 \gg \xi_C/\xi_\Delta$. Finally for curvature friction to dominate we require $\xi_C/\xi_\Delta \gg \mu_C^2$. We therefore need only to compare length-scales to know wether a single mode of friction is dominant. For external friction to dominate we require:

$$\xi_\Delta \ll \sqrt{\frac{\xi_\perp \kappa_C}{k_\mathrm{d}}}. \tag{3.64}$$

Water has a friction coefficient of around $\xi_\perp \simeq 6 \times 10^{-3}\,\mathrm{Pa\,s}$, while the bending rigidity for an axoneme can be estimated to be $\kappa_C \simeq 580\,\mathrm{pN\,\mu m^2}$, with a frequency $f \simeq 60\,\mathrm{s}^{-1}$ [108]. The dimensionless frequency in the case of dominant external friction is $\bar{f} \simeq 0.5$, therefore $k_\mathrm{d} \simeq 120\,\mathrm{s}^{-1}$. For external friction to dominate, it must be the case that $\xi_\Delta \ll 0.17\,\mathrm{pN\,s}$.

The conditions for internal shear friction to dominate are:

$$\xi_\Delta \gg \sqrt{\frac{\xi_\perp \kappa_C}{k_\mathrm{d}}}, \tag{3.65}$$

$$\xi_C \ll \frac{\kappa_C}{k_\mathrm{d}}. \tag{3.66}$$

Because the dimensionless frequency in the case of dominant shear friction is $\bar{f} \simeq 0.2$, we have $k_\mathrm{d} \simeq 300\,\mathrm{s}^{-1}$. Using our estimates for the bending rigidity, the curvature friction coefficient can be neglected if $\xi_C \ll 1.9\,\mathrm{pN}\,\mu\mathrm{m}^2\,\mathrm{s}$.

Likewise, for curvature friction to dominate we have:

$$\xi_\Delta \ll \frac{\kappa_\Delta}{k_\mathrm{d}}. \qquad (3.67)$$

We estimate the shear rigidity to be $\kappa_\Delta = 2\,\mathrm{pN}$. The value is given by the rigidity from the shear deformation of $1\,\mathrm{nm}$ of an axoneme of $1\,\mu\mathrm{m}$ in length [127], multiplied by the square of a typical inter-doublet distance of $\sim 30\,\mathrm{nm}$ [128–130]. We take a typical dimensionless frequency in the case of dominant curvature friction of $\bar{f} \simeq 3$, therefore $k_\mathrm{d} = 20\,\mathrm{s}^{-1}$. Thus, curvature friction dominates over shear friction if $\xi_\Delta \ll 0.1\,\mathrm{pN\,s}$.

To decide the relevant regime for a biological flagellum, we must estimate the flagellar shear friction coefficient ξ_Δ, and the flagellar curvature friction coefficient ξ_C. The shear friction for an axoneme.

The shear friction coefficient is such that $\xi_\Delta = \rho a^2 k_\mathrm{m} \tau_\mathrm{m} \simeq 1\,\mathrm{pN\,s}$, where $\rho \simeq 100\,\mu\mathrm{m}^{-1}$ is the density of dyneins along the axoneme, $a \simeq 30\,\mathrm{nm}$ is the inter micro-tubule pair distance, $k_\mathrm{m} \simeq 100\,\mathrm{pN\,nm}^{-1}$ is the rigidity of dyneins in the weak binding-state, while $\tau_\mathrm{m} \simeq 10^{-4}\,\mathrm{s}$ is the life-time of the dynein cross-bridge in the weak binding state [103, 131]. We estimate the curvature friction coefficient to be 20 times the curvature friction of a single micro-tubule, so that $\xi_C \simeq 0.8\,\mathrm{pN}\,\mu\mathrm{m}^2\,\mathrm{s}$ [39, 100, 132, 133].

We conclude that the dynamics of a biological flagellum is well described by a limit of dominant internal friction, with the most important contribution to the dynamics due to shear friction. However curvature friction, while small, cannot be fully neglected.

CHAPTER 4

STUDY OF RECONSTITUTED ACTOMYOSIN BUNDLES

4.1 INTRODUCTION

Artificial active filaments have been developed in laboratory, using biological proteins, such as cytoskeletal filaments and molecular motors. This class of systems gives fundamental insights into the characteristics of the constituent proteins, and their collective behaviour. It also gives insight into the self-organised beating of slender filaments, giving strong evidence, that spontaneous oscillations, are a generic property of filament-motor systems, instead of being a specific property, heavily dependent on the microscopic details of a given system.

The first artificial active filament that were studied, are reconstituted microtubule bundles driven by clusters of kinesin molecular motors [16]. These bundles, attached to air bubbles, and formed with the help of the depleting agent polyethylene glycol, exhibit spontaneous oscillations. Biological cilia and flagella, in contrast, are driven by dynein molecular motors. Therefore, spontaneous beating of active filaments is not dependent on the properties of the dyneins themselves.

The second type of artificial active filament to be engineered [17], are actin bundles formed by growing actin filaments from a nucleation site in the presence of myosin molecular motors, and the depleting agent methylcellulose. These filaments and motors assemble into bundles and spontaneously oscillate. In this case, both the molecular motor and the cystoskeletal filaments are different from those of a biological flagellum.

In the present chapter, we first describe the phenomenology of the active actin filament bundle's dynamics, and then we adapt the framework developed in chapter 2, to describe the experimental data. In particular, we take into account the heterogeneous nature of actin-bundles, which are structures constituted of many actin filaments of various lengths. We also take into account the myosin molecular motors, which exhibit nonlinear dynamics coupled to the bundle's shape.

4.2 ACTIVE ACTIN FILAMENT BUNDLES

In the presence of myosin motors and ATP, and a depleting agent, polymerising actin filaments and myosin molecular motor self-assemble into bundles *in vitro*, which exhibit spontaneous beating, with travelling bending waves moving from the base to-

Parameter	Definition	myosin-II	myosin-V
$L\,(\mu\mathrm{m})$	Bundle length	15.9 ± 6.1	18.3 ± 5.4
$\ell\,(\mu\mathrm{m})$	Wavelength of bending waves	17.1 ± 6.1	15.88 ± 3.52
$T\,(\mathrm{s})$	Tangent-angle period	15 ± 9	53.6 ± 27.1
$v\,(\mu\mathrm{m\,s^{-1}})$	Bending-wave phase velocity	1.6 ± 0.8	0.57 ± 0.15
$v_\mathrm{m}\,(\mu\mathrm{m\,s^{-1}})$	Myosin-density wave velocity	n.a.	0.7 ± 0.2
$T_\mathrm{m}\,(\mathrm{s})$	Myosin-density wave period	n.a.	41.1 ± 12.4

Table 4.a: Parameters of the beating patterns of actomyosin bundles. The numerical values for the properties of the bundle's beating are given over mean of $n = 59$ bundles for myosin-II and $n = 29$ bundles for myosin-V, the numerical values for the properties of the myosin-density wave are given over a mean of $n = 10$ bundles for the period T_m and $n = 17$ for the speed v_m. There is no statistical difference between the mean lengths and wavelengths of bundles driven by myosin-II and myosin-V.

wards the bundle's distal end. The properties of the actin bundle's beating resemble, qualitatively, those of eukaryotic cilia and flagella. This is despite the very different molecular components of the bundle, and lack of any cellular regulatory mechanism. The bending waves are associated with myosin-density waves, travelling from a basal recruitment zone, towards the distal end, going almost twice as fast as the mechanical waves [17].

Actin filaments are polar, with a (-) and a (+) end, called the barbed end. Actin filaments grow by monomer addition on the barbed end. The actin filaments grow perpendicularly from the border of surface micro-patterns of nucleation-promoting factor [134]. Each actin filament has a different length, with the total lengths following an exponential distribution, with a mean length of $\lambda = 8\ \mu\mathrm{m}$ [135]. The inclusion of methylcellulose, a depleting agent, ensured that most filaments grew parallel to the substrate, ensuring nearly-planar beating of the aforementioned bundles.

The molecular motors used in the experiments were either heavy meromyosin-II (hereafter myosin-II), or myosin-Va fragment (hereafter myosin-V), fused to green fluorescent protein (GFP). Myosin-II is a non-processive motor, it detaches from the filament after a power-stroke, while myosin-V is processive, moving towards the barbed end of actin filaments. Spontaneous bending waves occur with both molecular motor

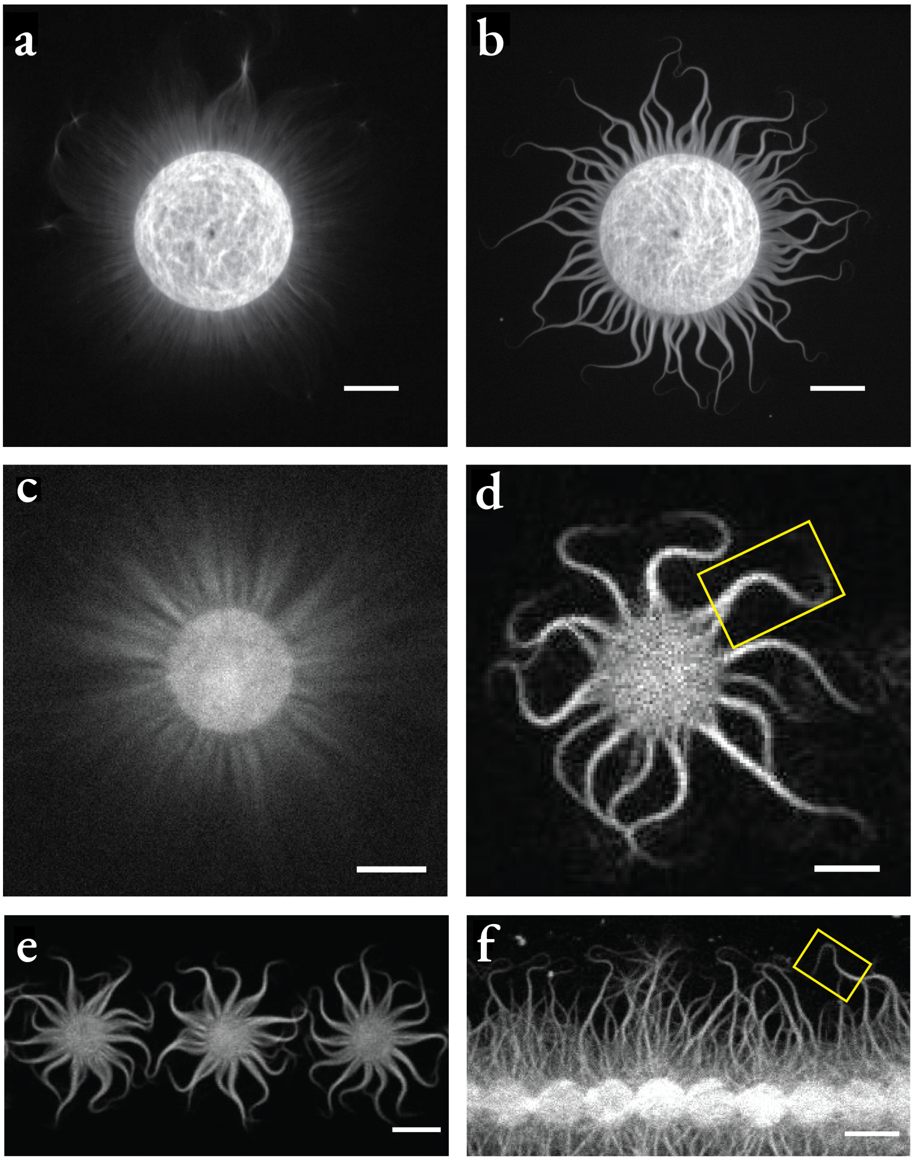

Figure 4.1: Actin micro-patterns and actin bundles driven by myosin (**a**) actin filaments growing radially out of a nucleation disk of 60 µm of diameter, in the presence of methylcellulose (**b**) actin filaments growing radially out of a nucleation disk of 60 µm of diameter, in the presence of methylcellulose and myosin-II molecular motors and ATP (**c**) nucleation disk of 9 µm of diameter with radial actin filaments (**d**) nucleation disk of 9 µm of diameter with bundled actin filaments in the presence of myosin-II and ATP, the yellow rectangle corresponds to the bundle shown in figure 4.2 (**e**) nucleation disks of 9 µm of diameter with bundled actin filaments in the presence of myosin-V and ATP (**f**) line of nucleation disks with bundles driven by myosin-V, the yellow rectangle corresponds to the bundle shown in figures 4.3 and 4.3. Scale bars: 20 µm in (a) and (b), 5 µm in (c) and (d), 10 µm in (e) and (f).

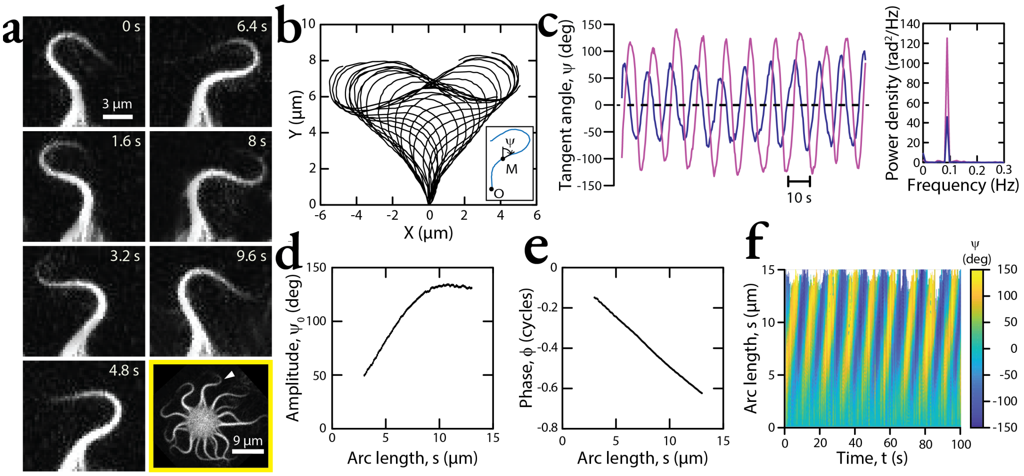

Figure 4.2: Actin bundle driven by myosin II (**a**) snapshots of a bundle of length $L = 14.8\,\mu\text{m}$ shown with the arrow in the yellow box. (**b**) Beating patterns exhibit a heart shape and an infinity symbol. (**c**) Tangent angle oscillations as a function of time at $s = 5\,\mu\text{m}$ (purple) and $s = 10\,\mu\text{m}$ (magenta) with corresponding power spectral densities at the right (**d**) Amplitude of the tangent angle as a function of the arc-length (**e**)Phase of the tangent angle as a function of the arc-length (**f**) Color plot of the tangent angle as a function of time and the arc-length.

types. The oscillations driven by both molecular motors is similar, however, myosin-V is a slower molecular motor, which is reflected in a longer beating period and slower wave propagation. The details of actin bundle waves are written in table 4.a. The velocity of tangent-angle wave propagation is nearly constant along the bundle's length, and across bundles. Uniform phase velocity is remarkable, because the actin bundles are heterogeneous structures, with their thickness going from about one micrometer thick at the base, with around a thousand individual actin filaments, to a tip with only a hundred actin filaments. Uniform phase velocities have been observed in flagellar beating [80, 136], however, biological flagella have a constant number of microtubule pairs along its length. For a heterogeneous bundle, constant speed is most easily explained if an internal friction dominates, because parameters describing the internal dynamics of the filament are directly proportional to the number of actin filaments, while external friction depends on the logarithm of the number of filaments. In order to verify this assumption, the relative importance of internal and external friction coefficients will be estimated.

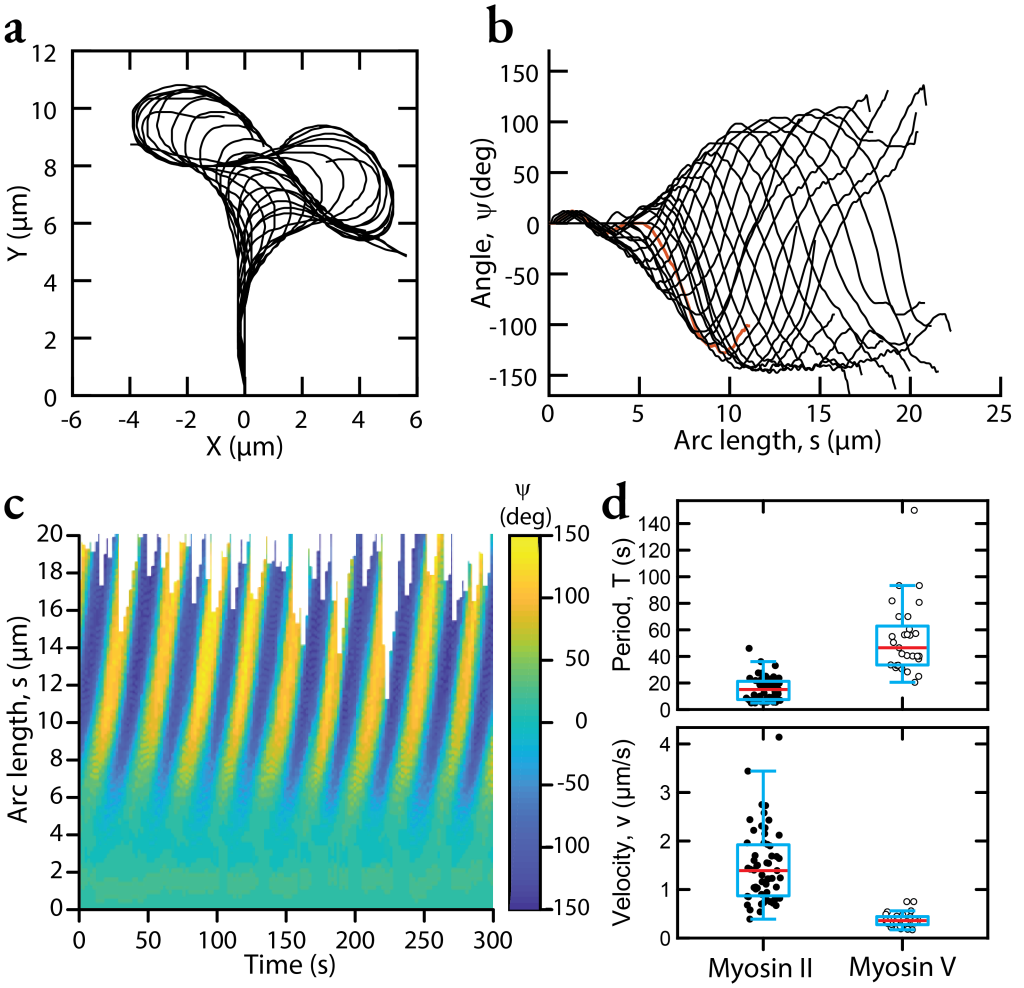

Figure 4.3: Active actin bundle driven by myosin-V: (**a**) beating pattern, (**b**) tangent angle oscillations over one period with a 2 s time step, (**c**) Color plot of the tangent angle as a function of time and the arc-length, (**d**) Period (top) and velocity (bottom) of tangent angle oscillations, driven by myosin-II (black dots, left) and myosin-V (white dots, right), the box-plots indicate 25th and 75th percentiles with median values in red.

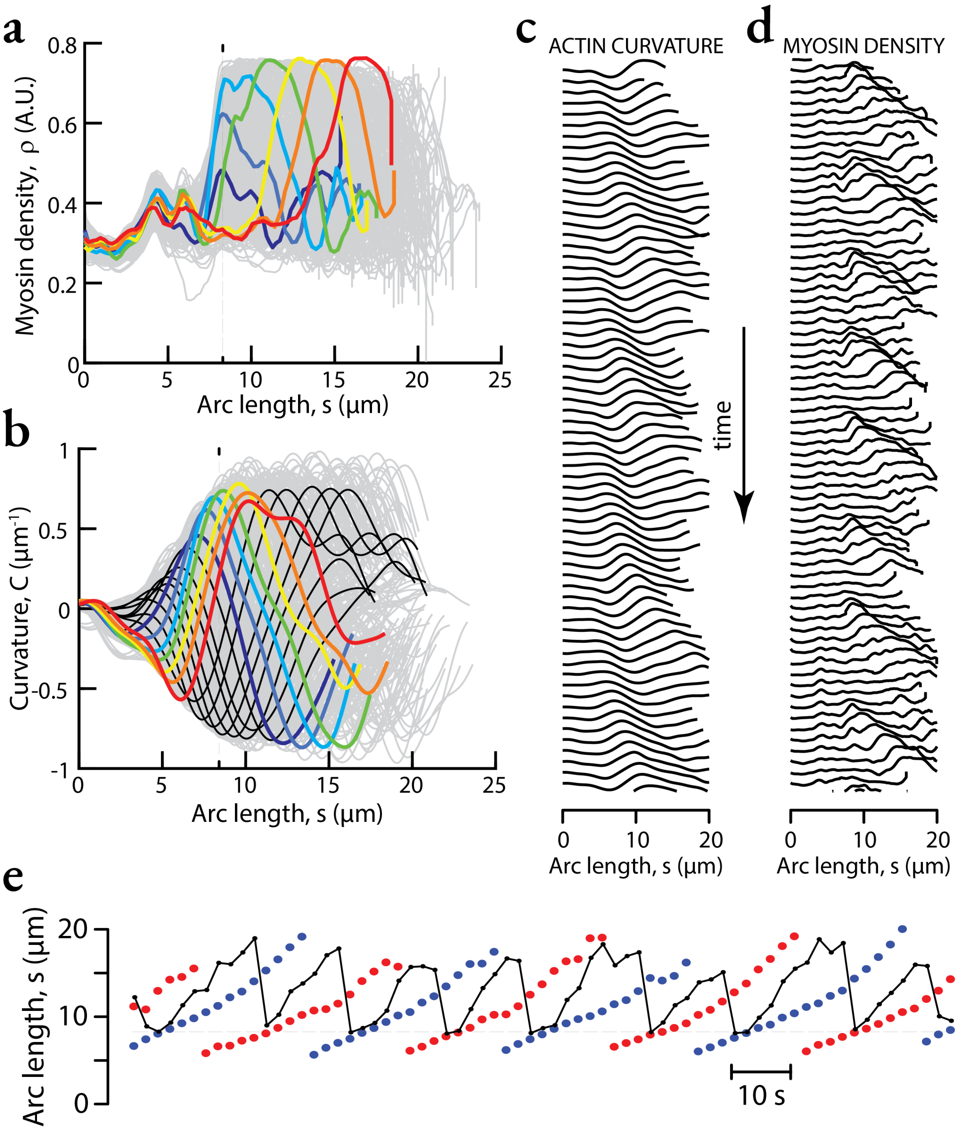

Figure 4.4: Dynamic interplay between actin-bundle's bending waves and myosin-density waves: (**a**) myosin-density waveform snapshots over twenty-two periods in light grey, snapshots over one myosin-density period in color from dar blue to dark red, (**b**) actin-bundle's curvatures snapshots over twenty-two periods in light grey, snapshots over one curvature period in black, colored snapshots in (a) and (b) correspond to the same times, (**c**) kymograph of the actin bundle's curvature over time with a 2 s time-step, (**d**) kymograph of the myosin density profile with same time-step, (**e**) position along the bundle's arc length of the curvature maxima (red dots ●) and minima (blue dots ●), and position of the myosin-density maxima (black line) over time.

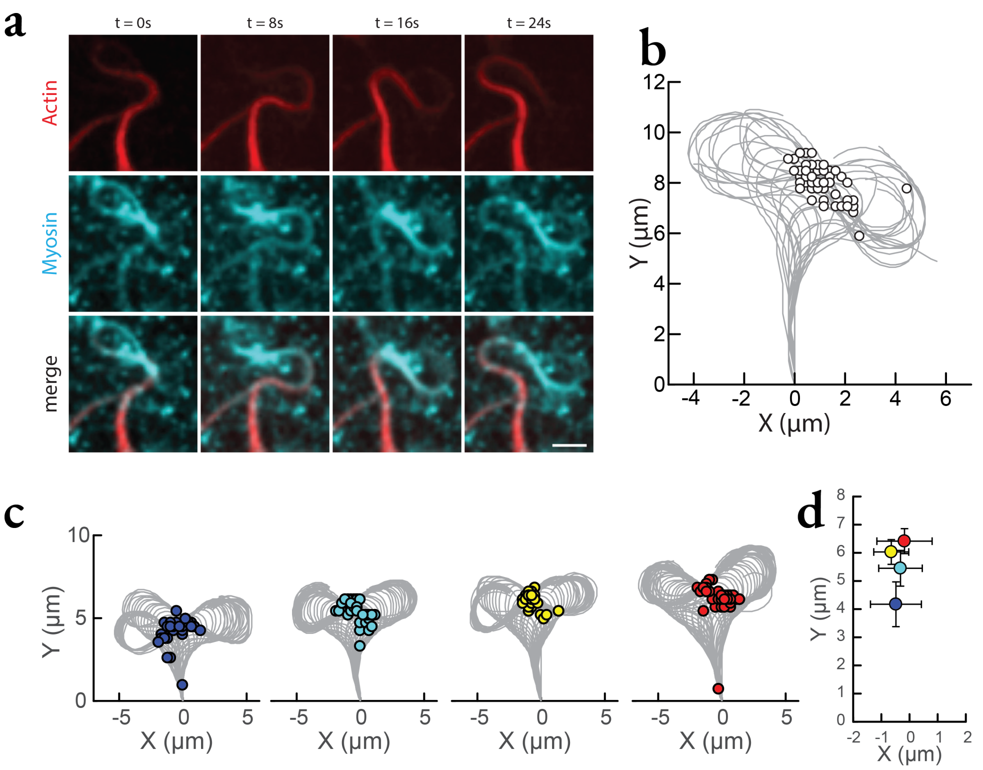

Figure 4.5: Bundle distribution of myosin-density: (**a**) fluorescence images at different time-steps for actin (red), myosin-V (cyan) and the superposition of both signs at the bottom, (**b**) Position of the myosin density peaks in the bundle, (**c**) Position of the myosin density peaks for an individual bundle which grows with time, (**d**) mean position of myosin density peak shown in (c).

MYOSIN-DENSITY WAVES

Because myosin-V is labelled with GFP, myosin-V density could be observed experimentally through fluorescence intensity measurements. Myosin-V density exhibits wave behaviour, with the abrupt apparition of a density peak near the base of the flagellum, which then travels towards the distal end. As seen in figure 4.5, the shape of the peak conforms dynamically to the local shape of the bundle, elongating as the bundle becomes thinner.

Comparing the myosin-V density profile, with the local curvature profile along the bundle, it is possible to observe that the frequency of myosin-density waves is twice the frequency of the bundle's oscillation, corresponding to a period of about 41.1 ± 12.4 s for the myosin-density wave and a period of about 20.7 ± 6.0 s for the bundle beating. We remark that the number shown here for the bundle is different from the one in table 4.a, this is because these numbers come from a subsection of $n = 10$ observations, corresponding to a third of the total number of observations made on the actin bundles driven by myosin-V. The observed speed of the myosin-density waves is 1.4 to 3 times larger than observed speed of myosin-V in gliding or bead assays [47, 137, 138], but comparable to the speed of single myosin-V motors on actin filaments [139], and *in vivo* cellular transport velocities [140]. Whether the myosin-density wave velocity is due to the processivity of myosin-V molecular motors, or due to some other collective mechanism, is not known

The myosin-V density peak appears in a basal region characterised by a threshold curvature $C^* = 0.65 \pm 0.09\,\mu\mathrm{m}^{-1}$, at an arc-length of $s^* = 6.9 \pm 1.8\,\mu\mathrm{m}$, after which the bundle curvature and tangent angle reaches a plateau. As the myosin-wave density peak travels towards the distal end, it does not change in magnitude, and remains saturated. Because the myosin-density wave travels faster than the curvature wave, the myosin-density peak does not colocalize with the curvature extrema. The observations suggest that the myosin recruitment is triggered by curvature, but only at the base, after which it is not recruited anymore.

ESTIMATES OF EXTERNAL AND INTERNAL FRICTION

We first determine which friction contribution is most important in the dynamics of the actin bundle, in particular, whether the bundle's dynamics are better described by a regime dominated by either external or internal friction. To do this we estimate the values of the different friction coefficients, which are compared to the observed wavevector of the bundle's travelling bending wave. In the actin bundle, the wavelength is of the order of the total length of the bundle, therefore $q \simeq 2\pi/L$.

The hydrodynamic friction coefficient is given by $\xi_\perp \simeq 4\pi\eta/\log(L/D) \simeq 45 \times 10^{-3}\,\mathrm{Pa\,s}$, were $\eta \simeq 15 \times 10^{-3}\,\mathrm{Pa\,s}$ is the viscosity of the methylcellulose solutions used in the experiments, and the logarithm is of order $3 \sim 4$, with $D \propto \sqrt{N(s)}$, and where $N(s) = N_0 \exp(-s/\lambda)$ is the number of filaments at any given point along the bundle, with $N_0 \simeq 1000$.

Shear friction is given by $\xi_\Delta = N(s)\xi_\Delta^0$, and $\xi_\Delta^0 = \rho a^2 k_\mathrm{m} \tau_\mathrm{m} \simeq 10^{-2}\,\mathrm{pN\,s}$ is the shear friction per filament [103], where $\rho \simeq 6\,\mu\mathrm{m}^{-1}$ is the density of myosin motors per filament, $a \simeq 30\,\mathrm{nm}$ is the inter-filament spacing comparable to the myosin stepsize, $k_\mathrm{m} \simeq 0.2\,\mathrm{pN\,nm}^{-1}$ is the myosin stiffness [141], and $\tau_\mathrm{m} = 50\,\mathrm{ms}$ is the lifetime of a myosin-cross bridge at stall force [142–144].

The curvature friction is difficult to estimate, the relaxation of a single actin filament in a fluid is dominated by external viscous friction, not internal friction [133], however, microtubules are two orders of magnitude stiffer than actin filaments [40, 133], assuming the same order of magnitude holds for the difference in curvature friction, we estimate the bundle's curvature friction to be $\xi_C = N(s)\xi_C^0$, with the curvature friction per filament being $\xi_C^0 = 6 \times 10^{-3}$ pN µm^2 s.

To determine which friction dominates, we define the following three quantities:

$$\alpha = \frac{\xi_\Delta^0}{\xi_\perp}\frac{4\pi^2}{L^2}N(s), \tag{4.1}$$

$$\beta = \frac{\xi_C^0}{\xi_\Delta^0}\frac{4\pi^2}{L^2}, \tag{4.2}$$

$$\gamma = \frac{\xi_C^0}{\xi_\perp}\frac{16\pi^4}{L^4}N(s), \tag{4.3}$$

where $N(0) = 1000$ and $N(L) \simeq 82$. If $\alpha \gg 1$ the limit of dominant internal friction is valid, if $\beta \ll 1$ then shear friction is dominant over curvature friction, which can be neglected, while if $\gamma \gg 1$ curvature friction dominates is dominant over external. Using the above estimates for the friction coefficients, we compute the ranges for the aforementioned quantities: $\alpha \in [2, 20]$, $\beta \simeq 0.06$ and $\gamma \in [0.13, 1.3]$. The effects of internal shear friction in relation to external friction ranges from comparable, near the tip, to dominant at the base.

4.3 THEORETICAL DESCRIPTION OF ACTIN BUNDLES

EQUATIONS OF MOTION

In this section we adapt the theory presented in chapter 2 to take into account experimental observations. Because the number of filaments along the bundle follows an exponential distribution, the bundle is heterogeneous. The parameters describing the bundle's dynamics depend locally on the number of filaments, and therefore depend on the position. While Δ and ψ do not depend on the number of filament, the active moment m_a does, because the number of possible sites were a molecular motor may generate torque depends on the number of filament pairs. Recalling that the beating of the actin bundles is nearly planar, molecular motors cross-linking a pair perpendicular to the beating plane do not contribute to an observed change of shape, therefore we assume that the active moment defined in section 2.4.3 has the form $m_\text{a} = AN(s)\rho_\text{a}$, where A is the magnitude of the torque generated by a myosin cross-link, and $\rho_\text{a} = \rho_+ - \rho_-$ is the asymmetric density of cross-links, whith $\rho_\pm$ the lineic densities per filament pairs of motor cross-links producing clock-wise or counter clock-wise torques. The actin bundles grow with time, we will assume that this growth is adiabatic, such that the filament can be taken to be of constant length over one beating period.

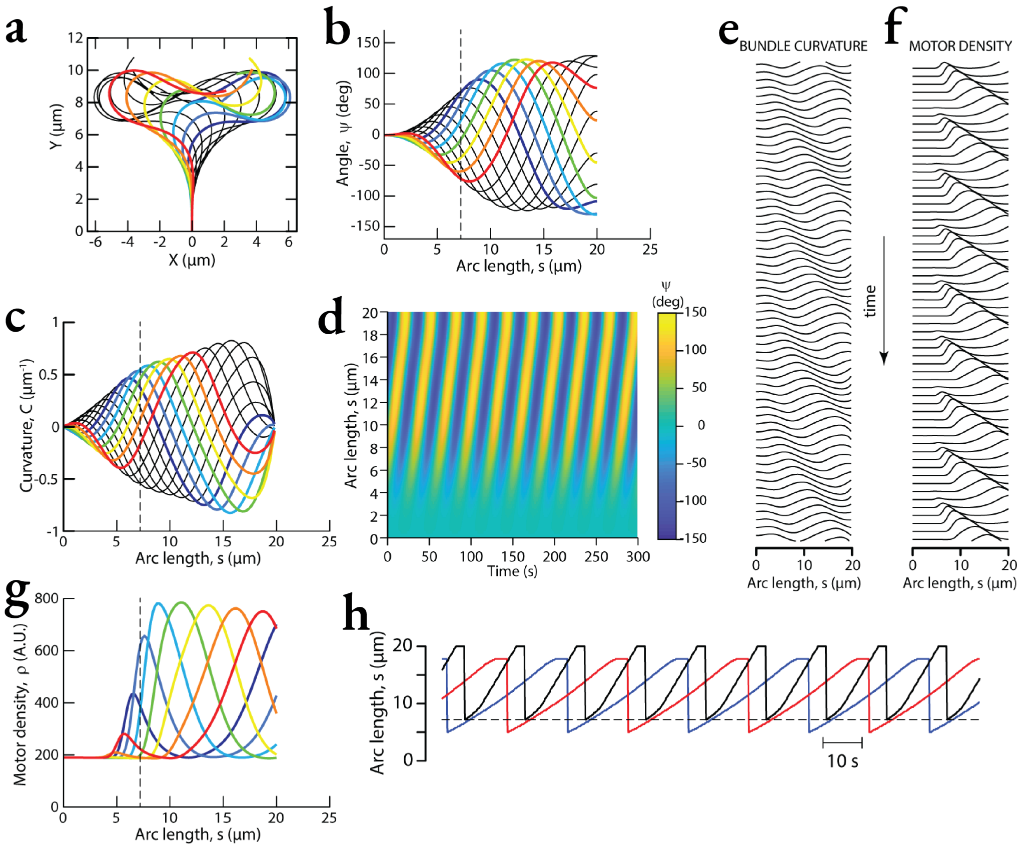

Figure 4.6: Numerical solutions of equations of motion (4.4,4.6,4.8): (**a**) spatial conformation of bundle over time, (**b**) tangent angle profiles, (**c**) and curvature profiles as a function of the arc length over time, (**e**) color plot of tangent angle showcasing uniform wave propagation, (**e**) kymograph of bundle curvature (**f**) and motor density over time with a time-step of 2.2 s, (**g**) myosin density profile over time, colours in (a), (b), (c) and (g) correspond to different times, going from blue (earlier) to read (later), so that the same color in all figures corresponds to the same time everywhere, with a time step of 2.2 s, the black lines go over the rest of one period, (**h**) position along arc-length of curvature maxima (red line), minima (blue line) and motor density maxima (black line) as a function of time. The dashed line in (b), (c) and (g) corresponds to the position were motor-density is abruptly recruited.

We must also describe an observable not considered in chapter 2, the total density of myosin molecular motors $\rho(s, t)$. Because the density is always positive, it does not obey the same symmetries of Δ and ρ_a, and therefore only non-linear couplings between ρ and ρ_a are allowed. In order to take into account the dynamic properties of the myosin density, we consider an evolution equation with an advection term and a source term. Because the myosin-density peak appears only after when curvature reaches a certain threshold, and because of symmetry considerations, the molecular motor recruitment must be a function square of the curvature. However, because myosin density is only recruited in a specified basal region of the bundle, the recruitment must also depend on the number of filaments. We therefore postulate the following form for the dynamics of the myosin density waves:

$$\partial_t \rho - v \partial_s \rho = N(s) k_\mathrm{on}(C^2, N(s)) - k_\mathrm{off} \rho, \tag{4.4}$$

where the nonlinear recruitment rate has a Hill function dependence on $CN(s)$:

$$k_\mathrm{on}(C, N(s)) = k_0 + k_1 \frac{\left(\frac{C}{C_0} N(s)\right)^{2m}}{1 + \left(\frac{C}{C_0} N(s)\right)^{2m}}. \tag{4.5}$$

The motor recruitment is large when both the magnitude of the curvature C and the number of filaments N are larger than a threshold curvature C_0. The integer m sets the strength of the nonlinearity, we choose large enough such that it approximates a step-function, but not infinite so as to avoid numerical instabilities. Equation (2.58) describing the time-evolution of the active moment becomes the equation for the asymmetric density:

$$\partial_t \rho_\mathrm{a} = k_\mathrm{a}^0 \partial_s \Delta - k_\mathrm{d} \rho_\mathrm{a} - \epsilon \rho \rho_\mathrm{a}^3, \tag{4.6}$$

where $k_\mathrm{a} = N(s) A k_\mathrm{a}^0$ and the nonlinearity has been modified to take into account the modulation of the asymmetric density by the total density of myosin. Because the nonlinearity becomes greater in areas of high myosin-density, which are themselves correlated to areas of high curvature, the nonlinearity also helps to describe the curvature saturation of the bundle. In principle if $\rho = 0$ we must have no recruitment, such that $k_\mathrm{a}^0 = 0$, however, the linear stability of the bundle is studied around some finite constant $\rho = \rho_0$, therefore variations around ρ_0 have only nonlinear effects on the dynamics.

We are now left with the equation of motion for the bundle shape. With the notable exception of the external friction coefficient, all parameters in the equation of motion (2.55) are inside derivatives with respect to s, therefore extra terms taking into account the heterogeneity appear in the linearised equation. Neglecting curvature friction and shear rigidity we have:

$$\frac{\xi_\perp(s)}{N_0 \mathrm{e}^{-\frac{s}{\lambda}}}\partial_t\psi = \left(\frac{1}{\lambda}-\partial_s\right)^2\left(\xi^0_\Delta\partial_t\Delta + \kappa^0_C\left(\frac{1}{\lambda}-\partial_s\right)\partial_s\Delta + A\rho_\mathrm{a}\right). \tag{4.7}$$

We observe that in the presence of external friction, there is an explicit arc-length dependence in the left-hand side. Because the observed phase speed of the bundle's waves is constant, and because the effects of external friction become only comparable to the effects of internal shear at the tip of the bundle, we assume that external friction can be neglected everywhere. Therefore the equation of motion for the bundle shape becomes:

$$\xi^0_\Delta\partial_t\Delta = \kappa^0_C\left(\partial_s-\frac{1}{\lambda}\right)\partial_s\Delta - A\rho_\mathrm{a}. \tag{4.8}$$

We will assume that the bundle's base is infinitely compliant to changes in shear, therefore the boundary conditions for the above equation are:

$$\partial_s\Delta(0,t) = 0, \tag{4.9}$$
$$\partial_s\Delta(L,t) = 0. \tag{4.10}$$

Equation (4.4) also requires a boundary condition, we choose a constant concentration of motors at the base, such that:

$$\rho(0,t) = \rho_0. \tag{4.11}$$

Equations (4.4, 4.6, 4.8) in conjunction with boundary conditions (4.9 – 4.11) fully specify the system's dynamics.

NUMERICAL SOLUTIONS

Using the same units as in section 3.4, where we recall the dimensionless unit time is $\bar{t} = k_\mathrm{d}t$, the dimensionless unit arc-length is $\bar{s} = s/\mu$, with $\mu = \sqrt{\kappa^0_C/(\xi^0_\Delta k_\mathrm{d})}$. The dimensionless asymmetric density is rescaled such that $\bar{\rho}_\mathrm{a} = \rho_\mathrm{a}\mu k^0_\mathrm{a}/k_\mathrm{d}$. The dimensionless equations of motion then become:

$$\partial_{\bar{t}}\Delta = -\frac{1}{\bar{\lambda}}\partial_{\bar{s}}\Delta + \partial^2_{\bar{s}}\Delta - \bar{\Omega}\bar{\rho}_\mathrm{a}, \tag{4.12}$$
$$\partial_{\bar{t}}\bar{\rho}_\mathrm{a} = \partial_{\bar{s}}\Delta - \bar{\rho}_\mathrm{a}, \tag{4.13}$$
$$\partial_{\bar{t}}\bar{\rho} + \bar{v}\partial_{\bar{s}}\bar{\rho} = \left(\bar{k}_0 + \bar{k}_1\frac{\left(\partial_{\bar{s}}\Delta/\bar{C}^*(\bar{s})\right)^{2m}}{1+\left(\partial_{\bar{s}}\Delta/\bar{C}^*(\bar{s})\right)^{2m}}\right)\mathrm{e}^{-\bar{s}/\bar{\lambda}} - \bar{k}_\mathrm{off}\bar{\rho}, \tag{4.14}$$

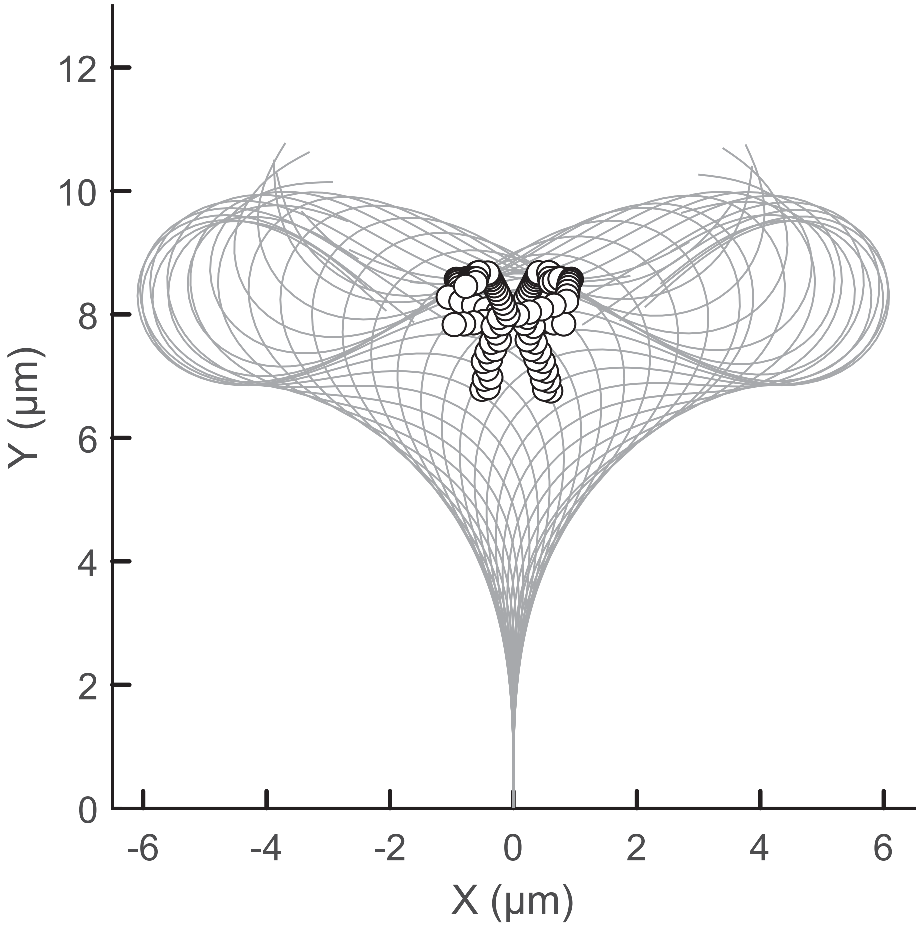

Figure 4.7: Numerical solutions of equations of motion (4.4, 4.6, 4.8), white dots correspond to spatial position of motor-density peak over time, over one bundle shape period (in grey). The trajectory of the motor density peaks forms a bow shape.

where the characteristic dimensionless curvature is $\bar{C}^*(\bar{s}) = \bar{C}_0 N_0 \exp(-\bar{s}/\bar{\lambda})$. The definition of the other parameters can be seen in table 4.b. Because there is no basal shear rigidity, and because the dynamics of ρ do not affect the linear stability analysis, we can find an analytical expression for the instability threshold, as a function of the dimensionless bundle length $\bar{L}$, and the mean dimensionless actin filament length $\bar{\lambda}$:

Dimensionless parameter	Definition	Relation to variables	Value
$\bar{L}$	Bundle length	$\bar{L} = \frac{L}{\mu}$	6
$\bar{\lambda}$	Mean-filament length	$\bar{\lambda} = \frac{\lambda}{\mu}$	8/3
$\bar{\Omega}$	Control parameter	$\bar{\Omega} = A\frac{k_{\mathrm{a}}^0}{k_{\mathrm{d}}}\frac{\mu}{\kappa_C^0}$	13.2
$\bar{\rho}_0$	Basal motor density	$\bar{\rho}_0 = \rho_0\mu$	150
$\bar{v}$	motor advection velocity	$\bar{v} = \frac{v}{k_{\mathrm{d}}\mu}$	5
$\bar{k}_0$	Constant motor binding rate	$\bar{k}_0 = \frac{k_0\mu N_0}{k_{\mathrm{d}}}$	15
$\bar{k}_1$	Mechanosensitive motor binding rate	$\bar{k}_1 = \frac{k_1\mu N_0}{k_{\mathrm{d}}}$	$3 \cdot 10^4$
$\bar{k}_{\mathrm{off}}$	Motor unbinding rate	$\bar{k}_{\mathrm{off}} = \frac{k_{\mathrm{off}}}{k_{\mathrm{d}}}$	0.1
$\bar{\epsilon}$	Magnitude of nonlinear $\bar{\rho}_{\mathrm{a}}$ unbinding rate	$\bar{\epsilon} = \frac{\epsilon k_{\mathrm{a}}^2}{(k_{\mathrm{d}}\mu)^3}$	0.08
$\bar{C}_0$	Magnitude of the critical curvature	$\bar{C}_0 = \frac{C_0\mu}{N_0}$	0.8

Table 4.b: Definition and values of dimensionless parameters for numerical solutions of Eqs. (4.12 – 4.14) shown in to Fig. 5 of the main text.

$$\bar{\Omega}_c = \frac{1}{4}\left(\frac{1}{\bar{\lambda}^2} + 4\left(\frac{\pi^2}{\bar{L}^2} + 1\right)\right)\left(\frac{1}{\bar{\lambda}^2} + \sqrt{\frac{1}{\bar{\lambda}^2} + 8}\right). \tag{4.15}$$

If $\bar{\Omega} \geq \bar{\Omega}_c$, the bundle is unstable. For $\bar{L} = 6$ and $\bar{\lambda} = 8/3$ the critical value of the control parameter is $\bar{\Omega}_c \simeq 3.9$. As in chapter 3, the equations of motion can be solved with a modified Crank-Nicolson finite difference scheme [126]. Solutions for the dynamics of a bundle in the nonlinear regime ($\bar{\Omega} = 13.2$) can be seen in figure 4.6 with parameter values written in table 4.b. The numerical solutions exhibit the main characteristics of a beating actin bundle: heart shape displaying an infinity symbol; uniform tangent-angle wave velocity; saturation of the tangent angle and of the curvature; abrupt recruitment of myosin molecular motors; myosin density peak velocity higher than the tangent-angle wave speed; motor-density peak localised at the centre of the heart shape (see figure 4.7).

We compare the numerical solutions with a bundle of length $L = 20\,\mu\mathrm{m}$, and a beating period $T = 30.62\,\mathrm{s}$. This enables us to estimate the value of remaining parameters: we compute $\mu = L/\bar{L} \simeq 3.33\,\mu\mathrm{m}$ and $k_\mathrm{d} = \bar{T}/T \simeq 6.73 \times 10^{-2}\,\mathrm{s}^{-1}$, therefore the relaxation time of the active moment is $k_\mathrm{d}^{-1} \simeq 14.86\,\mathrm{s}$. The bending rigidity of a single actin filament is $\kappa_0 = 4 \times 10^{-2}\,\mathrm{pN}\,\mu\mathrm{m}^2$ [145], therefore we independently estimate the shear friction coefficient per filament pair as $\xi_\Delta^0 = \kappa_C^0/(\mu^2 k_\mathrm{d}) \simeq 5.35 \times 10^{-2}\,\mathrm{pN\,s}$ which is consistent with the estimate in the previous subsection 4.2.

The magnitude of the torque generated by a single cross-link is $A = aF_\mathrm{stall} \simeq 75\,\mathrm{pN\,nm}$, given by the magnitude of the stall force $F_\mathrm{stall} \simeq 2.5\,\mathrm{pN}$ exerted by a myosin-V molecular motor [47,142,143,146,147] multiplied by the estimated distance between actin filaments in a bundle of $a \simeq 30\,\mathrm{nm}$, similar to the step-size of myosin-V. With the relations given in table 4.b, all other parameters can be estimated, and are given in table 4.c.

4.4 DISCUSSION

The theoretical framework developed in the previous chapters, and modified to take into account the specifics of an active actin bundle, captures qualitatively the key behaviour of the experimental bundle. It does so in a regime which was not explored before, and with realistic parameter values. However the value of the active moment's relaxation time $1/k_\mathrm{d}$, is much longer than the relaxation time of myosin molecular motors [142–144]. Because the active moment results from the collective behaviour of the individual molecular motors, it would be expected to obtain a relaxation time of the same order of magnitude. What sets the value of k_d as a function of the properties of this motor-filament system is, therefore, an important open question.

Not presented in the current chapter is the dependence of the bundle's beating properties on the bundle's length. The dependence is not trivial, in particular the wavelength and the period of bending waves grows linearly with the bundle length, therefore the phase velocity is constant [17]. The current theory cannot explain the behaviour, instead the wavelength and the period are primarily set by the value of the control parameter, therefore implying that the control parameter also has a hidden length dependence. See Figure 4.8.

The theory presented here assumes that the parameters depend linearly on the number of actin filaments. While not an outlandish assumption, the dependence might be more complex. In particular the bending rigidity depends linearly on the number of filaments only if the filaments are decoupled, and able to slide freely with respect one another [116]. In the actin bundle the filaments are free to slide with respect to each other, however there is a frictional force between the filaments, which might modify the relationship between number of filaments and bending rigidity.

	parameters	Definition	Parameter relations	Values
Prescribed parameters	L $(\mu\mathrm{m})$	Bundle length	—	20
	λ $(\mu\mathrm{m})$	Mean actin filament length	—	8.9
	κ_0 $(\mathrm{pN}\,\mu\mathrm{m}^2)$	Actin filament bending rigidity	—	4×10^{-2}
	A_0 (zJ)	Motor cross-link torque magnitude	—	75
Estimated parameters	ξ_0 $(\mathrm{pN\,s})$	Shear-friction coefficient	$\xi_0 = \frac{\kappa_0}{k_\mathrm{d}}\mu^2$	5.35×10^{-2}
	ρ_0 $(\mu\mathrm{m}^{-1})$	Basal motor density	$\rho_0 = \frac{\bar{\rho}_0}{\mu}$	45
	v $(\mu\mathrm{m\,s}^{-1})$	Motor advection velocity	$v = \bar{v}\mu k_\mathrm{d}$	1.12
	$N_0 k_0$ $(\mathrm{s}^{-1}\,\mu\mathrm{m}^{-1})$	Constant motor binding rate	$N_0 k_0 = \frac{\bar{k}_0 k_\mathrm{d}}{\mu}$	0.03
	$N_0 k_1$ $(\mathrm{s}^{-1}\,\mu\mathrm{m}^{-1})$	Mechanosensitive motor binding rate	$N_0 k_1 = \frac{\bar{k}_1 k_\mathrm{d}}{\mu}$	605.5
	k_off (s^{-1})	Motor unbinding rate	$k_\mathrm{off} = \bar{k}_\mathrm{off} k_\mathrm{d}$	6.7×10^{-3}
	k_a (s^{-1})	Curvature-control rate of ρ_a	$k_\mathrm{a} = \frac{\kappa_0}{\mu}\frac{\bar{\Omega}}{A_0 k_\mathrm{a}}$	0.14
	k_d (s^{-1})	Relaxation rate of ρ_a	$k_\mathrm{d} = \frac{\bar{T}}{T}$	6.73×10^{-2}
	ϵ $(\mu\mathrm{m}^3\,\mathrm{s}^{-1})$	nonlinear unbinding of ρ_a	$\epsilon = \frac{\bar{\epsilon}(k_\mathrm{d}\mu)^3}{k_\mathrm{a}^2}$	4.46×10^{-2}
	C_0/N_0 $(\mu\mathrm{m}^{-1})$	Characteristic curvature	$\frac{C_0}{N_0} = \frac{\bar{C}_0}{\mu}$	0.24

Table 4.c: Definition and values of dimensional parameters for numerical solutions of Eqs. (4.12 – 4.14)

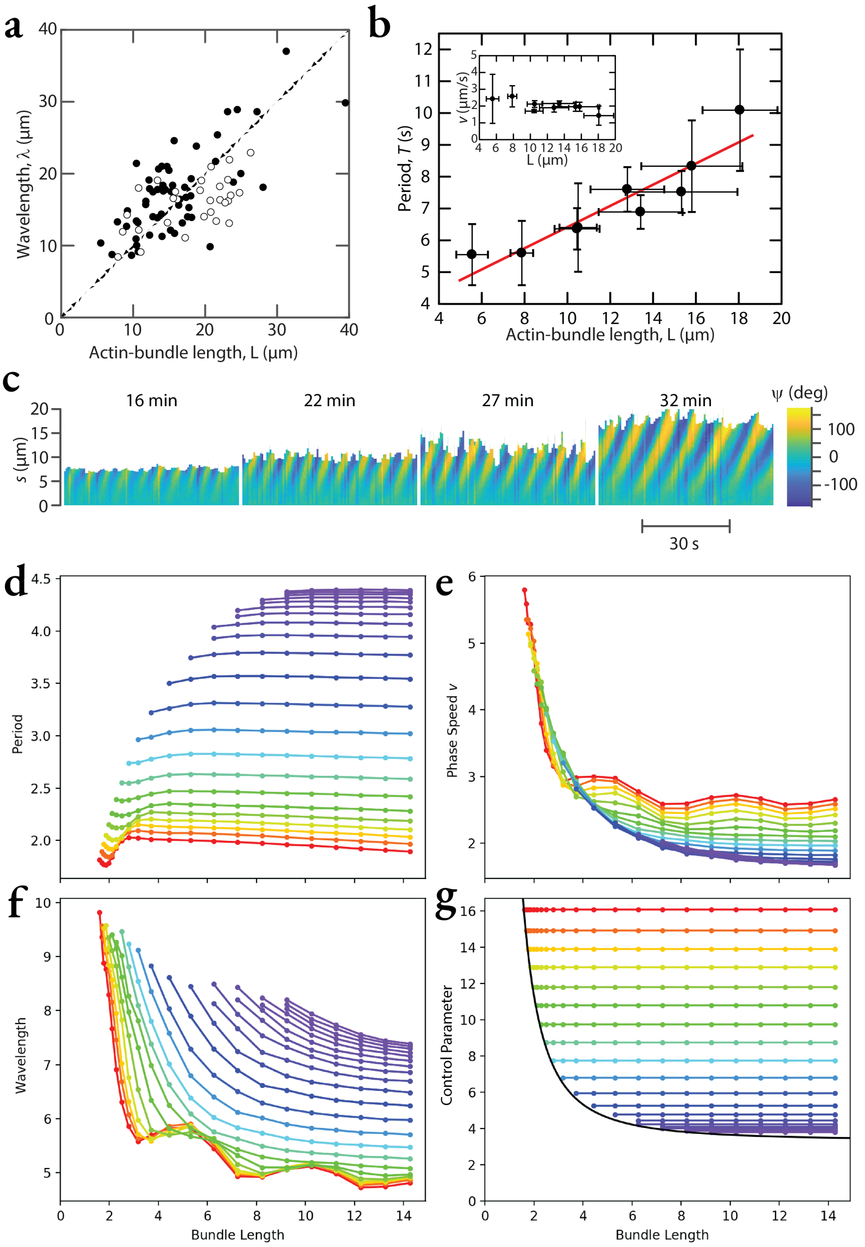

Figure 4.8: (**a**) Wavelengths λ of actin bundle's tangent angle's waves as a function of the bundle length L, driven by myosin-II (black dots) or myosin-V (white dots), (**b**) Period T with red linear fit of $0.33\,\mathrm{s}\,\mu\mathrm{m}^{-1}$ and phase velocity v of tangent angle waves, (**c**) Color plot of the tangent angle $\psi(s,t)$ for a single bundle driven by myosin-II at different times and bundle lengths. Numerical results as a function of the control parameter (color) and the length (abscissa) (**d**) dimensionless period, (**e**) dimensionless phase velocity, (**f**) dimensionless wavelength and (**g**) control parameter as a function of the dimensionless bundle length. The black line corresponds to the onset of the instability.

CHAPTER 5

Summary and Outlook

The aim of the dissertation, is to present a theoretical framework to study the dynamics of active filaments as found in biological systems, as well as synthetic active filaments. Cilia and flagella are very different from their synthetic counterparts [12, 16, 17, 37], yet they both exhibit qualitatively similar behaviours, indicating the existence of universal principles governing the dynamics of beating filaments. Starting from the hypothesis that the same physics underlies the spontaneous oscillations of cilia and bottom-up active bundles, we postulate that both these classes of systems are special cases of a more general object: an active filament.

An active filament is a slender structure, much longer than it is wide, driven locally by active moments alongg its length. If the dynamics of the active moments are regulated by the filament conformation, and if these active moments are balanced by the elastic and dissipative moments governing the shape of the filament, then spontaneous oscillations and travelling bending waves may occur. In this dissertation, we derive equations of motion for an active filament in a novel manner using linear irreversible thermodynamics and symmetry principles. These equations of motion, in their most general form, fully describe the dynamics of a heterogeneous active filament in two dimensions. In particular, the appearance of different friction terms in the equations of motion is derived systematically. These friction forces have different relative importances, depending on the structural properties of the filament, and have important effects on the subsequent dynamics. The active moments follow an explicit evolution equation. Therefore, the theoretical framework presented in this dissertation, describes the dynamics of a filament in the time domain.

After deriving general equations of motion, we studied particular limiting cases, where a single source of friction dominates the dynamics of a homogeneous filament. The limit of dominant external friction, leads to a fourth order nonlinear equation, which we linearised and studied numerically. The limit of dominant shear friction leads to a second order linear equation; for a specific choice of the boundary conditions, the equations of motion can be solved analytically. Analytical and numerical solutions were then compared. Finally, the limit of dominant curvature friction is described by a mixed-order partial differential equation, with dynamic boundary conditions. Estimating the relative values of the different friction coefficients, we discovered that the limit of dominant shear friction is particularly relevant when studying the dynamics of cilia, flagella, and active filament-bundles.

We then analysed the dynamics of bio-mimetic actin bundles. These active filament–bundles are characterised by bending waves travelling at constant speed, despite the heterogeneous structure of the bundle, a saturation of the tangent angle maxima, as well as the presence of myosin-density waves, travelling from the base to the tip at nearly twice the speed of the bending wave, and twice its frequency. An active filament in the limit of dominant shear friction, coupled to a phenomenological equation modelling the dynamics of myosin-density waves, could adequately describe the experimental observations. The equation governing the dynamics of the myosin-density waves predicts a mechanosensitive recruitment of myosin from the ambient solution: not only is a bent actin filament predicted to have an increased myosin binding rate, but the effect is drastically increased in the case of an actin-filament–myosin bundle.

The dissertation leaves many doors open, and many open questions. We list some of them below.

We have assumed throughout the dissertation that the filament obeys mirror symmetry. Such an assumption is difficult to justify: the constituent filaments of both biological cilia and flagella, as well as artificial microtubule and actin bundles, are helical, and therefore break mirror symmetry [12, 16, 17, 37]. Studying the dynamics of an active filament, without mirror symmetry, might unveil interesting and novel regimes.

In the dissertation, we considered an active moment which is conjugate to the shear. We assumed its evolution equation to be as simple as possible, yet complex enough to still enable spontaneous oscillations to occur. Different forms for the evolution equation are possible, for example taking into account normal forces, or going beyond a phenomenological description of active moments, modelling the molecular dynamics of the motors. Active moments conjugate to the curvature could also exist, and lead to different dynamical regimes.

In the limits of dominant external and shear friction, the stability analysis of a filament of finite length does not agree with the stability analysis of an infinitely long filament. The infinite length limit is not trivial, understanding it would provide key insights into the dynamics of longer filaments and the structure of the theory presented in this dissertation. Examples of longer active filaments are numerous, such as the flagella of *Ctenophora*, which can be up to $2\,\mathrm{mm}$ in length [11]. Are these flagella well described by an infinite filament? Because of the increased length, we expect the dynamics to be dominated by hydrodynamic effects, however, how important is internal friction to describe their dynamics?

Regimes in which there are severals sources of friction were not studied in detail. The boundary conditions derived by the theory are, in general, dynamic, depending on the time-derivatives of either the curvature, the shear, or both. Understanding these regimes is critical to fully account for the dynamics of eukaryotic flagella: in particular when considering the couplings between the flagellum and the cell body, when studying the propulsion of the cell, or when interactions between two or more filaments are important. In particular, basal or hydrodynamic couplings should lead to synchronisation and the emergence of metachronal waves.

While the behaviour of an active filament in two dimensions is rich, a generic theory of such systems must also describe their three dimensional dynamics. Developing such a theory, using an approach similar to the one employed in this dissertation, would be of great interest.

APPENDIX A

DEFINITION OF THE GEOMETRICAL SHEAR

In this appendix we derive the expression for the geometric shear presented in section 2.1. Let us consider the behaviour of two ideal curves, γ_1 and γ_2, parametrised by s_1 and s_2 respectively, lying on each side of the centreline γ, at a constant distance $a/2$ parallel from it. These two curves are not material curves, there might be nothing where they are placed, and might be outside of the filament itself. They will be used to define the geometric shear occurring when the centreline curves. Let $\mathrm{d}s_1$ and $\mathrm{d}s_2$ be arc-length elements on curves γ_1 and γ_2 respectively. The projections of $\mathrm{d}s_{1,2}$ onto the centreline curve are called $\mathrm{d}s'_{1,2}$, and are given by the following relations:

$$\mathrm{d}s'_1 = \frac{1}{1+\frac{a}{2}C(s,t)}\,\mathrm{d}s_1, \tag{A.1}$$

$$\mathrm{d}s'_2 = \frac{1}{1-\frac{a}{2}C(s,t)}\,\mathrm{d}s_2. \tag{A.2}$$

This can be seen by considering two disks of radii $R+a/2$ and R respectively, then the length of a circular arc given by the angle $\mathrm{d}\theta_1$ is $\mathrm{d}s_1 = (R+a/2)\,\mathrm{d}\theta_1$ and $\mathrm{d}s'_1 = R\,\mathrm{d}\theta_1$ respectively. We can then write the first arc length as $\mathrm{d}s_1 = (1+aC/2)\,\mathrm{d}s'_1$ where $C = 1/R$.

The arc-length elements $\mathrm{d}s_{1,2}$ are of arbitrary size, we therefore choose them to be equal to an arc-length element $\mathrm{d}s$ on the centreline curve. Doing this we may compare how the curvature of the filament dilates the projection of one of the elements, and contracts the projection of the other. The difference in size will be defined as the infinitesimal sliding:

$$\mathrm{d}s'_2|_{\mathrm{d}s_2=\mathrm{d}s} - \mathrm{d}s'_1|_{\mathrm{d}s_1=\mathrm{d}s} = \frac{aC}{1-\left(\frac{a}{2}C\right)^2}\,\mathrm{d}s = \mathrm{d}\Upsilon. \tag{A.3}$$

We can then integrate over the centreline arc-length to get the sliding:

$$\Upsilon(s,t) = \Upsilon_0(t) + \int_0^s \mathrm{d}s' \frac{aC(s',t)}{1-\left(\frac{a}{2}C(s',t)\right)^2}. \tag{A.4}$$

The sliding is therefore related to the curvature by the local expression:

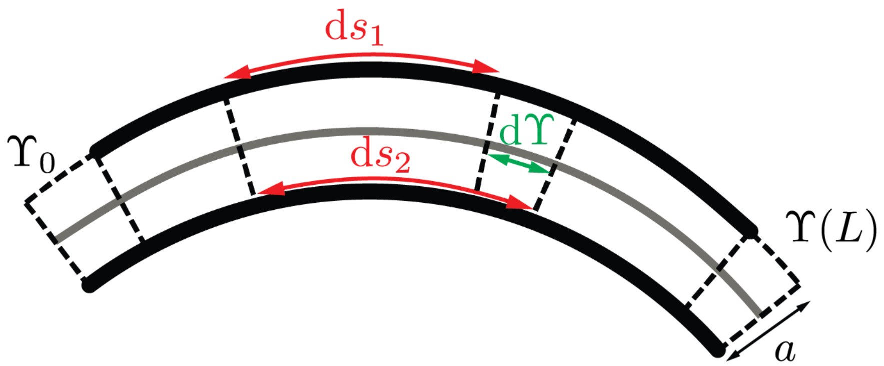

Figure A.1: Schematic showcasing the sliding element $\mathrm{d}\Upsilon$ in green, as the difference between the projections of the arc-length elements $\mathrm{d}s_1$ and $\mathrm{d}s_2$ in red, of two black curves distanced by the length $a/2$ from the centreline arc length in grey. The basal and distal sliding Υ_0 and $\Upsilon(L)$ are shown in black.

$$\partial_s \Upsilon = \frac{aC}{1-\left(\frac{a}{2}C\right)^2}. \tag{A.5}$$

The expression diverges when $aC = 2$, as there appears a kink in one of the curves $\gamma_{1,2}$. For $aC < 2$ the Taylor series expression of the infinitesimal sliding is the geometric series:

$$\mathrm{d}\Upsilon = 2\sum_{n=0}^{\infty}\left(\frac{a}{2}C\right)^{2n+1}\mathrm{d}s. \tag{A.6}$$

The sliding depends on the distance to the centreline, in order to have a geometric quantity independent from a we will define the *geometric* shear as the following limit:

$$\Delta = \lim_{a\to 0}\frac{1}{a}\Upsilon, \tag{A.7}$$

which then gives the following expression for the geometric shear:

$$\Delta(s,t) = \Delta_0 + \int_0^s \mathrm{d}s' C(s',t). \tag{A.8}$$

Because $C = \partial_s \psi$, we also have

$$\partial_s \Delta(s,t) = \partial_s \psi(s,t), \tag{A.9}$$

$$\Delta(s,t) - \Delta_0(t) = \psi(s,t) - \psi_0(t), \tag{A.10}$$

where Δ_0 and ψ_0 are the basal shear and the basal angle respectively. The shear Δ is a rotationally invariant transformation of the tangent angle ψ

APPENDIX B

TOY MODEL FOR THE ACTIVE STRESS

We present in this appendix a microscopic toy model, which recovers the form of the active moment dynamical equation (2.58) in general, and of the (linearised) equation for the asymmetric density (4.6) in particular. Let us consider a bundle of two filaments $i = 1, 2$, such as the one shown in figure A.1. On each filament there is a population of motors per unit length $\mathrm{d}n_i$, such that:

$$\mathrm{d}n_i = \rho_i \, \mathrm{d}s_i,$$

where ρ_i is the density of molecular motors per unit length, along the i^{th} filament. A motor can bind or unbind to the filament i with the binding rate per unit length k_{a} and the unbinding rate k_{d} respectively. We can therefore write the dynamical equation for the motor number per unit length per filament as:

$$\partial_t \, \mathrm{d}n_i = k_{\text{a}} \, \mathrm{d}s_i - k_{\text{d}} \, \mathrm{d}n_i.$$

In order to recover a dynamical equation for the whole bundle, we compute the projections of the above quantities into the centreline arc-length using equations (**??**, **??**). In particular the number of molecular motors per unit length and per filament becomes:

$$\mathrm{d}n_i = \rho_i \left(1 \pm \frac{aC(s)}{2}\right) \mathrm{d}s, \tag{B.1}$$

where C is the curvature of the bundle's centreline. We define the asymmetric density of molecular motors ρ_{a}, and the symmetric density of molecular motors ρ_{s} as:

$$\rho_{\text{a}} = \frac{\mathrm{d}n_1 - \mathrm{d}n_2}{\mathrm{d}s} = \rho_1 \left(1 + \frac{aC(s)}{2}\right) - \rho_2 \left(1 - \frac{aC(s)}{2}\right), \tag{B.2}$$

$$\rho_{\text{s}} = \frac{\mathrm{d}n_1 + \mathrm{d}n_2}{\mathrm{d}s} = \rho_1 \left(1 + \frac{aC(s)}{2}\right) + \rho_2 \left(1 - \frac{aC(s)}{2}\right). \tag{B.3}$$

The equations of motion are easily obtained by taking the time derivatives of equations (B.2, B.3), and inserting equation (B.1):

$$\begin{aligned}\partial_t \rho_{\mathrm{a}} &= a k_{\mathrm{a}} C - k_{\mathrm{d}} \rho_{\mathrm{a}},\\ \partial_t \rho_{\mathrm{s}} &= 2 k_{\mathrm{a}} - k_{\mathrm{d}} \rho_{\mathrm{s}}.\end{aligned}$$

APPENDIX C

NUMERICAL METHODS

Equations of motions described in chapters 3 and 4 were all solved numerically using a modified Crank-Nicolson [126] scheme with central finite differences. Because in this dissertation there are three different sets of equations of motion solved numerically, this appendix will be written quite generally, instead of going into the details of the implementation for each case.

Using dimensionless units, we define a state vector $\Sigma(\bar{s},\bar{t})$, which will be comprised of each of the independent variables of a particular case. For example, $\Sigma = (\psi, \bar{m}_\perp)^T$ for the case of dominant external friction, $\Sigma = (\Delta, \bar{m}_\Delta)^T$ for the case of dominant shear friction and $\Sigma = (\Delta, \bar{\rho}_\mathrm{a}, \bar{\rho})^T$ for the numerical solutions of the actin bundle system. We write the equations of motion in the general form:

$$\partial_{\bar{t}}\Sigma(\bar{s},\bar{t}) = \hat{\mathrm{M}}\Sigma(\bar{s},\bar{t}) + \hat{N}(\Sigma(\bar{s},\bar{t})), \tag{C.1}$$

where the $\hat{\mathrm{M}}$ and $\hat{N}$ are a linear and nonlinear operator respectively. For example, in the case of dominant shear friction, the operators are defined as:

$$\hat{\mathrm{M}} = \begin{pmatrix} -\bar{\kappa}_\Delta + \partial_{\bar{s}}^2 & -\bar{\Omega}_\Delta \\ \partial_{\bar{s}} & -1 \end{pmatrix},$$
$$\hat{N}(\Sigma) = \begin{pmatrix} 0 \\ -\epsilon\bar{m}_\Delta^3 \end{pmatrix}.$$

First, the time derivative is approximated by using a modified Crank-Nicolson scheme. We discretize in time using a tilmestep $\delta\bar{t}$, such that $\bar{t} = n\delta\bar{t}$ and $\Sigma(\bar{t},\bar{s}) \to \Sigma_n(\bar{s})$. Therefore, Equation (C.1) becomes

$$\frac{\Sigma_{n+1}(\bar{s}) - \Sigma_n(\bar{s})}{\delta\bar{t}} = \hat{\mathrm{M}}\frac{\Sigma_{n+1}(\bar{s}) + \Sigma_n(\bar{s})}{2} + \hat{N}(\Sigma_n(\bar{s})).$$

Rearranging the terms we get:

$$\left(\hat{\mathrm{I}} - \frac{\delta\bar{t}}{2}\hat{\mathrm{M}}\right)\Sigma_{n+1}(\bar{s}) = \left(\hat{\mathrm{I}} + \frac{\delta\bar{t}}{2}\hat{\mathrm{M}}\right)\Sigma_n(\bar{s}) + \delta\bar{t}\hat{N}(\Sigma_n(\bar{s})),$$

where $\hat{\mathrm{I}}$ is the identity operator. In order to compute each consecutive time-step as a function of the previous one, the left-hand side operator must be inverted. To do this we must now discretize in space, so that $\bar{s} = m\delta\bar{s}$, and $\Sigma_n(\bar{s}) \to \Sigma_{n,m}$. The linear operators $\hat{\mathrm{M}}$ and $\hat{\mathrm{I}}$ can now be written in matrix form. The spatial derivatives are approximated in the bulk by central finite differences so that, as an example:

$$\partial_s \Sigma_n(\bar{s}) = \frac{\Sigma_{n,m+1} - \Sigma_{n,m-1}}{\delta\bar{s}} + \mathscr{O}(\delta\bar{s}^2).$$

The boundary conditions are approximated by one sided finite differences. For example, in the case of dominant external friction, boundary condition (3.18) becomes:

$$\Delta_{n,0} = \frac{1}{1 + \delta\bar{s}\bar{k}_\Delta}\Delta_{n,1}.$$

Because the case of dominant external friction has up to fourth order derivatives, the formula $\Delta_{n,0}$ is used to replace the term wherever it appears in the matrix $\hat{\mathrm{M}}$. The same procedure is then done for all boundary conditions.

Every consecutive time-step can now be solved using:

$$\Sigma_{n+1,m} = \left(\hat{\mathrm{I}} - \frac{\delta\bar{t}}{2}\hat{\mathrm{M}}\right)^{-1}\left(\left(\hat{\mathrm{I}} + \frac{\delta\bar{t}}{2}\hat{\mathrm{M}}\right)\Sigma_{n,m} + \delta\bar{t}\hat{N}(\Sigma_{n,m})\right).$$

APPENDIX D

SHEAR CONTROL IN THE LIMIT OF DOMINANT SHEAR FRICTION

In this dissertation we have used an active moment controlled by curvature. Another possible choices to have an active moment controlled by shear. A shear controlled active moment obeys the following dynamical equation:

$$\partial_t m_\mathrm{a} = k_\mathrm{a}\Delta - k_\mathrm{d} m_\mathrm{a}.$$

The reason why such a choice of active moment has not been made, is that there exists cases in which no oscillatory instability exist. In this appendix we will show one such case. Let us write the following dimensionless equations of motion:

$$\begin{aligned}\partial_{\bar t}\Delta &= -\bar\kappa_\Delta\Delta + \partial_{\bar s}^2\Delta - \bar\Omega\bar m\\ \partial_{\bar t}\bar m &= \Delta - \bar m,\end{aligned}$$

where $\bar t = k_\mathrm{d} t$, $\bar s = s/\mu$, with $\mu = \sqrt{\kappa_C/(k_\mathrm{d}\xi_\Delta)}$, are the dimensionless units; $\bar\Omega = k_\mathrm{a}/(k_\mathrm{d}^2\xi_\Delta)$ is the control parameter, $\bar m = k_\mathrm{d} m_\mathrm{a}/k_\mathrm{a}$ is the dimensionless active moment, and where $\bar\kappa_\Delta = \kappa_\Delta/(k_\mathrm{d}\xi_\Delta)$ is the shear rigidity. For simplicity we choose to have no basal shear rigidity, therefore the boundary conditions are:

$$\begin{aligned}\partial_{\bar s}\Delta(0,\bar t) &= 0,\\ \partial_{\bar s}\Delta(\bar L,\bar t) &= 0.\end{aligned}$$

Using the Laplace ansatz $\Delta = \tilde\Delta\exp(-\bar q\bar s + \bar\omega\bar t)$, and $\bar m = \tilde m\exp(-\bar q\bar s + \bar\omega\bar t)$, we find the following dispersion relation:

$$\bar q^2 = \bar\omega + \frac{\bar\Omega}{1+\bar\omega} + \bar\kappa_\Delta.$$

The wave vectors are related to each other by a phase difference $\bar q_1 - \bar q_2 = 2\mathrm{i}\pi n/\bar L$, therefore the allowed angular frequencies must obey the following polynomials:

$$\left(\bar{\omega} + \bar{\kappa}_{\Delta} + \frac{4\pi^2 n^2}{\bar{L}^2}\right)(\bar{\omega} + 1) + \bar{\Omega} = 0. \tag{D.1}$$

An oscillatory instability occurs for purely imaginary values of the angular frequency $\bar{\omega} = \mathrm{i}\bar{\omega}_n$. Looking for such solutions in equation D.1 we find the two following polynomials:

$$\bar{\omega}_n^2 = \bar{\Omega} + \bar{\kappa}_{\Delta} + \frac{4\pi^2 n^2}{\bar{L}^2}, \tag{D.2}$$

$$0 = \bar{\omega}_n \left(1 + \bar{\kappa}_{\Delta} + \frac{4\pi^2 n^2}{\bar{L}^2}\right). \tag{D.3}$$

Equations (D.2,D.3) can only be true if $\bar{\omega}_n = 0$ or if the sum $\bar{\kappa}_{\Delta} + 4\pi^2 n^2/\bar{L}^2 = -1$. Because $\bar{\kappa}_{\Delta}$ and $4\pi^2 n^2/\bar{L}^2$ are positive, $\bar{\omega}_n$ must vanish. Therefore no oscillatory instability can exist.

LIST OF FIGURES

1.1 Examples of active filaments 4

2.1 Schematic of a planar filament 10

3.1 Stability of an infinite filament—limit of dominant external friction . . 31
3.2 Most unstable mode properties—limit of dominant external friction . . 32
3.3 Stability of a finite filament—limit of dominant external friction 33
3.4 Beating patterns of active filaments—limit of dominant external friction 34
3.5 Properties of tangent angle waves (1)—limit of dominant external friction 36
3.6 Properties of tangent angle waves (2)—limit of dominant external friction 37
3.7 Stability of an infinite filament—limit of dominant shear friction 39
3.8 Most unstable mode properties—limit of dominant shear friction . . . 40
3.9 Stability of a finite filament—limit of dominant shear friction 42
3.10 Slow mode—limit of dominant shear friction 44
3.11 Analytical waveforms at the instability (1)—limit of dominant shear friction 46
3.12 Analytical waveforms at the instability (2)—limit of dominant shear friction 47
3.13 Beating patterns (1)—limit of dominant shear friction 49
3.14 Properties of tangent angle waves (1)—limit of dominant shear friction . 50
3.15 Properties of tangent angle waves (2)—limit of dominant shear friction . 51
3.16 Beating patterns (2)—limit of dominant shear friction 52
3.17 properties of tangent angle waves (3)—limit of dominant shear friction . 53
3.18 properties of tangent angle waves (4)—limit of dominant shear friction . 54
3.19 Stability of an infinite filament—limit of dominant curvature friction . 57
3.20 Most unstable mode properties—limit of dominant curvature friction . 58
3.21 Angular frequency distribution in the complex plane—limit of dominant curvature friction 60

4.1 Actin micro-patterns and actomyosin bundles 65
4.2 Actin bundles driven by myosin-II 66
4.3 Actin bundles driven by myosin-V 67
4.4 Interplay between actin bundle and myosin-V density 68
4.5 Myosin-V density bundle distribution 69
4.6 Numerical solutions—actomyosin bundles 72
4.7 numerical solutions: position of the motor density peak on the bundle . 75

4.8 Length dependence of actomyosin bundles 79

A.1 Schematic of sliding between elements 86

List of Tables

2.a List of symmetries 11
2.b List oof physical quantities 14
2.c Thermodynamic fluxes and forces 16

3.a Dimensionless parameters—limit of dominant external friction 27
3.b Dimensionless parameters—limit of dominant shear friction 35
3.c Dimensionless parameters—limit of dominant curvature friction 56

4.a Parameters of the actomyosin bundle's beating 64
4.b Dimensionless parameters—actomyosin bundles 76
4.c Dimensional parameters corresponding to numerical solutions—actomyosin bundles 78

BIBLIOGRAPHY

[1] L. D. Landau, L. P. Pitaevskii, A. M. Kosevich, and E. M. Lifshitz. *Theory of Elasticity: Volume 7*. Elsevier, 1986.

[2] Basile Audoly and Yves Pomeau. *Elasticity and Geometry: From Hair Curls to the Non-linear Response of Shells*. Oxford University Press, June 2010.

[3] M. C. Marchetti, J. F. Joanny, S. Ramaswamy, T. B. Liverpool, J. Prost, Madan Rao, and R. Aditi Simha. Hydrodynamics of soft active matter. *Rev. Mod. Phys.*, 85(3), July 2013.

[4] J. Prost, F. Jülicher, and J.-F. Joanny. Active gel physics. *Nature Physics*, 11(2), February 2015.

[5] Christopher Battle, Chase P. Broedersz, Nikta Fakhri, Veikko F. Geyer, Jonathon Howard, Christoph F. Schmidt, and Fred C. MacKintosh. Broken detailed balance at mesoscopic scales in active biological systems. *Science*, 352(6285), April 2016.

[6] S. J. Kron and J. A. Spudich. Fluorescent actin filaments move on myosin fixed to a glass surface. *PNAS*, 83(17), September 1986.

[7] Yoshie Harada, Akira Noguchi, Akiyoshi Kishino, and Toshio Yanagida. Sliding movement of single actin filaments on one-headed myosin filaments. *Nature*, 326(6115), April 1987.

[8] Sara Moens and Jos Vanderleyden. Functions of Bacterial Flagella. *Critical Reviews in Microbiology*, 22(2), January 1996.

[9] Howard C. Berg. The Rotary Motor of Bacterial Flagella. *Annual Review of Biochemistry*, 72:19–54, 2003.

[10] Li Zhang, Jake J. Abbott, Lixin Dong, Bradley E. Kratochvil, Dominik Bell, and Bradley J. Nelson. Artificial bacterial flagella: Fabrication and magnetic control. *Appl. Phys. Lett.*, 94(6), February 2009.

[11] G. I. Matsumoto. Swimming movements of ctenophores, and the mechanics of propulsion by ctene rows. *Hydrobiologia*, 216(1):319–325, June 1991.

[12] William J. Snell, Junmin Pan, and Qian Wang. Cilia and Flagella Revealed: From Flagellar Assembly in Chlamydomonas to Human Obesity Disorders. *Cell*, 117(6), June 2004.

[13] David M. Woolley. Flagellar oscillation: a commentary on proposed mechanisms. *Biological Reviews*, 85(3), 2010.

[14] William Gilpin, Matthew Storm Bull, and Manu Prakash. The multiscale physics of cilia and flagella. *Nat Rev Phys*, 2(2), February 2020.

[15] Vivek N. Prakash, Matthew S. Bull, and Manu Prakash. Motility-induced fracture reveals a ductile-to-brittle crossover in a simple animal's epithelia. *Nat. Phys.*, 17(4), April 2021.

[16] Timothy Sanchez, David Welch, Daniela Nicastro, and Zvonimir Dogic. Cilia-Like Beating of Active Microtubule Bundles. *Science*, 333(6041), July 2011.

[17] Marie Pochitaloff, Martin Miranda, Mathieu Richard, Atitheb Chaiyasitdhi, Wenxiang Cao, Frank Jülicher, Laurent Blanchoin, and Pascal Martin. Flagella-like beating of actin bundles driven by self-organized myosin waves. 2022. to be published.

[18] Mark G. Nielsen and Elizabeth C. Raff. The best of all worlds or the best possible world? Developmental constraint in the evolution of beta-tubulin and the sperm tail axoneme. *Evol Dev*, 4(4):303–315, August 2002.

[19] Björn A. Afzelius. The fine structure of the cilia from ctenophore swimming-plates. *J Biophys Biochem Cytol*, 9(2):383–394, February 1961.

[20] W. L. Dentler. Microtubule-membrane interactions in ctenophore swimming plate cilia. *Tissue Cell*, 13(2):197–208, 1981.

[21] Nicholas Sperelakis. *Cell Physiology Source Book: Essentials of Membrane Biophysics*. Elsevier, December 2012.

[22] J Schrevel and C Besse. A functional flagella with a 6 + 0 pattern. *Journal of Cell Biology*, 66(3):492–507, September 1975.

[23] Kerstin Feistel and Martin Blum. Three types of cilia including a novel 9+4 axoneme on the notochordal plate of the rabbit embryo. *Dev Dyn*, 235(12):3348–3358, December 2006.

[24] D.M. Woolley. Studies on the eel sperm flagellum. I. The structure of the inner dynein arm complex. *Journal of Cell Science*, 110(1):85–94, January 1997.

[25] Gérard Prensier, Emile Vivier, Stuart Goldstein, and Joseph Schrével. Motile Flagellum with a "3 + 0" Ultrastructure. *Science*, 207(4438), March 1980.

[26] S. Marchese-Ragona and M. E. J. Holwill. Motile flagellar axonemes with a 9 + 1 microtubule configuration. *Nature*, 287(5785), October 1980.

[27] Romano Dallai, Björn A. Afzelius, and Wojciech Witalinski. The axoneme of the spider spermatozoon. *Bollettino di zoologia*, 62(4), January 1995.

[28] Gerard Prensier, Jean-Francois Dubremetz, and Joseph Schrevel. The unique adaptation of the life cycle of the coelomic gregarine Diplauxis hatti to its host Perinereis cultrifera (Annelida, Polychaeta): an experimental and ultrastructural study. *J Eukaryot Microbiol*, 55(6):541–553, December 2008.

[29] Z. V. Zizzari, P. Lupetti, C. Mencarelli, and R. Dallai. Sperm ultrastructure and spermiogenesis of Coniopterygidae (Neuroptera, Insecta). *Arthropod Structure & Development*, 37(5):410–417, September 2008.

[30] Gregory J. Pazour, Nathan Agrin, John Leszyk, and George B. Witman. Proteomic analysis of a eukaryotic cilium. *J Cell Biol*, 170(1):103–113, July 2005.

[31] Geraint G. Vernon and David M. Woolley. Basal Sliding and the Mechanics of Oscillation in a Mammalian Sperm Flagellum. *Biophysical Journal*, 87(6):3934–3944, December 2004.

[32] Sushil Khanal, Miguel Ricardo Leung, Abigail Royfman, Emily L. Fishman, Barbara Saltzman, Hermes Bloomfield-Gadêlha, Tzviya Zeev-Ben-Mordehai, and Tomer Avidor-Reiss. A dynamic basal complex modulates mammalian sperm movement. *Nat Commun*, 12(1), June 2021.

[33] V. Mukundan, P. Sartori, V. F. Geyer, F. Jülicher, and J. Howard. Motor Regulation Results in Distal Forces that Bend Partially Disintegrated Chlamydomonas Axonemes into Circular Arcs. *Biophysical Journal*, 106(11):2434–2442, June 2014.

[34] Veikko Geyer. *Characterization of the flagellar beat of the single cell green alga Chlamydomonas Reinhardtii*. PhD thesis, January 2014.

[35] D. M. Woolley and G. G. Vernon. A study of helical and planar waves on sea urchin sperm flagella, with a theory of how they are generated. *Journal of Experimental Biology*, 204(7), April 2001.

[36] D. D. Hackney. The kinetic cycles of myosin, kinesin, and dynein. *Annu Rev Physiol*, 58:731–750, 1996.

[37] Jonathon Howard. *Mechanics of Motor Proteins and the Cytoskeleton*. Sinauer Associates, Publishers, 2001.

[38] Gary J. Brouhard and Luke M. Rice. Microtubule dynamics: an interplay of biochemistry and mechanics. *Nat Rev Mol Cell Biol*, 19(7), July 2018.

[39] Katja M. Taute, Francesco Pampaloni, Erwin Frey, and Ernst-Ludwig Florin. Microtubule Dynamics Depart from the Wormlike Chain Model. *Phys. Rev. Lett.*, 100(2), January 2008.

[40] F Gittes, B Mickey, J Nettleton, and J Howard. Flexural rigidity of microtubules and actin filaments measured from thermal fluctuations in shape. *Journal of Cell Biology*, 120(4):923–934, February 1993.

[41] I. R. Gibbons and A. J. Rowe. Dynein: A Protein with Adenosine Triphosphatase Activity from Cilia. *Science*, 149(3682), July 1965.

[42] Stan A. Burgess, Matt L. Walker, Hitoshi Sakakibara, Peter J. Knight, and Kazuhiro Oiwa. Dynein structure and power stroke. *Nature*, 421(6924), February 2003.

[43] Samara L. Reck-Peterson, William B. Redwine, Ronald D. Vale, and Andrew P. Carter. The cytoplasmic dynein transport machinery and its many cargoes. *Nat Rev Mol Cell Biol*, 19(6), June 2018.

[44] Nobutaka Hirokawa, Yasuko Noda, Yosuke Tanaka, and Shinsuke Niwa. Kinesin superfamily motor proteins and intracellular transport. *Nat Rev Mol Cell Biol*, 10(10), October 2009.

[45] Kristen J. Verhey, Neha Kaul, and Virupakshi Soppina. Kinesin Assembly and Movement in Cells. *Annual Review of Biophysics*, 40:267–288, 2011.

[46] Enrique M. De La Cruz, Amber L. Wells, Steven S. Rosenfeld, E. Michael Ostap, and H. Lee Sweeney. The kinetic mechanism of myosin V. *Proc Natl Acad Sci U S A*, 96(24):13726–13731, November 1999.

[47] Amit D. Mehta, Ronald S. Rock, Matthias Rief, James A. Spudich, Mark S. Mooseker, and Richard E. Cheney. Myosin-V is a processive actin-based motor. *Nature*, 400(6744), August 1999.

[48] James R Sellers. Myosins: a diverse superfamily. *Biochimica et Biophysica Acta (BBA) - Molecular Cell Research*, 1496(1):3–22, March 2000.

[49] Lynne Coluccio. *Myosins: A Superfamily of Molecular Motors*, volume 7. January 2008.

[50] C. Dobell. *Antony van Leeuwenhoek and his "Little Animals."*. Harcourt, Brace and Co, New York, 1932.

[51] Phil Beales and Peter K. Jackson. Cilia - the prodigal organelle. *Cilia*, 1(1):1, April 2012.

[52] Robert Hooke. *Micrographia, or some physiological descriptions of minute bodies made by magnifying glasses, with observations and inquiries thereupon*. Jo. Martyn, and Ja. Allestry, printers to the Royal Society, London, 1665.

[53] J. GRAY. Studies in Animal Locomotion : I. The Movement of Fish with Special Reference to the Eel. *Journal of Experimental Biology*, 10(1):88–104, January 1933.

[54] J. GRAY. Studies in Animal Locomotion : VI. The Propulsive Powers of the Dolphin. *Journal of Experimental Biology*, 13(2):192–199, April 1936.

[55] J. GRAY. Studies in Animal Locomotion : VIII. The Kinetics of Locomotion of Nereis diversicolor. *Journal of Experimental Biology*, 16(1):9–17, January 1939.

[56] J. GRAY. The Mechanism of Locomotion in Snakes. *Journal of Experimental Biology*, 23(2):101–120, December 1946.

[57] J. GRAY. Undulatory Propulsion. *Journal of Cell Science*, s3-94(28):551–578, December 1953.

[58] Geoffrey Ingram Taylor. Analysis of the swimming of microscopic organisms. *Proceedings of the Royal Society of London. Series A. Mathematical and Physical Sciences*, 209(1099), November 1951.

[59] Geoffrey Ingram Taylor. The action of waving cylindrical tails in propelling microscopic organisms. *Proceedings of the Royal Society of London. Series A. Mathematical and Physical Sciences*, 211(1105), February 1952.

[60] G. J. Hancock and Maxwell Herman Alexander Newman. The self-propulsion of microscopic organisms through liquids. *Proceedings of the Royal Society of London. Series A. Mathematical and Physical Sciences*, 217(1128), March 1953.

[61] J. GRAY. The Movement of Sea-Urchin Spermatozoa. *Journal of Experimental Biology*, 32(4):775–801, December 1955.

[62] J. GRAY and G. J. HANCOCK. The Propulsion of Sea-Urchin Spermatozoa. *Journal of Experimental Biology*, 32(4):802–814, December 1955.

[63] K. E. Machin. Wave Propagation along Flagella. *Journal of Experimental Biology*, 35(4), December 1958.

[64] K. E. Machin and Miriam Louisa Rothschild. The control and synchronization of flagellar movement. *Proceedings of the Royal Society of London. Series B. Biological Sciences*, 158(970), July 1963.

[65] Robert Rikmenspoel. The Tail Movement of Bull Spermatozoa: Observations and Model Calculations. *Biophysical Journal*, 5(4), July 1965.

[66] Björn Afzelius. Electron Microscopy of the Sperm Tail Results Obtained with a New Fixative. *The Journal of Biophysical and Biochemical Cytology*, 5(2):269–278, March 1959.

[67] I. R. Gibbons. Structural Asymmetry in Cilia and Flagella. *Nature*, 190(4781), June 1961.

[68] I. R. Gibbons. THE RELATIONSHIP BETWEEN THE FINE STRUCTURE AND DIRECTION OF BEAT IN GILL CILIA OF A LAMELLIBRANCH MOLLUSC. *The Journal of Biophysical and Biochemical Cytology*, 11(1):179–205, October 1961.

[69] Peter Satir. STUDIES ON CILIA : The Fixation of the Metachronal Wave. *Journal of Cell Biology*, 18(2):345–365, August 1963.

[70] P. Satir. STUDIES ON CILIA : II. Examination of the Distal Region of the Ciliary Shaft and the Role of the Filaments in Motility. *J Cell Biol*, 26(3):805–834, September 1965.

[71] C. J. Brokaw. Bend Propagation along Flagella. *Nature*, 209(5019), January 1966.

[72] Peter Satir. Morphological Aspects of Ciliary Motility. *J Gen Physiol*, 50(6):241–258, July 1967.

[73] Peter Satir. STUDIES ON CILIA : III. Further Studies on the Cilium Tip and a "Sliding Filament" Model of Ciliary Motility. *Journal of Cell Biology*, 39(1):77–94, October 1968.

[74] Charles J. Brokaw. Bend Propagation by a Sliding Filament Model for Flagella. *Journal of Experimental Biology*, 55(2):289–304, October 1971.

[75] Charles J. Brokaw. Computer Simulation of Flagellar Movement: I. Demonstration of Stable Bend Propagation and Bend Initiation by the Sliding Filament Model. *Biophysical Journal*, 12(5):564–586, May 1972.

[76] Charles B. Lindemann and Kathleen A. Lesich. Flagellar and ciliary beating: the proven and the possible. *Journal of Cell Science*, 123(4):519–528, February 2010.

[77] Charles B. Lindemann and Kathleen A. Lesich. The many modes of flagellar and ciliary beating: Insights from a physical analysis. *Cytoskeleton*, 78(2), 2021.

[78] Sébastien Camalet, Frank Jülicher, and Jacques Prost. Self-Organized Beating and Swimming of Internally Driven Filaments. *Phys. Rev. Lett.*, 82(7):1590–1593, February 1999.

[79] Sébastien Camalet and Frank Jülicher. Generic aspects of axonemal beating. *New J. Phys.*, 2, October 2000.

[80] Ingmar H. Riedel-Kruse, Andreas Hilfinger, Jonathon Howard, and Frank Jülicher. How molecular motors shape the flagellar beat. *HFSP Journal*, 1(3), September 2007.

[81] Andreas Hilfinger, Amit K. Chattopadhyay, and Frank Jülicher. Nonlinear dynamics of cilia and flagella. *Phys. Rev. E*, 79(5), May 2009.

[82] Pablo Sartori, Veikko F Geyer, Andre Scholich, Frank Jülicher, and Jonathon Howard. Dynamic curvature regulation accounts for the symmetric and asymmetric beats of Chlamydomonas flagella. *eLife*, 5, May 2016.

[83] J. Lubliner and J. J. Blum. Model for bend propagation in flagella. *Journal of Theoretical Biology*, 31(1):1–24, April 1971.

[84] R. Rikmenspoel and W. G. Rudd. The contractile mechanism in cilia. *Biophys J*, 13(9):955–993, September 1973.

[85] J. Lubliner and J. J. Blum. Analysis of bend initiation in cilia according to a sliding filament model. *Journal of Theoretical Biology*, 69(1):87–99, November 1977.

[86] M Hines and J J Blum. Bend propagation in flagella. I. Derivation of equations of motion and their simulation. *Biophys J*, 23(1):41–57, July 1978.

[87] Jacob J. Blum and Michael Hines. Biophysics of flagellar motility. *Quarterly Reviews of Biophysics*, 12(2), May 1979.

[88] Charles B. Lindemann. A model of flagellar and ciliary functioning which uses the forces transverse to the axoneme as the regulator of dynein activation. *Cell Motility*, 29(2), 1994.

[89] Charles B. Lindemann. A ”Geometric Clutch” Hypothesis to Explain Oscillations of the Axoneme of Cilia and Flagella. *Journal of Theoretical Biology*, 168(2):175–189, May 1994.

[90] Charles J. Brokaw and D. R. Rintala. Computer simulation of flagellar movement. III. Models incorporating cross-bridge kinetics. *J Mechanochem Cell Motil*, 3(2):77–86, 1975.

[91] C J Brokaw. Computer simulation of flagellar movement. IV. Properties of an oscillatory two-state cross-bridge model. *Biophys J*, 16(9):1029–1041, September 1976.

[92] M. Murase and H. Shimizu. A model of flagellar movement based on cooperative dynamics of dynein-tubulin cross-bridges. *Journal of Theoretical Biology*, 119(4):409–433, April 1986.

[93] Masatoshi Murase. Excitable dynein model with multiple active sites for large-amplitude oscillations and bend propagation in flagella. *Journal of Theoretical Biology*, 149(2):181–202, March 1991.

[94] Lars Onsager. Reciprocal Relations in Irreversible Processes. I. *Phys. Rev.*, 37(4), February 1931.

[95] Lars Onsager. Reciprocal Relations in Irreversible Processes. II. *Phys. Rev.*, 38(12), December 1931.

[96] L. Onsager and S. Machlup. Fluctuations and Irreversible Processes. *Phys. Rev.*, 91(6), September 1953.

[97] S. Machlup and L. Onsager. Fluctuations and Irreversible Process. II. Systems with Kinetic Energy. *Phys. Rev.*, 91(6), September 1953.

[98] H. B. G. Casimir. On Onsager’s Principle of Microscopic Reversibility. *Rev. Mod. Phys.*, 17(2-3), April 1945.

[99] Sybren Ruurds de Groot and Peter Mazur. *Non-equilibrium Thermodynamics*. Courier Corporation, January 1984.

[100] Michael G. Poirier and John F. Marko. Effect of Internal Friction on Biofilament Dynamics. *Phys. Rev. Lett.*, 88(22), May 2002.

[101] Ronald D. Vale, David R. Soll, and I. R. Gibbons. One-dimensional diffusion of microtubules bound to flagellar dynein. *Cell*, 59(5):915–925, December 1989.

[102] K. Tawada and K. Sekimoto. A physical model of ATP-induced actin-myosin movement in vitro. *Biophysical Journal*, 59(2):343–356, February 1991.

[103] Katsuhisa Tawada and Ken Sekimoto. Protein friction exerted by motor enzymes through a weak-binding interaction. *Journal of Theoretical Biology*, 150(2):193–200, May 1991.

[104] Katsuhisa Tawada. Dynamical Role of "Protein Friction" In the Sliding Movement of Protein Motors In Vitro. In Haruo Sugi and Gerald H. Pollack, editors, *Mechanism of Myofilament Sliding in Muscle Contraction*, Advances in Experimental Medicine and Biology, pages 291–297. Springer US, Boston, MA, 1993.

[105] Ken Sekimoto and Katsuhisa Tawada. Extended Time Correlation of In Vitro Motility by Motor Protein. *Phys. Rev. Lett.*, 75(1), July 1995.

[106] Debasmita Mondal, Ronojoy Adhikari, and Prerna Sharma. Internal friction controls active ciliary oscillations near the instability threshold. *Science Advances*, 6(33), August 2020.

[107] Ashwin Nandagiri, Avinash Satish Gaikwad, David L Potter, Reza Nosrati, Julio Soria, Moira K O'Bryan, Sameer Jadhav, and Ranganathan Prabhakar. Flagellar energetics from high-resolution imaging of beating patterns in tethered mouse sperm. *eLife*, 10, April 2021.

[108] Veikko F. Geyer, Jonathon Howard, and Pablo Sartori. Ciliary beating patterns map onto a low-dimensional behavioural space. *Nat. Phys.*, January 2022.

[109] Charles J. Brokaw. Microtubule sliding in swimming sperm flagella: direct and indirect measurements on sea urchin and tunicate spermatozoa. *Journal of Cell Biology*, 114(6):1201–1215, September 1991.

[110] Sriram Ramaswamy. Active matter. *J. Stat. Mech.*, 2017(5), May 2017.

[111] J. M. R. Parrondo, C. Van den Broeck, and R. Kawai. Entropy production and the arrow of time. *New J. Phys.*, 11(7), July 2009.

[112] P. Curie. Sur la symétrie dans les phénomènes physiques, symétrie d'un champ électrique et d'un champ magnétique. *J. Phys. Theor. Appl.*, 3(1), 1894.

[113] Masao Doi. Onsager's variational principle in soft matter. *J. Phys.: Condens. Matter*, 23(28), June 2011.

[114] P. C. Hohenberg and B. I. Halperin. Theory of dynamic critical phenomena. *Rev. Mod. Phys.*, 49(3), July 1977.

[115] P.C. Hohenberg and A.P. Krekhov. An introduction to the Ginzburg–Landau theory of phase transitions and nonequilibrium patterns. *Physics Reports*, 572:1–42, April 2015.

[116] Claus Heussinger, Felix Schüller, and Erwin Frey. Statics and dynamics of the wormlike bundle model. *Phys. Rev. E*, 81(2), February 2010.

[117] Ludger Harnau and Peter Reineker. Equilibrium and dynamical properties of semiflexible chain molecules with confined transverse fluctuations. *Phys. Rev. E*, 60(4), October 1999.

[118] Chris H. Wiggins, D. Riveline, A. Ott, and Raymond E. Goldstein. Trapping and Wiggling: Elastohydrodynamics of Driven Microfilaments. *Biophysical Journal*, 74(2):1043–1060, February 1998.

[119] István Gyarmati. *Non-equilibrium Thermodynamics*. Ingenieurwissenschaftliche Bibliothek / Engineering Science Library. Springer Berlin Heidelberg, Berlin, Heidelberg, 1970.

[120] Roger A. Horn and Charles R. Johnson. *Matrix analysis*. Cambridge University Press, Cambridge ; New York, 2nd ed edition, 2012.

[121] Michel Fruchart, Ryo Hanai, Peter B. Littlewood, and Vincenzo Vitelli. Nonreciprocal phase transitions. *Nature*, 592(7854), April 2021.

[122] A. Oberbeck. Ueber stationäre Flüssigkeitsbewegungen mit Berücksichtigung der inneren Reibung. 1876(81), January 1876.

[123] J. M. Burgers. On the Motion of Small Particles of Elongated Form. Suspended in a Viscous Liquid. In F. T. M. Nieuwstadt and J. A. Steketee, editors, *Selected Papers of J. M. Burgers*, pages 209–280. Springer Netherlands, Dordrecht, 1995.

[124] R. G. Cox. The motion of long slender bodies in a viscous fluid Part 1. General theory. *Journal of Fluid Mechanics*, 44(4), December 1970.

[125] Joseph B. Keller and Sol I. Rubinow. Slender-body theory for slow viscous flow. *Journal of Fluid Mechanics*, 75(4), June 1976.

[126] J. Crank and P. Nicolson. A practical method for numerical evaluation of solutions of partial differential equations of the heat-conduction type. *Mathematical Proceedings of the Cambridge Philosophical Society*, 43(1), January 1947.

[127] Itsushi Minoura, Toshiki Yagi, and Ritsu Kamiya. Direct Measurement of Inter-doublet Elasticity in Flagellar Axonemes. *Cell Structure and Function*, 24(1):27–33, 1999.

[128] Dominic W. Pelle, Charles J. Brokaw, Kathleen A. Lesich, and Charles B. Lindemann. Mechanical properties of the passive sea urchin sperm flagellum. *Cell Motility*, 66(9), 2009.

[129] Jianfeng Lin, Thomas Heuser, Kangkang Song, Xiaofeng Fu, and Daniela Nicastro. One of the Nine Doublet Microtubules of Eukaryotic Flagella Exhibits Unique and Partially Conserved Structures. *PLoS One*, 7(10):e46494, October 2012.

[130] Philip V. Bayly and Kate S. Wilson. Equations of Interdoublet Separation during Flagella Motion Reveal Mechanisms of Wave Propagation and Instability. *Biophysical Journal*, 107(7):1756–1772, October 2014.

[131] Narutoshi Kamiya, Tadaaki Mashimo, Yu Takano, Takahide Kon, Genji Kurisu, and Haruki Nakamura. Elastic properties of dynein motor domain obtained from all-atom molecular dynamics simulations. *Protein Eng Des Sel*, 29(8):317–325, August 2016.

[132] Marcel E. Janson and Marileen Dogterom. A Bending Mode Analysis for Growing Microtubules: Evidence for a Velocity-Dependent Rigidity. *Biophys J*, 87(4):2723–2736, October 2004.

[133] Clifford P. Brangwynne, Gijsje H. Koenderink, Ed Barry, Zvonimir Dogic, Frederick C. MacKintosh, and David A. Weitz. Bending Dynamics of Fluctuating Biopolymers Probed by Automated High-Resolution Filament Tracking. *Biophys J*, 93(1):346–359, July 2007.

[134] Anne-Cécile Reymann, Jean-Louis Martiel, Théo Cambier, Laurent Blanchoin, Rajaa Boujemaa-Paterski, and Manuel Théry. Nucleation geometry governs ordered actin networks structures. *Nat Mater*, 9(10):827–832, October 2010.

[135] Mathieu Richard, Carles Blanch-Mercader, Hajer Ennomani, Wenxiang Cao, Enrique M. De La Cruz, Jean-François Joanny, Frank Jülicher, Laurent Blanchoin, and Pascal Martin. Active cargo positioning in antiparallel transport networks. *PNAS*, 116(30), July 2019.

[136] D. J. Smith, E. A. Gaffney, H. Gadêlha, N. Kapur, and J. C. Kirkman-Brown. Bend propagation in the flagella of migrating human sperm, and its modulation by viscosity. *Cell Motility*, 66(4), 2009.

[137] Matthias Rief, Ronald S. Rock, Amit D. Mehta, Mark S. Mooseker, Richard E. Cheney, and James A. Spudich. Myosin-V stepping kinetics: A molecular model for processivity. *PNAS*, 97(17), August 2000.

[138] Anabel E.-M. Clemen, Mojca Vilfan, Johann Jaud, Junshan Zhang, Michael Bärmann, and Matthias Rief. Force-Dependent Stepping Kinetics of Myosin-V. *Biophys J*, 88(6):4402–4410, June 2005.

[139] Takeshi Sakamoto, Fei Wang, Stephan Schmitz, Yuhui Xu, Qian Xu, Justin E. Molloy, Claudia Veigel, and James R. Sellers. Neck length and processivity of myosin V. *J Biol Chem*, 278(31):29201–29207, August 2003.

[140] Paolo Pierobon, Sarra Achouri, Sébastien Courty, Alexander R. Dunn, James A. Spudich, Maxime Dahan, and Giovanni Cappello. Velocity, Processivity, and Individual Steps of Single Myosin V Molecules in Live Cells. *Biophys J*, 96(10):4268–4275, May 2009.

[141] Claudia Veigel, Stephan Schmitz, Fei Wang, and James R. Sellers. Load-dependent kinetics of myosin-V can explain its high processivity. *Nature Cell Biology*, 7(9), September 2005.

[142] Claudia Veigel, Fei Wang, Marc L. Bartoo, James R. Sellers, and Justin E. Molloy. The gated gait of the processive molecular motor, myosin V. *Nature Cell Biology*, 4(1), January 2002.

[143] J. Christof M. Gebhardt, Anabel E.-M. Clemen, Johann Jaud, and Matthias Rief. Myosin-V is a mechanical ratchet. *PNAS*, 103(23), June 2006.

[144] James R. Sellers and Claudia Veigel. Direct observation of the myosin-Va power stroke and its reversal. *Nature Structural & Molecular Biology*, 17(5), May 2010.

[145] H. Isambert and A. C. Maggs. Bending of Actin Filaments. *EPL*, 31(5-6), August 1995.

[146] Sotaro Uemura, Hideo Higuchi, Adrian O. Olivares, Enrique M. De La Cruz, and Shin'ichi Ishiwata. Mechanochemical coupling of two substeps in a single myosin V motor. *Nature Structural & Molecular Biology*, 11(9), September 2004.

[147] Giovanni Cappello, Paolo Pierobon, Clémentine Symonds, Lorenzo Busoni, J. Christof, M. Gebhardt, Matthias Rief, and Jacques Prost. Myosin V stepping mechanism. *PNAS*, 104(39), September 2007.

[148] Pablo Sartori, Veikko F. Geyer, Jonathon Howard, and Frank Jülicher. Curvature regulation of the ciliary beat through axonemal twist. *Phys. Rev. E*, 94(4), October 2016.

VERSICHERUNG

Hiermit versichere ich, Martin Miranda, dass ich die vorliegende Arbeit ohne unzulässige Hilfe Dritter und ohne Benutzung anderer als der angegebenen Hilfsmittel angefertigt habe; die aus fremden Quellen direkt oder indirekt übernommenen Gedanken sind als solche kenntlich gemacht. Die Arbeit wurde bisher weder im Inland noch im Ausland in gleicher oder ähnlicher Form einer anderen Prüfungsbehörde vorgelegt. Die Dissertation wurde am Max-Planck Institut für Physik komplexer Systeme in Dresden unter der wissenschaftlichen Betreuung von Prof. Dr. Frank Jülicher und Prof. Dr. Jean-François Joanny angefertigt.

Martin Miranda,
Dresden, März 2022